

UC Merced

UC Merced Electronic Theses and Dissertations

Title

Understanding Surface and Bulk Properties of Lubricants

Permalink

<https://escholarship.org/uc/item/5kw1r1v4>

Author

Ramasamy, Uma Shantini

Publication Date

2017

Peer reviewed|Thesis/dissertation

UNIVERSITY OF CALIFORNIA, MERCED

**UNDERSTANDING SURFACE AND BULK
PROPERTIES OF LUBRICANTS**

by

Uma Shantini Ramasamy

A dissertation submitted in partial satisfaction of the
requirements for the degree of
Doctor of Philosophy

in

Biological Engineering and Small-Scale Technology

Committee in charge:
Professor Ashlie Martini, Advisor
Professor Christopher Viney, Chair
Professor Sachin Goyal
Professor Yanbao Ma

2017

© Uma Shantini Ramasamy, 2017
All rights reserved.

The dissertation of *Uma Shantini Ramasamy* is approved, and it is acceptable in quality and form for publication on microfilm and electronically:

Professor Ashlie Martini, Advisor

Date

Professor Christopher Viney, Chair

Date

Professor Sachin Goyal

Date

Professor Yanbao Ma

Date

University of California, Merced
2017

*To my family, friends, and mentors who supported me through this
journey.*

ACKNOWLEDGEMENTS

I acknowledge support from the US Department of Energys (DOE) Office of Vehicle Technology (under Contract No. 27029) of the Pacific Northwest National Laboratory (PNNL) AOP project. PNNL is a multiprogram national laboratory operated by Battelle for DOE under Contract DEAC05-76RL01830. Several computational aspects of this dissertation used the Extreme Science and Engineering Discovery Environment (XSEDE), which was supported by National Science Foundation Grant No. ACI-1053575. I also acknowledge partial support from the Center for Information Technology Research in the Interest of Society (CITRIS) at the University of California and the American Chemical Society Petroleum Research Fund (# 55026-ND6)

CURRICULUM VITAE

EDUCATION

- Ph.D. in Materials Engineering (within the Biological Engineering and Small-Scale Technology graduate group), University of California, Merced, CA, US (2017)
- B.S. in Chemical Engineering, Purdue University, West Lafayette, IN, US (2012)

PROFESSIONAL EXPERIENCES

- Graduate Student Researcher, University of California, Merced CA (January 2013 –May 2017)
- Intern, Lubricant Additives Department, King Industries, Norwalk CT (June 2016 –August 2016)
- Intern, Lubricant Additives Department, King Industries, Norwalk CT (June 2015 –August 2015)
- Graduate Teaching Assistant, University of California, Merced CA (August 2012 –December 2012)
- Undergraduate Grader, Purdue University, West Lafayette IN (August 2010 –December 2010)

HONORS AND AWARDS

- Finalist, BASF Science Competition (August 2016)
- Graduate Student Opportunity Program Fellowship (Fall 2015 –Summer 2016)
- 1st Place, Student Poster Competition, Society of Tribologists and Lubrication Engineers Annual Meeting and Exhibition (May 2014)

- UC Merced Bobcat Fellowship (Spring 2014)
- Northern California STLE Section Research Scholarship (Spring 2013)
- UC Merced School of Engineering Graduate Fellowship (Spring 2013, Summer 2013)
- UC Merced School of Engineering Travel Award (Summer 2013, 2014, 2015, 2016)
- Top Research Poster, Summer Undergraduate Research Fellowship Research Symposium (August 2011)
- Public Service Department Scholarship (2007 –2012)

PUBLICATIONS

Journals

1. Bhattacharya P., **Ramasamy US.**, Krueger S., Robinson JW., Tarasevich B.J., Martini A., Cosimbescu L., (2016) “Trends in Thermoresponsive Behavior of Lipophilic Polymers”, *Ind. Eng. Chem. Res.*, **55** (51), pp. 12983-12990
2. **Ramasamy US.**, Lichter S., Martini A. (2016) “Effect of Molecular-Scale Features on the Polymer Coil Size of Model Viscosity Index Improvers”, *Tribol. Lett.*, **62** (23), pp. 1-7
3. Adams H.L., Garvey M., **Ramasamy US.**, Ye Z., Martini A., Tysoe W.T. (2015) “Shear Induced Mechanochemistry: Pushing Molecules Around”, *J. Phys. Chem. C*, **119** (13), pp. 7115-7123
4. **Ramasamy US.**, Bair S., Martini A. (2015) “Predicting Pressure-Viscosity Behavior from Ambient Viscosity and Compressibility: Challenges and Opportunities”, *Tribol. Lett.*, **57** (11), pp. 1-7
5. Yi T., **Ramasamy US.**, Lichter S., Martini A. (2014) “Stability and Structure of Nanometer-thin Perfluoropolyether Films using Molecular Simulations”, *Tribol. Lett.*, **54** (2), pp. 119-127

Magazine Articles

1. **Ramasamy US.**, Cosimbescu L., Martini A. (2015) “Temperature-Dependent Conformations of Model Viscosity Index Improvers”, *Tribol. Lubr. Technol.*, **71** (5), pp. 30-31

ORAL PRESENTATIONS

- **Ramasamy US.**, Michael P., Simulation, Rheology, and Efficiency of Polymer Enhanced Solutions. Tribology Frontiers Conference, Chicago, IL. November 2016
- **Ramasamy US.**, Hu X., Novel Method Correlating Chemistry and Functionality. BASF Science Competition, Tarrytown, NY. August 2016
- **Ramasamy US.**, Cosimbescu L., Martini A., Viscosity and Structure of Model Viscosity Index Improvers. Tribology Frontiers Conference, Denver, CO. October 2015
- **Ramasamy US.**, Bair S., Martini A., Predicting Pressure-Viscosity Behavior from Ambient Viscosity and Compressibility: Challenges and Opportunities. Tribology Frontiers Conference, Chicago, IL. October 2014
- **Ramasamy US.**, Martini A., Predicting Pressure-Viscosity Coefficients using Molecular Dynamics Simulation. Society of Tribologists and Lubrication Engineers Northern California Section Meeting, Berkeley, CA. June 2014
- **Ramasamy US.**, Martini A., Predicting Pressure-Viscosity Coefficients using Molecular Dynamics Simulation. Society of Tribologists and Lubrication Engineers 69th Annual Meeting and Exhibition, Orlando, FL. May 2014

POSTER PRESENTATIONS

- **Ramasamy US.**, Lichter S., Martini A., Effect of Molecular-Scale Features on the Polymer Coil Size of Model Viscosity Index Improvers. Society of Tribologists and Lubrication Engineers 71st Annual Meeting and Exhibition, Las Vegas, NV. May 2016
- **Ramasamy US.**, Cosimbescu L., Martini A., Temperature-Dependent Conformations of Model Viscosity Index Improvers. Society of Tribologists and Lubrication Engineers 70th Annual Meeting and Exhibition, Dallas, TX. May 2015
- **Ramasamy US.**, Martini A., Estimating Pressure-Viscosity Coefficients using Molecular Dynamics. Society of Tribologists and Lubrication Engineers 69th Annual Meeting and Exhibition, Orlando, FL. May 2014

- **Ramasamy US.**, Yi T., Martini A., MD Simulation of the Structure and Stability of PFPE Lubricants. Society of Tribologists and Lubrication Engineers 68th Annual Meeting and Exhibition, Detroit, MI. May 2013
- **Ramasamy US.**, Vadakkepatt A., Martini A., Development of Realistic Lubricant Compressibility Model using Molecular Dynamic Simulations. SURF Research Symposium Poster Presentation, Purdue University, West Lafayette, IN. August 2011

PROFESSIONAL SOCIETY

- Member, Society of Tribologists and Lubrication Engineers (STLE), 2012–Present

PROFESSIONAL CONTRIBUTIONS

- Peer Reviewer of Submitted Manuscript, Scientific Reports
- Vice Chair, Nanotribology Session, Society of Tribologist and Lubrication Engineers 71st Annual Meeting and Exhibition, Las Vegas, NV. May 2016
- Poster Coordinator, Society of Tribologist and Lubrication Engineers 70th Annual Meeting and Exhibition, Dallas, TX. 2014-2015
- Poster Coordinator, Society of Tribologist and Lubrication Engineers 69th Annual Meeting and Exhibition, Orlando, FL. 2013-2014

TABLE OF CONTENTS

ACKNOWLEDGEMENTS	ii
CURRICULUM VITAE	iii
LIST OF FIGURES	xi
LIST OF TABLES	xvi
ABSTRACT	xviii

Chapter

1 INTRODUCTION	1
1.1 Lubrication	1
1.2 Lubrication Regimes	2
1.3 Properties of Lubricants	4
1.3.1 Bulk Properties	5
1.3.1.1 Viscosity	5
1.3.1.2 Density	5
1.3.1.3 Other Bulk Properties	6
1.3.2 Surface Properties	6
1.3.2.1 Chemical Reactions at the Lubricant-Surface Interface	6
1.3.2.2 Coverage and Stability	6
1.4 Lubricant Composition	7
1.4.1 Base Fluid	7
1.4.1.1 Mineral Oils	7

1.4.1.2	Synthetic Oils	8
1.4.2	Additives	9
1.4.2.1	Bulk Fluid Additives	9
1.4.2.2	Surface Additives	10
1.5	Objective and Motivation	11
1.6	Molecular Dynamics Simulation	11
1.7	Thesis Outline	12
I	Surface Properties of Lubricants	13
2	SURFACE COVERAGE AND STABILITY OF FUNCTIONALIZED POLYMERS	14
2.1	Introduction	14
2.2	Methods	16
2.3	Results	20
2.3.1	Film Characterization	20
2.3.1.1	Density	20
2.3.1.2	Film Conformation	20
2.3.1.3	Film Thickness	21
2.3.1.4	Roughness	22
2.3.2	Disjoining Pressure	23
2.4	Conclusions	28
3	SURFACE TRIBOCHEMISTRY	30
3.1	Introduction	30
3.2	Methods	31
3.3	Results	33
3.4	Discussion	36
3.5	Conclusion	37

II	Bulk Properties of Lubricants	40
4	PRESSURE-VISCOSITY BEHAVIOR OF LUBRICANTS	41
4.1	Introduction	41
4.2	Methods	43
4.2.1	Empirical Model	43
4.2.2	MD Simulation	44
4.3	Results	46
4.3.1	Accuracy of the General Correlation	46
4.3.2	Accuracy of the General Correlation with MD Data	47
4.4	Conclusions	50
4.5	Appendix	51
5	EFFECT OF MOLECULAR-SCALE FEATURES ON THE POLYMER COIL SIZE OF MODEL VISCOSITY INDEX IMPROVERS	53
5.1	Introduction	53
5.2	Methods	54
5.3	Results and Discussion	56
5.4	Conclusions	61
6	TRENDS IN THERMORESPONSIVE BEHAVIOR OF LIPOPHILIC POLYMERS	62
6.1	Introduction	62
6.2	Methods	63
6.3	Results	65
6.4	Discussion	72
6.5	Conclusion	74
7	SUMMARY AND FUTURE WORK	76
7.1	Summary	76

7.2	Future Work	77
7.2.1	Exploring Lubricant-Surface Interactions Under Shear	77
7.2.2	Exploring Mechanochemical Reactions Using Reactive Force Fields	77
7.2.3	Correlating Molecular Features to Coil Expansion and Viscosity	78
7.2.4	Exploring Alternative Mechanisms That Influence VII Functionality	79
7.2.5	Exploring Competition Between Boundary Lubricated Additives	79
7.3	Concluding Remarks	81
	BIBLIOGRAPHY	82

LIST OF FIGURES

1.1	The Stribeck curve, a plot that describes the relationship between friction and viscosity, load, and speed, shows the various lubrication regimes and their corresponding film thickness. Taken from reference [1].	3
1.2	Schematic illustrating the differences between boundary, mixed-film, and full-film lubrication regimes.	4
2.1	Left: Snapshot of a model lubricant film on a substrate. Right: Bead-spring structure of the lubricant models (with 10 beads or 20 beads) in which the coarse-grained beads are colored as shown. . .	17
2.2	Schematic diagram of the pair-wise interactions. V_{LJ} is the Lennard-Jones interaction and V_{func} is the functional group interaction. Superscripts (b , s , $func$) correspond to (lubricant, substrate, and functional group) bead types.	19
2.3	Density profiles for thick films using the 10-bead and 20-bead CG models, where $\epsilon^* = 1.0$ for the 10-bead model and $\epsilon^* = 1.0$ and 5.0 for the 20-bead model. The 20-bead model that is introduced here correctly predicts the bulk density. Inset: A close-up of the near-wall densities for the three cases. The peaks in density are spaced by σ_{10} or σ_{20} for the 10- and 20-bead models, respectively, indicating molecular layering [2].	21
2.4	Checking for complete substrate coverage. Variation of film conformations for different values of the (a) normalized LJ interaction strength between lubricant and substrate ϵ^* at constant $N = 325$, and (b) number of lubricant molecules, for the 20-bead CG model at constant $\epsilon^* = 0.25$. Subsequent simulations were restricted to conditions of complete coverage with $\epsilon^* \geq 1$ and $N > 605$	22

2.5	Roughness of the film surface as a function of film thickness (calculated using $\rho_{cut}=0.5$) for the 10-bead and 20-bead models; the dashed line is a theoretical prediction based on capillary wave theory.	24
2.6	Disjoining pressure calculated directly from the MD lubricant bead-substrate interaction energies. The dashed line is calculated assuming a $1/h^3$ dependence with a Hamaker constant of 1×10^{-19} J, an experimentally-reported value. Though the calculated values lie near the experimentally-reported values, their slopes do not well match the $1/h^3$ dependence, most noticeably for the case of $\epsilon^* = 5$.	25
2.7	Density profile for 20-bead cases with similar film thickness but generated using models with different interaction strengths. The density is in homogeneously distributed throughout the film thickness, with peaks in the density separated by the characteristic scale $\sigma_{20} = 0.43$ nm. Inset shows the Hamaker constant increasing with interaction strength; data from MD simulation and line represents a fit power law.	27
2.8	Disjoining pressure from the density measurements using Eq. 2.9. The black dashed line is the same as that in Figure 2.6 and the black dotted line is the estimate assuming a constant density of $1/\sigma^3$ across the entire film thickness and using $\epsilon^* = 1$.	28
3.1	(a) Fully atomic structure of methyl thiolate covered Cu(100) plates, where the inset shows a a close up of the adsorbed methyl thiolate species. (b) A top view snapshot of the adsorbed molecules. (c) A load of 0.45 GPa is imposed on the top plate and slid at a speed of 4 mm/s.	32

- 3.2 The 16 amu (methane) signal measured by sliding a tungsten carbide pin on a run-in (50 scans) clean copper foil as a function of the number of scans at a sliding speed of $1 * 10^{-3}$ m/s with a normal load of 0.44 N showing the decay in methane desorption yield as a function of the number of scans. Shown as an inset is the desorption yield measured from the area under each methane pulse as a function of the number of scans. After collecting data for the first DMDS dose, until no more methane was detected, the sample was re-saturated with DMDS and the 16 amu signal again monitored while sliding. This experiment was repeated for the third, fourth and fifth DMDS doses, where the evolution of methane yield as a function of the number of scans is identical. Experiments were performed by Dr. W.T. Tysoe's research group. 34
- 3.3 The calculated force distribution from MD simulations of methyl thiolate species on Cu(100) at a sliding speed of 4 mm/s with a contact pressure of 0.45 GPa; snapshots of the simulation are shown in the insets. The calculated average force F_0 is ~ 0.08 nN (dashed line in figure). However, the distribution of forces is Gaussian with a significant proportion of molecules experiencing much larger forces than the average value. The calculations show that $D = \sigma/F_0$, where σ is the standard deviation of the force distribution (dotted line in figure) is ~ 6.9 35
- 3.4 (a) A plot of the effective activation energy, $E_a(F)$, vs. D for an elastically deforming contact. Energy is estimated for a Gaussian force distribution with an average force of $F_0 \sim 0.018$ nN/molecule. The horizontal line shows the measured value of the shear-induced methyl thiolate decomposition activation energy for an elastically deforming contact. (b) A plot of the effective activation energy, $E_a(F)$, vs. D for a plastically deforming contact. Energy is estimated for a Gaussian force distribution with an average force of $F_0 \sim 0.07$ nN/molecule. The horizontal line shows the measured value of the shear-induced methyl thiolate decomposition activation energy, assuming plastic deformation at the contact. In both figures, the black squares represent energy distributions estimated using the Bell modal while the red circles represent energy distributions estimated using the Tomlinson/Prandtl model. Details on these calculations are available in reference [3]. This analysis was performed by Dr. W.T. Tysoe's research group. 38

4.1	(a) Fully atomistic structure of TOM and CPD (b) Cross sectional view of the initial configuration of the model where the black line indicates the periodic boundary. Colored spheres represent individual atoms: Orange-carbon and green-hydrogen	45
4.2	Normalized volume (normalized by ambient volume) versus pressure plots for TOM and CPD. Symbols represent MD data and the dashed lines represent the Tait equation fit to experimental data [4]	48
5.1	Atomic structures of the model (a) random ethylene-propylene copolymer, (b) polydodecylmethacrylate polymer, and (c) dodecane. (d) Initial configuration of the polydodecylmethacrylate molecule in dodecane solvent, where the dotted black lines indicate the periodic boundary. For all figures, colored spheres represent individual atoms: grey/black-carbon, white/pink-hydrogen, and red-oxygen . .	55
5.2	(a) Changes in R_g over time as the polymers moves and changes conformations (b) Frequency histogram plotted from raw R_g data. The dotted line represents a Gaussian fit to the histogram data. . .	57
5.3	Frequency histograms of (a) PMA and (b) OCP at 40°C and 100°C. Gaussian functions are fit to these histograms to obtain information on the mean and standard deviation of the distribution	58
5.4	Molecular structures of (a) polymethylmethacrylate (PMMA) and (b) a test polymer that is structurally similar to PMMA but without oxygen atoms (OFP). For all figures, colored spheres represent individual atoms: grey-carbon, red-oxygen, and white-hydrogen. The scale bar applies to all figures	60
6.1	Molecular structures of (a) PAMA, (b) OCP, (c) HBPE, and (d) Star. For all structures, colored spheres represent individual atom types: grey - carbon, white - hydrogen, red - oxygen.	64
6.2	(a) Initial configuration of HBPE in dodecane. The lines represent the periodic boundary. The carbon and hydrogen atoms in dodecane are represented by magenta and green spheres, respectively. The grey and white spheres represent the HBPE polymer. (b) Representative histogram of the radius of gyration of HBPE at the two temperatures, which were fit to Gaussian functions to obtain the mean of the distribution.	66

6.3	Schematic representation of the four polymers investigated, where the red line represents the polar backbone.	67
6.4	DLS plots as a function of temperature for (a) OCP, (b) PAMA, (c) HBPE, and (d) Star polymers. The scales of the y-axes have been adjusted to better visualize the changes in R_h . Error bars (standard error of the mean over 3 to 5 sample runs) are smaller than the data points and are not shown for clarity. DLS experiments and analysis were performed by P. Bhattacharya and B.J. Tarasevich from PNNL.	68
6.5	SANS profiles of (a) OCP, (b) PAMA, (c) HBPE, and (d) Star polymers in d-hexadecane. Solid red and blue lines show model fits to the SANS data. The data for OCP and PAMA polymers have been fitted to the polymer excluded volume model, whereas data for HBPE and Star polymers have been fitted to the correlation length model. The $I(Q)$ values at 100 °C data and their corresponding fits in each plot have been multiplied by 2 for clarity. Error bars (standard error of the mean for the number of detector pixels used in the data averaging) at low Q are smaller than the data points, and error bars at high Q are not shown for clarity. SANS experiments and analysis were performed by S. Krueger from NCNR.	70
6.6	Comparison between DLS, SANS, and MD simulations results of polymers, along with the VI values. Here R represents R_h values from DLS, R_g values from MD simulations, R_g values for OCP and PAMA, and L_c values for HBPE and Star polymers from SANS measurements. DLS experiments and analysis were performed by P. Bhattacharya and B.J. Tarasevich (PNNL) while SANS experiments were performed by S. Krueger (NCNR).	73
7.1	Schematic representation of potential copolymer configurations. The green and grey triangles represent different monomer species.	78
7.2	Schematic representation of a mixture of friction modifiers and antiwear additives at two different concentrations. The red spheres represent friction modifiers and the blue spheres represent antiwear additives.	80

LIST OF TABLES

1.1	API categorization of Group I-III base oils. Taken from Table 1.5 of reference [5].	8
2.1	Hamaker constants fit to simulation data using three different methods. The values under Energy are based on calculating the total interaction energy between the film and substrate. The Average Density values arise from evaluating Eq. (2.9) with $\rho_b = \bar{\rho}_b$. The Inhomogeneous Density values are from the numerical integration of Eq. (2.9), making use of the calculated values of the film density ρ_b as a function of height, as shown, for example, in Figure 2.7. (There were too few numerical points to evaluate the value for the 20-bead model at $\epsilon^* = 0.5$, shown above as N/A.)	26
3.1	Values of D obtained from MD at different normal pressures at a sliding speed of 40 m/s.	36
4.1	V_{molec} , A , and γ values required to predict PVR for DOS, CHH, TOM, CPD, and 80W-90	46
4.2	Predicted α^* for DOS, CHH, TOM, CPD, and 80W-90 are compared to reported literature values [4,6] (literature values in brackets)	47
4.3	V_{molec} , A , γ , and α^* values predicted by MD for TOM and CPD. α^* predictions are compared to reported literature values [4]	49
4.4	Predicted α^* and the resulting error in those predictions for TOM and CPD using $P - V$ and V_{molec} from either experiment or MD simulation	49
4.5	Viscosity for 80W-90 [6]	51
4.6	Calculated relative volume for 80W-90 [7]	52

5.1	Outline of the various stages of the simulations	56
5.2	Mean and standard deviation of the R_g distribution for PMA and OCP at 40°C and 100°C as well as the percent change in polymer coil size with increased temperature	59
5.3	Mean and standard deviation of PMMA and OFP at 40°C and 100°C, along with percent change with temperature	60
6.1	Summary of DLS measurements for all polymers at 45 and 95 °C. Errors (standard error of the mean over 3 - 5 sample runs) in R_h are within ± 0.04 nm.	69
6.2	Summary of SANS results for all polymers at 40 and 100 °C. Errors in R_g , L_c , and the Porod exponent are the statistical errors determined from the fits to the data.	72
6.3	Mean values of the R_g distribution for all polymers at 40 and 100°C along with the percent change in coil size with temperature ^a	73

ABSTRACT

Tribology is the study of friction, wear, and lubrication of surfaces in relative motion. In mechanical components, friction and wear lead to loss of energy efficiency. Lubricants control friction and wear by creating a film that separates contacting surfaces, which consequently reduces energy consumption and prolongs machine life. The effectiveness of a lubricating film is highly dependent on the physical and chemical properties as well as the composition of the lubricant used. Minor changes in chemical properties or composition can significantly influence the functionality of the lubricating film. Therefore it is necessary to understand the factors and mechanisms that influence the performance of lubricants at the molecular level.

The aim of this thesis is to investigate the surface and bulk properties of liquid lubricants using molecular dynamics (MD) simulation. This thesis is divided into two parts, where Part I focuses on understanding the properties of lubricated surfaces, and Part II explores the properties of bulk lubricants, specifically the pressure-viscosity and temperature-viscosity response of lubricating fluids. We explored the surface coverage and stability of thin functionalized polymer films using coarse-grain models, where we quantified the change in disjoining pressure with film thickness. We also studied the mechanochemical process occurring at boundary lubricated sliding interfaces and demonstrated that a distribution of forces are present at the sliding interface. Only a small percentage of the molecules at the sliding interface experienced forces large enough to initiate mechanochemical reactions. Next, we developed a novel method for predicting the pressure-viscosity response of fluids using an empirical equation and MD-predicted material properties. Using this method, the pressure-viscosity response of fluids was predicted from the variation of volume with pressure, which can be obtained relatively easily using atomic simulations. The temperature-viscosity response of liquid lubricants was also investigated to understand the mechanisms underlying the functionality of viscosity index improving (VII) polymers. Here, we studied the coil expansion mechanism of typical VII chemistries and found that the presence of specific molecular features influences the functionality of the polymer. In general, this work provides an in-depth analysis of several key properties that govern the functionality of surface and bulk lubricants. A clear understanding of functionality can lead to better lubricating capabilities through the design of novel application-specific lubricants, thus leading to an increase in energy efficiency and decrease in energy consumption.

Chapter 1

INTRODUCTION

Tribology is the study of friction, wear, and lubrication of interacting surfaces in relative motion [8]. Derived from the Greek word 'tribo', which means 'to rub' or 'to slide', tribology gained attention and popularity in 1966 after publication of the famous Jost Report. In his report, Peter Jost pointed out that the U.K. could potentially save approximately £515 million annually by the application of basic principles of tribology [9]. Since then, global energy consumption has reached new heights and is predicted to grow from 542 quads in 2012 to 770 quads in 2035 (1 quad $\approx 10^{18}$ J) [10]. Of the 95.1 quads consumed by the U.S. in 2011 [11], 61% was rejected (lost) energy. A significant portion of energy loss is attributed to friction, the force that resists the relative motion of two surfaces, where 7 quads of energy are wasted annually due to friction in passenger cars globally [12]. Additional waste is contributed by wear, the displacement of material from its original position, as the economic, environmental, and safety cost of wear-induced failures can be extensive [13]. Lubricants are typically used to lubricate surfaces and minimize metal-to-metal contact, therefore reducing friction and wear [1].

1.1 Lubrication

Lubricants are materials that reduce friction and wear by introducing a lubricating film between mechanical moving parts. Lubricants can be found in the form of solids, liquids, and gases, with liquids being the most common. Solid and gas lubricants are typically used in applications where liquid lubricants have limited functionality. For example, solid lubricants, such as graphite and molybdenum disulfide, are used in extreme environmental conditions, such as ambient temperatures above 500 °C or vacuum, where conventional liquid lubricants are less effective, i.e. have extremely low viscosities, decompose, or vaporize away from the surface [14].

Liquid lubricants typically come in the form of lubricating oils, which are a blend of base oil and additives [15]. The oil forms a lubricating film that minimizes metal-on-metal contact and reduces the force necessary to move one surface against the other, thereby reducing wear and saving energy [1, 5, 8, 16]. A lubricant also performs many diverse functions that ultimately help protect and prolong the life of equipment. Some of these functions include cooling, cleaning, protecting, and transferring power [1, 5, 8].

Cooling

In a mechanical component, heat is generated through friction, such as in gears, where metal surfaces rub against one another, or through conducted and radiated heat, such as combustion engines where parts are in close proximity to a heat source. In these situations, a lubricant can act as a heat sink that dissipates heat away from critical moving parts, which in return decreases the possibility of component deformation and wear [17].

Cleaning

For high temperature applications, lubricants can be oxidized to form carbon, sludge, and varnish [18]. These harmful products can form deposit precursors. Lubricants help suspend and remove carbon, sludge, varnish, dirt, and wear debris to facilitate smooth operation of the equipment [1, 17].

Protection

Lubricants prevent damage caused by oxidation, corrosion and wear. By forming a physical film that coats the metal surface, the lubricant prevents the surface from being susceptible to oxygen, water, and acids [1, 8, 17]. Some lubricants have additives such as rust and corrosion inhibitors, extreme-pressure (EP) additives, and anti-wear agents that form physical or chemical protective coatings on the metal surfaces.

Power Transfer

In hydraulic systems, a lubricant can be used as a medium to transfer power [1, 19]. The lubricant performs this function in addition to its normal function of lubrication. Transmissions, lifts, dump trucks, and fork lifts are some examples of equipment that use hydraulic technology.

1.2 Lubrication Regimes

The thickness of a lubricating film is used to characterize lubricated interfaces into different regimes, as illustrated by the Stribeck curve in Figure 1.1. The effectiveness of a lubricant in these regimes is affected by changes in lubricant viscosity, speed, and load, and quantified by changes in the friction coefficient. At low speed, low viscosity, and high load, the lubricating film will be too thin, leading to high friction. On the other hand, at high speed, high viscosity, and low load, the formation of a thicker film will reduce friction caused by surface-surface contact. An increase in the coefficient of friction is observed as the film continues to get thicker due to viscous drag as the viscosity of the lubricant increases. Based on the thickness of the lubricating film as well as the mechanism of film formation [16], the lubrication regimes are divided into boundary lubrication, mixed-film lubrication, and full-film lubrication. Figure

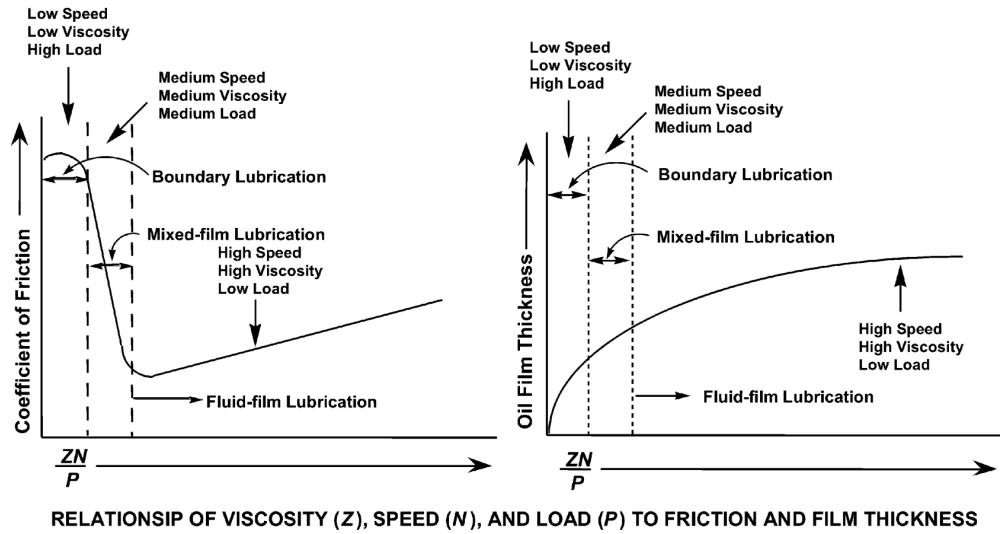


Figure 1.1: The Stribeck curve, a plot that describes the relationship between friction and viscosity, load, and speed, shows the various lubrication regimes and their corresponding film thickness. Taken from reference [1].

1.2 is a schematic illustrating the different conditions for boundary, mixed-film, and full-film lubrication regimes.

Boundary Lubrication

Boundary lubrication occurs at low speed, low viscosity, or high load, where a fluid film of sufficient thickness is unable to form. In the boundary lubrication regime, film thicknesses are in the order of $0.0\text{-}2.0\ \mu\text{m}$ [1] and surface-on-surface contact occurs. Lubrication in the boundary regime is aided by additives that physically or chemically attach onto the contacting surfaces to form a protective layer [20]. Some of these additives include, anti-wear, friction modifiers, and extreme pressure additives.

Mixed-Film Lubrication

When the contact between two rough surfaces is partially reduced, a mixed lubrication film is considered to exist [8]. Systems that fall in this regime have interfaces that experience both boundary and full-film lubrication. The load carrying capacity is divided between contacting surfaces and a lubricating film.

Full-Film Lubrication

At high speed, high viscosity, or low load, the fluid forms a layer that completely

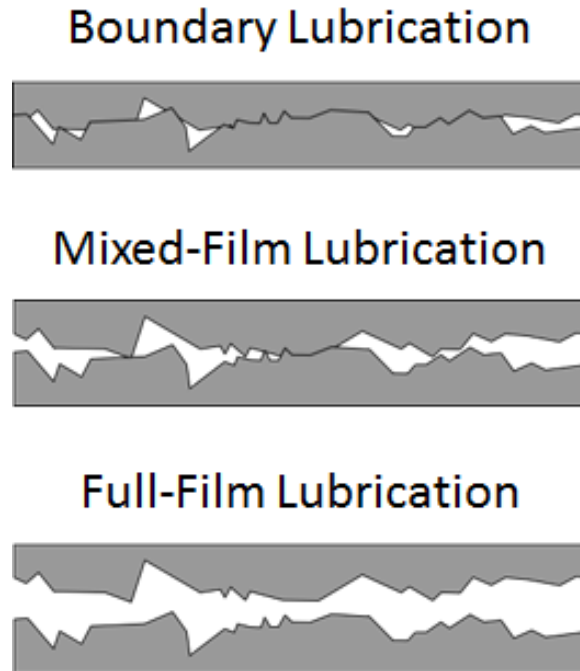


Figure 1.2: Schematic illustrating the differences between boundary, mixed-film, and full-film lubrication regimes.

separates the contacting surfaces. Within the full film regime, the contact between highly loaded counter-formal surfaces is classified as the elastohydrodynamic regime [21, 22], and contact between conformal surfaces is termed hydrodynamic lubrication [16]. Counter-formal surfaces, such as gears, have geometries that do not fit perfectly together. When a load is applied, parts of the system with relatively small contact areas experience pressures that are significantly higher than the rest of the surface. At these high pressures, the contact areas elastically deform and fluid viscosity is high enough to form a load bearing lubricating film [23]. Conformal surfaces, such as journal-sleeve bearings and hydrodynamic thrust bearings, have surfaces that geometrically fit well together. In these systems, the load is distributed evenly along the surface and no surface-surface contact or elastic deformation is observed [23].

1.3 Properties of Lubricants

The effectiveness of lubricating films is highly dependent on the physical and chemical properties as well as the composition of the lubricant used [15]. In the full film lubrication regime, lubricant viscosity and density play critical roles in application functionality. Similarly, the chemical properties of a lubricant are

important in boundary lubrication applications, where chemical interactions between lubricant and surface enable the formation of a lubricating film. Therefore, minimization of friction in the previously-mentioned regimes is achieved by improving the properties of the lubricating fluids. In this thesis, we will focus primarily on surface and bulk properties of lubricants.

1.3.1 Bulk Properties

1.3.1.1 Viscosity

Viscosity, a fluid property that resists flow, is the most important property of a lubricating oil. This feature drives the formation of a lubricating film (higher viscosities lead to thicker films) and ultimately determines the success or failure of a lubricated component [8]. Lubricant viscosity is sensitive to temperature, pressure, and shear rate changes [24–26]. Viscosity increases exponentially with increasing pressures, and decreases with increasing temperatures. Increasing shear rates can either increase (dilatant fluid) or decrease (pseudoplastic fluid) the viscosity of non-Newtonian fluids.

The temperature-viscosity relationship of a base fluid is captured by its viscosity index, a relative number that captures the rate of change in viscosity with temperature [27]. Fluids with high viscosity index values, such as polyalphaolefins, show minimum changes in viscosity with temperature while fluids with low viscosity index values, such as mineral oils, show drastic changes in viscosity with temperature. The pressure-viscosity relationship of a lubricant can be characterized by several different pressure-viscosity coefficient, all of which quantify the rate at which a lubricant’s viscosity increases with pressure.

While it seems logical to use highly viscous fluids to lubricate contacts due to their ability to form thicker films which in return leads to larger contact separation, this approach can in fact be detrimental to the system. Viscous fluids require more energy to be sheared, increasing power loss and heat generation. Since changes in environmental conditions alter lubricant viscosity, this can, if unaccounted for, lead to catastrophic component failure. In practice, lubricating oils are carefully chosen to provide optimum performance over a specific range of operating conditions. Hence, it is important to understand the effect of temperature, pressure, and shear rate on lubricant viscosity to avoid system failure while minimizing friction.

1.3.1.2 Density

Density, a measure of mass per unit volume, is a physical property that plays an important role in lubricant function and machine design [8]. This characteristic is affected by changes in temperature, pressure, and oxidation, where density increases with pressure and oxidation, and decreases with temperature. As fluid density increases, contaminant suspension time also increases. Depending on the system used, an increase in suspension time can be fatal to the operating system. For

example, hydraulic systems are sensitive to contaminants, therefore an increase in contaminant suspension time may lead to corrosion or cavitation [28]. Fluids with high densities have large erosion potentials [8]. In high-velocity or turbulent systems, the flow of these fluids can lead to corrosion and wear of surfaces.

High density fluids are typically used in filtration systems to aid in the removal of contaminants [28]. Their ability to increase particle suspension time eases the filtration processes. In a lubricated system, it is important to maintain the density of the lubricating fluid. Most systems are designed for a fluid with specific density, hence changes in fluid density that are outside of the system design can reduce the efficiency and durability of the system.

1.3.1.3 Other Bulk Properties

Thermal properties, such as specific heat, thermal conductivity, thermal diffusivity, flash point, volatility, and oxidation stability, are also important in lubrication. Understanding the effects of these features is important to application-specific lubricant selection. If the temperature within the system is too high, the oil degrades, and if the temperature is too low, the oil solidifies or freezes. However, thermal properties of a lubricant will not be discussed in this thesis.

1.3.2 Surface Properties

1.3.2.1 Chemical Reactions at the Lubricant-Surface Interface

Lubricant chemistry is an important attribute of lubricating oils. In a contact, chemical reactions between lubricating film and solid surface can be induced chemically or mechanically [20]. Reactions such as oxidation, polymerization, degradation, adsorption, and corrosion are prevalent throughout the lubricating film. Most of these reactions, such as corrosion and degradation, are detrimental to the mechanical system, if not controlled. Reactions such as adsorption, on the other hand, can form a thin protective layer that is beneficial for many applications [20].

In boundary lubrication, the thickness of the lubricating film is smaller than the average surface roughness, thus increasing contact between two asperities [8,20]. Friction at asperity-asperity contact creates heat and wear that encourages chemical reactions between the lubricant and solid surface. This chemical reaction forms thin films that coat the surface of the solid and protect it from further reactions. Most of these chemical reactions are accelerated by thermal energy, but there are also reactions that are mechanically induced [20].

1.3.2.2 Coverage and Stability

In boundary lubricated devices, such as micro electro-mechanical systems (MEMS) and hard disk drives (HDD), lubricant molecules adsorb to the solid surface to

provide protection and improve the durability of the system [29, 30]. The adhesive strength between lubricant and substrate is enhanced by the presence of functional groups in the lubricant's chemical structure [31]. In these applications, maximum protection is achieved by the formation of a thin, well distributed, and stable lubricating film. Advancements in devices, such as HDD, call for smaller, thinner, and faster performing equipment. These advancements can be achieved by the formulation of thinner (monolayer) films with strong adhesion and self-healing capabilities [32, 33].

1.4 Lubricant Composition

Commercial lubricants are composed of base fluid ($\sim 80\%$) and performance packages ($\sim 20\%$ or more). The performance packages are comprised of various additives in varying concentrations, where the concentration of additives depends on the quality of the base fluid as well as the intended end use [15]. Additives improve the lubricating capacity of the base oil by either enhancing existing properties or adding new properties.

1.4.1 Base Fluid

The major component of a lubricant is base fluid, therefore its bulk properties have a significant impact on the lubricating capabilities of the oil. An effective base fluid has exceptional inherent solvency, thermal stability, hydrolytic stability, low pour point (temperature at which the oil becomes semi-solid and loses its flow characteristic), high viscosity index, and low volatility [1, 5, 8]. These properties are directly related to the source, structure, chemistry, and degree of refinement of the base oil [1, 5, 8]. Base fluids can be divided into mineral oils and synthetic oils.

1.4.1.1 Mineral Oils

Mineral oils are a product of refined crude oil and consist of a mixture of paraffinic, naphthenic, and aromatic hydrocarbons [34]. The presence of different concentrations of paraffinic, naphthenic, and aromatic chemistries will affect physical properties such as pour point, viscosity index, and pressure-viscosity characteristics of the oil [8]. Paraffinic oils are preferred as base stocks, but have poor low-temperature functionality due to wax formation. Naphthenic base oils, on the other hand, have good low-temperature properties and pressure-viscosity relationship, but have mediocre oxidative stability. Aromatic oils are the least preferred for formulation of lubricants due to poor oxidative stability, but they have good solubility, thermal stability, and pressure-viscosity properties. Mineral oils also contain impurities, such as waxes as well as sulphur and nitrogen containing compounds, that can hinder the lubrication properties of the oil [5, 8]. The composition and purity of mineral oils can be improved through various refining stages and technologies.

Commercial mineral oils differ in composition, sulphur content, and viscosity depending on the source of the crude oil as well as the refining process [34]. Base oils produced from mineral oils can be divided into several categories, Group I-III base stock, based on their chemical composition, sulphur content, and viscosity index. Table 1.1 summarizes the properties of Group I-III oils as defined by the American Petroleum Institute, (API). Group I base oils are solvent refined, while Group II and III oils are hydrotreated [34]. Since Group II and III oils have a higher percentage of saturated components, these oils have better antioxidant properties compared to Group I. Overall, base oils with lower sulphur content, higher saturation concentrations, and higher viscosity index formulate better lubricants.

Table 1.1: API categorization of Group I-III base oils. Taken from Table 1.5 of reference [5].

Base Oil Categories	Saturates (%)	Sulphur (%)	Viscosity Index
Group I	< 90	≥ 0.03	$\geq 80, < 120$
Group II	≥ 90	0.03	$\geq 80, < 120$
Group III	≥ 90	0.03	≥ 120

1.4.1.2 Synthetic Oils

Synthetic base oils are man-made products manufactured from petroleum-derived low-molecular weight raw materials thorough various chemical reactions [1]. These products have well defined structures and properties. Examples of synthetic base fluids include polyalphaolefins, polybutenes, alkylated aromatics, polyol esters, phosphate esters, polyalkylene glycols, etc. Each type of synthetic fluid has its own advantages and disadvantages, therefore some are suitable for specific applications over others.

The most commonly used synthetic base oils are polyalphaolefins (PAO) and esters. PAO and esters have good thermal stability, oxidative stability, hydrolytic stability, shear stability, and low toxicity [1, 5]. PAOs are hydrogenated oligomers of α -olefin that are produced through free-radical oligomerization [35], Ziegler-catalyzed oligomerization [36–38], and Friedel-Crafts-catalyzed oligomerization [39–41]. The oligomerization process also provides high-purity base oils with good thermal and oxidative stability, but poor solvency of polar compounds [42]. Esters are manufactured through the esterification process by thermally reacting an acid and an alcohol in the presence of a catalyst [43]. The viscosity, thermal stability, hydrolytic stability, solvency, lubricity, and biodegradability of ester base oils can be modulated by the type of raw material used [5, 44].

API has categorized synthetic base fluids into two categories, Group IV and Group V base oils. Group IV oils are PAOs and Group V oils are all other base fluids that do not fall into categories I-IV. These include silicone oils, phosphate esters, and biolubes.

1.4.2 Additives

Additives are chemicals added in small quantities to the base oil to enhance or introduce new properties to the base fluid. These chemicals can improve the friction and wear characteristics of the oil, provide oxidative resistance, control corrosion and contamination, reduce the pour point, inhibit the generation of foam, as well as reduce the decline of viscosity with temperature [8]. Commonly used additives are viscosity modifiers, pour point depressants, detergents, corrosion and rust inhibitors, antioxidants, friction modifiers, anti-wear additives, extreme pressure additives, dispersants, anti-foam agents, emulsifiers, and dispersants. Some of these additives improve bulk fluid properties while others improve surface properties.

1.4.2.1 Bulk Fluid Additives

Lubricant characteristics, such as viscosity, cleanliness of the oil, and degradation of the oil through oxidation, can be controlled by the addition of additives that specifically improve bulk fluid properties and extend the lifetime of the oil. Additives, such as viscosity modifiers, pour point depressants, detergents, antioxidants, anti-foam agents, emulsifiers, and dispersants, are used to improve viscosity, control chemical breakdown, and control contamination of a lubricating oil.

Viscosity index improvers and viscosity modifiers are additives that improve the temperature-viscosity relationship of an oil, where viscosity modifiers are thickeners that improve low and high temperature functionality of an oil, while viscosity index improvers maintain the low temperature viscosity but enhance the high temperature functionality of an oil. These additives are typically large molecular weight polymers, such as polyalkylmethacrylates, olefin copolymers, polyisobutylenes, and styrene-butadienes [45–47]. As temperature is increased, these additives are believed to expand and impede the flow of the base fluid, therefore reducing the decline of viscosity with temperature [48]. Viscosity index improvers are used in the formulation of multigrade engine oils, gear oils, transmission fluid, etc. Pour point depressants enable the lubricant to flow at low temperatures and have chemistries that are similar to viscosity index improvers [49].

Mineral oils are highly susceptible to oxidative degradation through free radical chain reactions. Oxidation increases the overall viscosity and acidity of the oil, which can have detrimental effects on the performance of the lubricant [18, 50].

An increase in viscosity leads to power loss due to increased viscous drag while elevated acidity will accelerate corrosion of mechanical components [8]. Anti-oxidants are sacrificial additives that suppress oxidation of the oil [51]. These additives can be classified as metal deactivators, radical inhibitors, and peroxide decomposers [51].

Engine oils are regularly exposed to contaminants such as soot, wear debris, water, corrosion products, and dust. Without proper control of these contaminants, the lubricating capacity and life cycle of the lubricating oil is significantly reduced. Additives such as dispersant, demulsifiers, and detergents, preserve the integrity of the lubricating oil as well as the metal surfaces. Dispersants function by keeping insoluble contaminants, such as soot, suspended and dispersed in the oil to prevent them from coagulating to form larger particles [52]. Detergents neutralize and suspend byproducts of combustion and oxidation, hence keeping metal surfaces clear of detrimental deposits [1]. Demulsifiers enhance the separation of water from oils contaminated by water [53].

1.4.2.2 Surface Additives

Film forming additives are additives that specifically improve lubricity and protect metal surfaces. These additives include antiwear additives, friction modifiers, extreme pressure additives, and corrosion inhibitors. Surface additives function by physically or chemically attaching themselves to surfaces to provide a protective or lubricating layer [5, 54, 55]. If a lubricant is formulated with multiple surface active additives, these additives will compete amongst one another for the contact surfaces [56]. For this reason, it is important for lubricants to be formulated with very specific concentrations of surface active additives to ensure optimum lubricant functionality. Too much of one could lead to a loss of other properties.

Friction modifiers reduce the coefficient of friction between moving parts which improves fuel economy [57]. These additives have polar head groups, which are attracted to metal surfaces, and non-polar tail groups that are typically long alkyl chains. The polar head group adsorbs to a metal surface and the non-polar tail forms a lubricating film which reduces friction [58].

In applications where metal-on-metal contact is prevalent, such as gears, the metal surface needs to be protected against wear and equipment seizure. Antiwear and extreme pressure additives are boundary lubrication additives that protect metal surfaces from wearing off [59]. These two additives are similar in structure to friction modifiers except their non-polar tails are significantly shorter. Their polar to non-polar ratio is high, making them more surface active and resistant to shear. Antiwear additives, such as zinc dialkyl dithiophosphate and zinc diaryl dithiophosphate, perform well under mild loading conditions while extreme pressure additives, such as alkyl disulfides and dithiocarbamates, perform better under high loading conditions [60–62].

Acids formed from oxidation can accelerate corrosion of ferrous and non-ferrous surfaces [63]. Corrosion inhibitors control corrosion of non-ferrous metals from reactive elements, such as sulphur, phosphorous, and oxidation products, while rust inhibitors control corrosion of ferrous metals. These additives form a film that physically protects the surfaces from coming in contact with corrosion inducing agents. Benzotriazole and zinc diethyldithiophosphate are examples of corrosion inhibitors while metal sulphonates are good rust inhibitors [63–65].

1.5 Objective and Motivation

In this thesis we seek to develop methods that enable characterization and understanding of lubricant properties using molecular simulation tools. Ultimately, the objective of this work is to understand the relationship between molecular structure and lubricant functionality in both bulk fluid and surface applications. A clear understanding of structure and functionality will enhance current lubricating capabilities, thus increasing energy efficiency and reducing energy consumption. Growth in this area will also enable fast paced advancements in the field of lubricant design, specifically in the development of novel energy-efficient, application-specific lubricants.

1.6 Molecular Dynamics Simulation

The primary tool used in this investigation is Molecular Dynamics (MD) simulation, a computer simulation that provides an explicit representation of molecular structure. This computational tool is widely used to study changes in atomic positions, velocity, and orientation over time. Built on the principle of understanding macroscopic behavior by studying microscopic interactions, this method numerically solves Newton’s equation of motion for information on atomic trajectories [66]. This information is then used to calculate various properties of a model material.

In MD simulations, the interactions between atoms in a system are described by force fields, a set of empirical equations. Force fields that specifically model fluids do so by capturing atomic interactions using accurate models of bond, angle, torsion, etc. information of fluid-based systems. These force fields have been developed to study specific types of systems or molecules. For example, the Polymer Consistent Force Field (PCFF) was developed to model organic polymers, metals, and zeolites [67], whereas the Optimized Potential for Liquids Simulations (OPLS) was optimized to fit experimental properties of liquids [68].

MD simulations have been extensively used to study tribological properties of liquids [66, 69, 70]. Primarily used to supplement experimental predictions, MD simulations can be used to explore and understand data in areas that are not easily accessible via experimental approaches [66]. In this thesis, a variety of force fields and simulation models are used to accurately study the bulk and surface properties

of base fluids and additives. Details of the MD simulation methods used for specific studies will be presented in detail in subsequent chapters.

1.7 Thesis Outline

In this thesis, we aim to study the properties of liquid lubricants using MD simulation. This research will focus on bulk lubricant properties and surface interactions of liquid lubricants. This thesis is divided into two parts, where Part I (Chapters 2 and 3) focuses on surface properties of additives, while Part II (Chapters 4, 5, and 6) focuses on bulk properties of base fluids and additives. In Chapter 2 we discuss the structure and stability of a thin layer of functionalized polymer film. Chapter 3 focuses on understanding shear-induced mechanochemical reactions of lubricant coated surfaces. Studies on bulk fluid properties begin with Chapter 4, where we explore novel methods of predicting the pressure-viscosity behavior of lubricants. In Chapter 5 we explore the temperature-induced expansion of two commonly used viscosity index improvers to understand the mechanism behind their functionality. The study on viscosity improvers is continued in Chapter 6 where we compare and contrast different experimental and analytical techniques used to measure coil size. Finally, Chapter 7 concludes this thesis with a summary of completed work and an outlook on future research.

Part I

Surface Properties of Lubricants

Chapter 2

SURFACE COVERAGE AND STABILITY OF FUNCTIONALIZED POLYMERS

2.1 Introduction

Lubricants reduce friction between moving parts and increase durability of devices. Silicon (Si) is a ubiquitous substrate for micro electro-mechanical systems (MEMS). Though chosen for its electrical properties, silicon does not have good tribological characteristics. In cases in which MEMS are subject to wear, it is thus often helpful to provide a lubricating layer over the substrate. Functionalized polymers, such as perfluoropolyether (PFPE), are used for lubrication due to their stability over a wide range of operating temperatures, high flexibility and durability, good resistance to friction and wear, low volatility and surface tension, and good lubricity [29,30,71–74]. For example, in hard disk drives (HDD), a very thin lubricant layer (≈ 1 nm) is deposited onto the surface of the disk to protect the magnetic strip from being damaged [29]. As the demand for higher data storage density has grown, efforts to reduce the lubricant film thickness even further as a means to raise areal density have increased. At small film thicknesses, accurate film characterization methods become both more important and challenging.

Atomic-scale simulations are powerful tools for exploring the properties of thin lubricating films because they explicitly describe the molecular structure of the fluids which, at the small scale of modern devices, may directly determine observed properties [75–77]. We are interested here in thin perfluoropolyether (PFPE) films, which are widely used as lubricants. Pioneering research on PFPE using ab initio simulation methods showed the important role of the strength of interactions between PFPE molecules and an adjacent solid surface [78]. In addition, there are many examples of empirical model-based molecular dynamics (MD) simulation of PFPE lubricants in bulk systems or confined flow (see for example [79–82]). However, only recently has MD been applied to explore thin layers of PFPE on a surface. In general, there are two approaches to modeling PFPE on a surface: fully atomistic models that include all atoms in the system [30, 83] and coarse-grained models where a simplified bead-spring model is used to represent groups of atoms and bonds [84–86]. The latter is favorable for modeling large systems because of its computational efficiency, and this is the

approach we will use in this work. Previous coarse-grained models have been used to study a variety of PFPE film properties including lubricant morphology, lubricant-surface adhesion and the effect of local heating on lubricant behavior [84–86].

Stability is particularly important for liquid lubricant films since an unstable film can lead to device failure. Stability is often characterized in terms of disjoining pressure, Π , where the derivative of this parameter with respect to film thickness, h , must be less than zero to maintain a stable film. Since Derjaguin introduced the concept of disjoining pressure in 1936, various approaches have been developed to understand and quantify this property both theoretically and experimentally, including: (a) calculating the difference between bulk film pressure and pressure on the film surface [87], (b) applying the concept of Laplace pressure [88–91], and (c) taking the derivative of excess free energy with respect to film thickness [2, 87]. The first method is challenging to use with MD simulation due to the difficulty in accurately defining the interface between lubricant film and vacuum. The second method, which calculates disjoining pressure by equilibrating surface tension and excess free energy contributions, was applied by Izumisawa and Jhon [89] using molecular simulations. However, this method requires two independent surface curvatures, which cannot be applied to flat film conformations, and thus precludes direct calculation of disjoining pressure for thin films. Mate [2] described a third approach, which is based on directly taking the derivative of free energy with respect to film thickness, h [92]. In this approach, originally formulated by Derjaguin [87], disjoining pressure is the negative derivative of the excess free energy per unit area, F , with respect to film thickness h ,

$$\Pi(h) = -\left.\frac{\partial F}{\partial h}\right|_{(S,V,T)} , \quad (2.1)$$

where S is the surface area of the interacting surfaces, V is volume and T is temperature [87, 93, 94]. It is difficult to accurately numerically calculate the free energy [95, 96]. Change in the Helmholtz free energy $\Delta F = \Delta U - T\Delta S$ has contributions from changes in the internal energy ΔU and entropy ΔS . To simplify the calculation, the entropic term is often neglected [2]. This omission cannot be justified a priori. For example, for a film that is strongly attracting to the substrate such that it forms atomically-spaced layers, the entropy may be expected to be reduced relative to the bulk entropy. We will be concerned in particular with the variation in disjoining pressure with film thickness. In this case, the changes in entropy may not be critical. For example, it can be expected that translational entropy is proportional to volume [97], and so its variation with film thickness is proportional to the substrate area, which is a constant in our simulations. The translational entropy term would then add a constant to the disjoining pressure, and so have no contribution to the rate of change of disjoining

pressure that is a criterion for film stability (as discussed below). Using the assumption that the only film thickness dependent contribution to the free energy is $E(h)$, the excess interaction energy between a lubricant film and substrate, [2, 92] Eq. 2.1 can be further reduced to

$$\Pi(h) = -\left.\frac{\partial E(h)}{\partial h}\right|_{(s,v,T)}. \quad (2.2)$$

If we further assume that $E(h)$ arises primarily from van der Waals interaction energies between lubricant and substrate [2], we obtain the simplest and most often used expression relating disjoining pressure to film thickness

$$\Pi_{vdw}(h) = \frac{A_H}{6\pi h^3}, \quad (2.3)$$

where A_H is the Hamaker constant, a material property that represents the strength of van der Waals interactions between two bodies. For PFPE, the Hamaker constant has been reported to be in the range of $0.2 - 1 \times 10^{-19}$ J [2, 90]. The Hamaker constant is a function of interaction strength and density. The latter suggests another means of calculating disjoining pressure from MD since the simulation provides detailed information about the local density of the fluid.

In this chapter we use MD to characterize the structure and stability of thin PFPE films. We develop model films using several coarse-grained models that differ in the strength of the interaction between PFPE and the substrate, and in having 10 or 20 beads as the coarse-grained approximation of a single PFPE chain. These models are first analyzed in terms of their density profiles, film thickness, and surface roughness. The results suggest that the 20-bead model more accurately matches measured properties of PFPE. We then predict disjoining pressure using several approaches based on either direct calculation of fluid-substrate interaction energy or local fluid density. The model predictions are evaluated in terms of the magnitude of disjoining pressure and its dependence on film thickness which are then compared to expectations based on experimentally fit values of the Hamaker constant and the $1/h^3$ dependence on film thickness. We show that rapid computational methods based on the density of the film, though they may yield a poor estimate of the absolute value of the disjoining pressure, yield correct predictions for their rate of change, and consequently for stability.

2.2 Methods

The model, illustrated in Figure 2.1, consists of lubricant molecules and a rigid substrate. A coarse-grained (CG) bead-spring model is used to represent the structure of the PFPE lubricant. The per-bead molecular weight (MW) is assigned by dividing the MW of the entire molecule by the number of beads present in the bead-spring model. In this work, we explore two different bead-spring

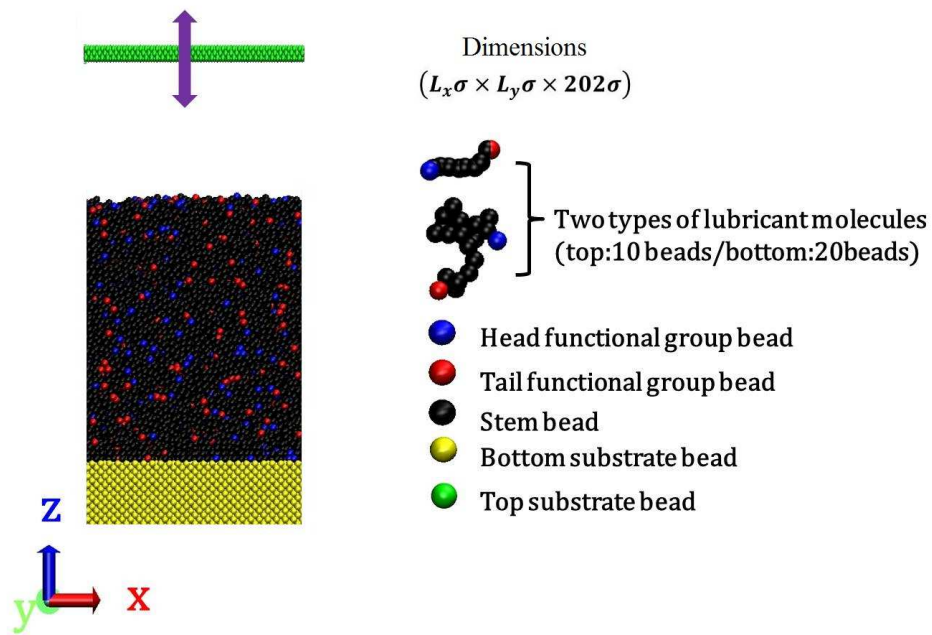


Figure 2.1: Left: Snapshot of a model lubricant film on a substrate. Right: Bead-spring structure of the lubricant models (with 10 beads or 20 beads) in which the coarse-grained beads are colored as shown.

configurations to represent a PFPE ZDOL 2000 molecule (MW 2000 g/mol): a 10-bead CG model and a 20-bead CG model; both are shown in Figure 2.1. The 10-bead structure, which consists of eight backbone beads and two end beads (functional groups), is similar to the model used by Ogata et al. [84] and Li et al. [85]. This structure has a length of 7 nm. The 20-bead model, on the other hand, has 18 backbone beads, 2 end beads, and a length of approximately 9 nm. This length is consistent with that of a fully atomistic PFPE ZDOL 2000 molecule predicted by Accelrys Materials Studio[®].

Three different bonded and non-bonded potential energy expressions are used to describe energetic interactions in both CG models. These potentials are the Finite Extensible Nonlinear Elastic (FENE) potential, the Lennard-Jones (LJ) potential, and the functional group interaction expression. The FENE potential, which describes intramolecular covalent bonds, is given by

$$V_{FENE} = -\frac{K_{FENE}R_{FENE}^2}{2} \ln \left[1 - \left(\frac{r}{R_{FENE}} \right)^2 \right], \quad (2.4)$$

where K_{FENE} is the stiffness of the bond, R_{FENE} is the maximum extent of the bond, and r is the distance between monomers. For this investigation, $K_{FENE} = 30$ and $R_{FENE} = 1.5$ [98].

The LJ potential defines interactions between any two beads within the simulation model,

$$V_{LJ} = 4\epsilon \left[\left(\frac{\sigma}{r} \right)^{12} - \left(\frac{\sigma}{r} \right)^6 \right], \quad (2.5)$$

where $\epsilon = 4 \times 10^{-21}$ J is the potential well depth, and σ is the separation at zero potential: $\sigma \equiv \sigma_{10} = 0.70$ nm for the 10-bead system, and $\sigma \equiv \sigma_{20} = 0.43$ nm for the 20-bead system. There are two types of lubricant interactions, lubricant-lubricant ($b-b$) and lubricant-substrate ($b-s$), that can be differentiated by their interaction strengths, ϵ_{b-b} and ϵ_{b-s} . The former is constant and will be referred to subsequently simply as ϵ . The latter is varied to explore the effect of lubricant-substrate interaction strength. The ratio of lubricant-substrate to lubricant-lubricant interactions strength is quantified by $\epsilon^* = \epsilon_{b-s}/\epsilon$. The value $\epsilon^* = 1$ is used for the 10-bead system, while $\epsilon^* = 0.25, 0.5, 1, 5$ is used for the 20-bead systems. The LJ potential is truncated at $r_{cutoff}^{b-b} = 2.5 \sigma$ for interactions between lubricant beads and $r_{cutoff}^{b-s} = 10 \sigma$ for interactions between beads in the film and substrate. Interactions between the functional groups at the ends of the lubricant chains and the substrate are expected to be stronger than those between the backbone and substrate. For stronger end group interactions, an additional energy term is assigned to end beads,

$$V_{func} = \alpha \exp \left(\frac{-r}{d} \right), \quad (2.6)$$

where $\alpha = -2 \epsilon$ is the attractive energy between two atoms and $d = 0.3 \sigma$ is the ionic-pair dependent length parameter [85,99]. Figure 2.2 provides a holistic picture of the various interactions.

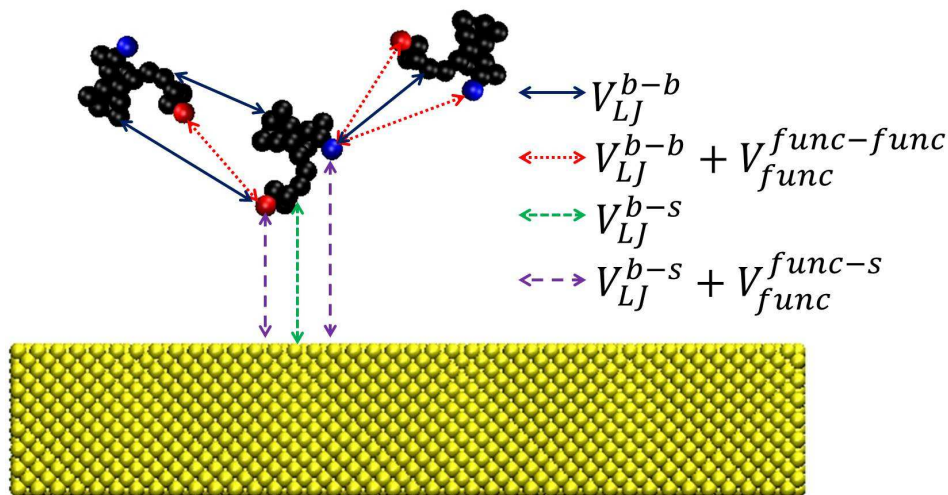


Figure 2.2: Schematic diagram of the pair-wise interactions. V_{LJ} is the Lennard-Jones interaction and V_{func} is the functional group interaction. Superscripts (b , s , $func$) correspond to (lubricant, substrate, and functional group) bead types.

Periodic boundary conditions are applied in the x - and y -directions (parallel to the surface), but not in the z -direction (film thickness). Two simulation box sizes are used: $(L_x, L_y, L_z) = (28.3 \sigma_{10}, 28.3 \sigma_{10}, 202.0 \sigma_{10})$ and $(L_x, L_y, L_z) = (56.6 \sigma_{20}, 56.6 \sigma_{20}, 202.0 \sigma_{20})$, for the 10-bead and 20-bead CG model, respectively. The rigid substrate consists of LJ spheres in a face-centered cubic (FCC) lattice. The number density of the substrate, expressed as number per σ^3 , is $\sqrt{2}$ where $\sigma = \sigma_{10}$ for the 10-bead model and $\sigma = \sigma_{20}$ for the 20-bead model. The x -direction is defined as [100]. The number of lubricant molecules present in a periodic unit cell is varied to study the changes in film thickness and lubricant coverage at equilibrium.

A Langevin thermostat is employed to keep the reduced temperature at $T^* = 1$, where $T^* = k_B/\epsilon$ with k_B the Boltzmann constant, and temperature is calculated using the equipartition theorem with the translational velocity of individual monomers. All simulation results are generated using the Large Atomic/Molecular Massively Parallel Simulator (LAMMPS) which employs the Verlet algorithm to solve the equations of motion of Newtonian mechanics [100]. Visual Molecular Dynamics (VMD) software is used to illustrate the molecular systems [101].

To create a thin lubricant film, some form of physical or chemical process has to be introduced to the equilibrated system. Previous work on this type of system employed either an additional external potential or modified lubricant interaction strengths to temporarily relocate molecules to the surface [84, 85]. In this work, we employ a simple heating, compression, and cooling process to methodically form a thin lubricant film. First, a top substrate is placed above the lubricant film to contain the lubricant molecules. The initial temperature of the system is set to a value 10 times higher than the target temperature for about 1500τ , where τ is the reduced time unit in a LJ system. Lubricant molecules are then compressed by moving the top substrate towards the bottom substrate at a velocity between $3 \sigma/\tau$ and $28 \sigma/\tau$, where the velocity is decreased as the system approaches its final film thickness. The final position of the top substrate varies for each system depending on the number of molecules contained by the simulation structure. Four intermediate relaxation times are allotted for each system during the compression process before the system reaches its target height. Finally the system is cooled to its target temperature at a rate of $(1/30)T^*/\tau$ before the top substrate is moved back to its original position. The system is then relaxed for more than 3000τ , where the exact relaxation time varies for each system depending on the number of lubricant molecules contained.

2.3 Results

2.3.1 Film Characterization

2.3.1.1 Density

Figure 2.3 presents density profiles for the 10-bead ($\epsilon^* = 1.0$) and 20-bead ($\epsilon^* = 1.0$ and $\epsilon^* = 5.0$) CG configurations, while the inset shows a close-up of the near-wall density of these films. All three films exhibit a plateau region which represents the bulk lubricant density. The plateau densities for each model can be compared to the reference bulk density of the material. It is evident that the commonly used 10-bead CG model, which has a density of 0.823 g/ml, does not accurately reproduce the density of PFPE ZDOL 2000 (1.81 g/ml). On the other hand, the 20-bead CG structure proposed, which has a density of 1.83 g/ml, predicts the expected bulk density that is accurate within 1%, for any ϵ^* .

2.3.1.2 Film Conformation

Although we use very thick films to evaluate the bulk fluid density, this research is focused on thinner films, i.e. those with thicknesses less than 10 nm, comparable to that expected in HDD or MEMS. For each combination of bead number and interaction strength, we attempted to model films with a range of thicknesses. However, as shown for a few representative cases in Figure 2.4, the ability to generate films with complete coverage on the surface depends on the number of

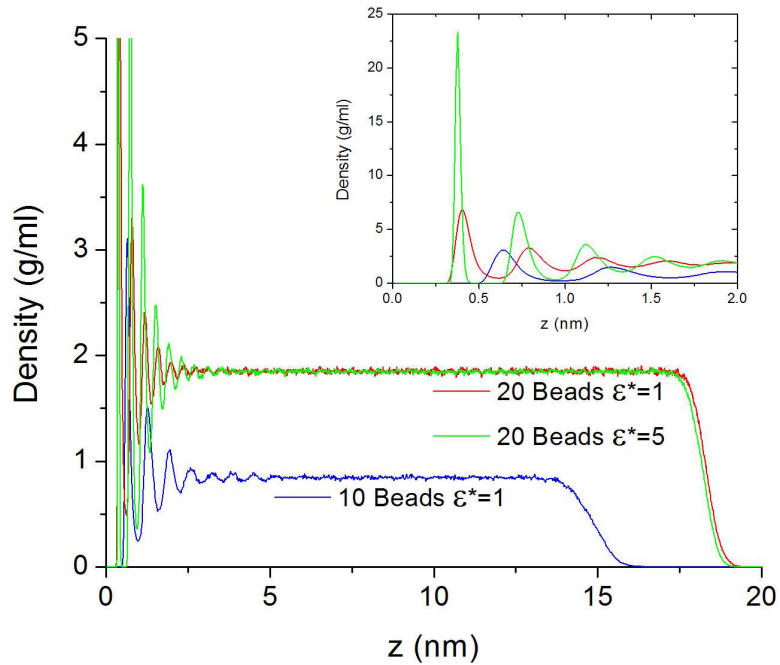


Figure 2.3: Density profiles for thick films using the 10-bead and 20-bead CG models, where $\epsilon^* = 1.0$ for the 10-bead model and $\epsilon^* = 1.0$ and 5.0 for the 20-bead model. The 20-bead model that is introduced here correctly predicts the bulk density. Inset: A close-up of the near-wall densities for the three cases. The peaks in density are spaced by σ_{10} or σ_{20} for the 10- and 20-bead models, respectively, indicating molecular layering [2].

lubricant molecules, N , and the lubricant-substrate interaction strength, ϵ^* . For small ϵ^* or N , lubricant molecules tend to aggregate to form a network of patches instead of distributing evenly over the substrate. In general, we found that ϵ^* must be greater than 1 for even distribution and the minimum N decreases with increasing ϵ^* . Given this constraint, we generated four films with complete surface coverage at different thicknesses for the 10-bead model with $\epsilon^*=1$ and for the 20-bead model with $\epsilon^*=1$ or 5 .

2.3.1.3 Film Thickness

Film thickness is calculated from density profiles such as those shown in Figure 2.3. Practically, a physical measurement of thickness would place the height somewhere within the interface over which the density decreases from a plateau to zero. To have

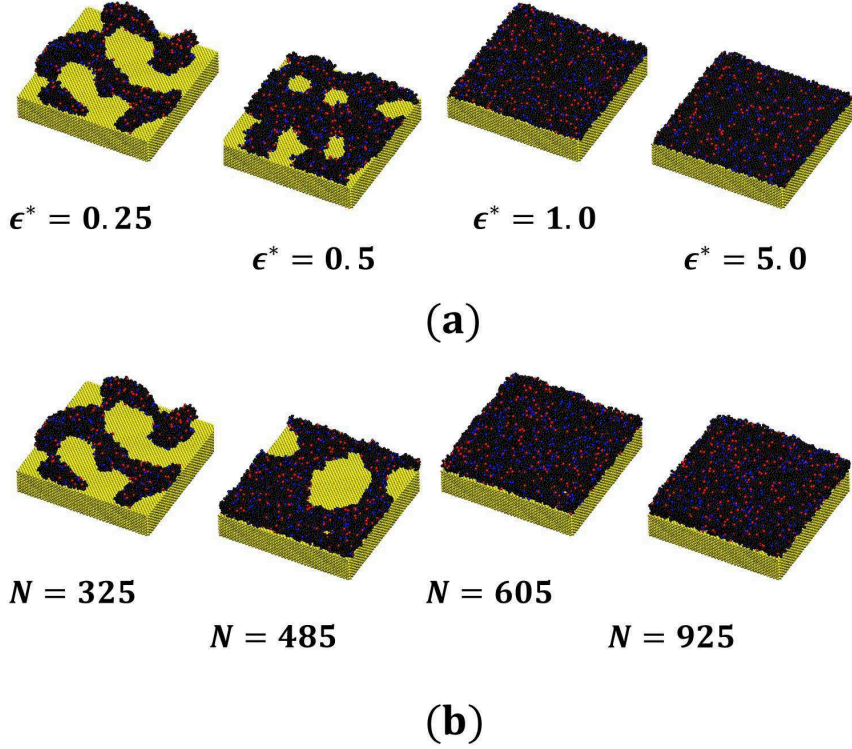


Figure 2.4: Checking for complete substrate coverage. Variation of film conformations for different values of the (a) normalized LJ interaction strength between lubricant and substrate ϵ^* at constant $N = 325$, and (b) number of lubricant molecules, for the 20-bead CG model at constant $\epsilon^* = 0.25$. Subsequent simulations were restricted to conditions of complete coverage with $\epsilon^* \geq 1$ and $N > 605$.

a definition of film height comparable to physical measurement, we define the top of the film to be the height at which the density decreases to some cut-off density ρ_{cut} .

2.3.1.4 Roughness

We also characterize the model films in terms of their surface roughness where roughness is quantified as the root-mean-square (RMS) height,

$$RMS = \left[\frac{1}{N_t} \sum_{k=1}^{N_t} (h_i - \bar{h})^2 \right]^{\frac{1}{2}}, \quad (2.7)$$

where h_i is the local height of the surface and \bar{h} is the average height of the surface taken at each snapshot for $N_t=400$ snapshots. Figure 2.5 shows how the surface

roughness varies with film thickness defined using $\rho_{cut}=0.5$. Roughness of the films increases with film thickness for all cases. Previous experimental measurements of PFPE film roughness [102] were fit to an equation based on capillary wave theory,

$$RMS = \sqrt{\sigma_0^2 + \frac{k_B T}{2\pi\gamma} \ln\left(\frac{\lambda_l}{\lambda_s}\right)}, \quad (2.8)$$

where $\sigma_0 = 0.1$ nm is the molecular roughness, k_B is the Boltzman constant, $T = 300$ K, $\gamma = 24$ mN/m is the surface tension, $\lambda_s = 1$ nm is the shortest wavelength of the capillary wave, and $\lambda_l = 2\pi h^2(2\pi\gamma/A_H)^{\frac{1}{2}}$ is the longest wavelength of the capillary wave at the liquid-vapor interface. In the wavelength expression, A_H is the Hamaker constant set to 10^{-19} J and h is film thickness. The prediction of this equation (which was consistent with some experimental data [102]) is shown in Figure 2.5. This comparison indicates that the surface roughness of the 20-bead model with $\epsilon^*=5$ is most consistent with predictions made by the capillary wave theory.

2.3.2 Disjoining Pressure

The most direct approach to predicting disjoining pressure from MD simulation is to use Eq. 2.2 with the assumption that the excess energy E is simply the sum of all lubricant bead-substrate interaction energies [93, 94]. We average these energies over time for each film thickness where film thickness is determined from the density profiles using $\rho_{cut}=0.5$. We then estimate the local derivative as the slope of a linear fit to two adjacent energy/film thickness data points. This calculation yields a single disjoining pressure which is associated with a film thickness that is the average of the two from which the slope was obtained. The results for each of the three models are shown in Figure 2.6. A comparison to the expected trend (Eq. 2.3 with a Hamaker constant of 1×10^{-19} J) reveals that these results do not capture the expected $1/h^3$ dependence well. This may be because small errors in the simulation-predicted energy are magnified by taking their derivative with respect to relatively small changes in film thickness. The magnitude of the disjoining pressure is described by the Hamaker constant which can be obtained for the simulation by fitting the data in Figure 2.6 to Eq. 2.3. The results are summarized in the second column of Table 2.1 headed “Energy” where we see that all three models predict Hamaker constants that are within the range of reported values ($0.2 - 1 \times 10^{-19}$ J). However, the inability of this approach to reproduce the expected $1/h^3$ dependence suggests an alternative method.

If we assume the $1/h^3$ dependence, we can use the simulation as a tool for determining the disjoining pressure directly as a function of interaction strength and density. The advantage of this approach is that densities are relatively quickly and easily generated from MD simulation whereas energies are obtained only from

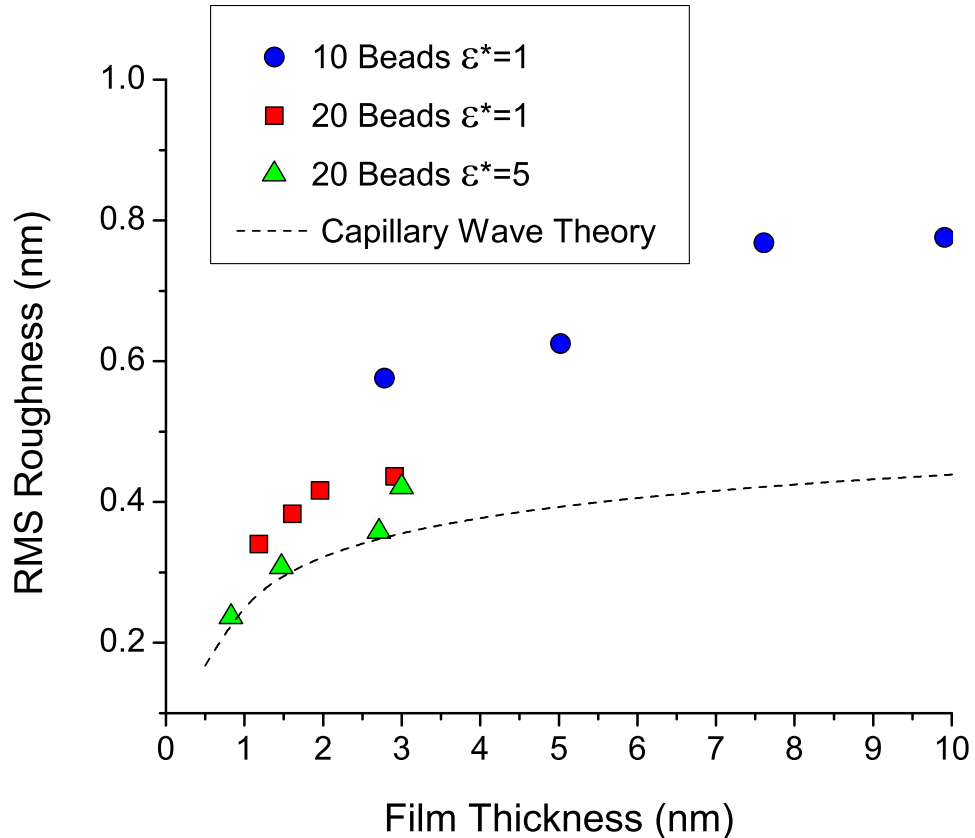


Figure 2.5: Roughness of the film surface as a function of film thickness (calculated using $\rho_{cut}=0.5$) for the 10-bead and 20-bead models; the dashed line is a theoretical prediction based on capillary wave theory.

long-time averages. First, we revisit the derivation of disjoining pressure. Following reference [93], the disjoining pressure per unit area of substrate between the film and the substrate is given by

$$\Pi = \frac{A_H}{6\pi\bar{\rho}_b} \frac{d}{dh} \int_0^h \frac{\rho_b dz}{z^3}, \quad (2.9)$$

in which $\bar{\rho}_b$ is the density averaged throughout the film of thickness h and z is the distance from the substrate. We investigated the effect of the film thickness cut-off heights in the range $0.1 \text{ beads}/\sigma^3 \leq \rho_{cut} \leq 0.7 \text{ beads}/\sigma^3$ on the values of the disjoining pressure to be presented below; the choice of cut-off had little effect on the numerical values. The PFPE molecule possesses two types of beads, those in the central portion of the molecule, interacting with the substrate with characteristic

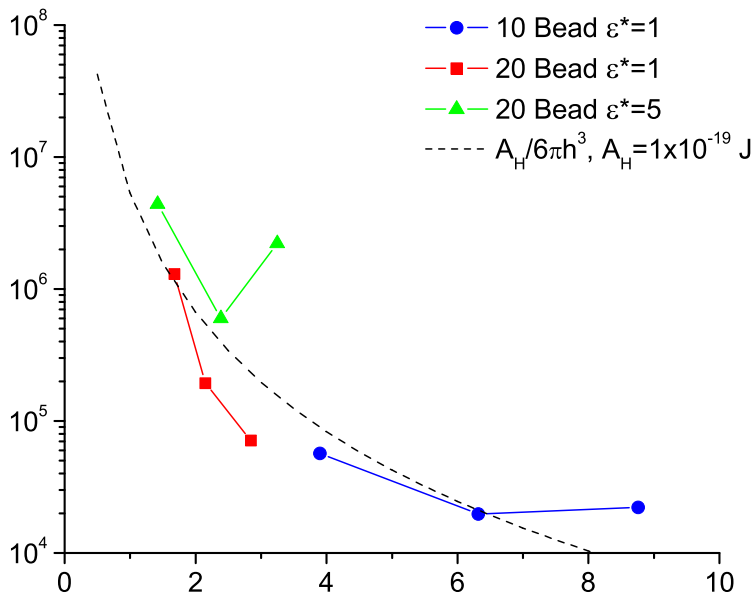


Figure 2.6: Disjoining pressure calculated directly from the MD lubricant bead-substrate interaction energies. The dashed line is calculated assuming a $1/h^3$ dependence with a Hamaker constant of 1×10^{-19} J, an experimentally-reported value. Though the calculated values lie near the experimentally-reported values, their slopes do not well match the $1/h^3$ dependence, most noticeably for the case of $\epsilon^* = 5$.

energy ϵ_{b-s} , and the end groups that have an additional energetic parameter α . The formulation in Eq. 2.9 assumes that the atoms in the film are of the same type, and so the interaction can be characterized by a single energy. By setting $\Pi = A_H/(6\pi h^3)$, A_H can be evaluated.

Recall the density profiles shown in Figure 2.3, in which the density of the fluid close to the confining wall exhibits oscillations. In very thin films, the density is inhomogeneous throughout the film; representative thin film density profiles are shown in Figure 2.7. These profiles suggest that evaluating the integral in Eq. 2.9 may not be straightforward. The simplest approach is to simply calculate an average density such that $\rho_b = \bar{\rho}_b$; the Hamaker constants calculated based on this assumption are reported in the middle column of Table 2.1, headed “Average Density”. In all cases, the Hamaker constants predicted using this approach are

Table 2.1: Hamaker constants fit to simulation data using three different methods. The values under **Energy** are based on calculating the total interaction energy between the film and substrate. The **Average Density** values arise from evaluating Eq. (2.9) with $\rho_b = \bar{\rho}_b$. The **Inhomogeneous Density** values are from the numerical integration of Eq. (2.9), making use of the calculated values of the film density ρ_b as a function of height, as shown, for example, in Figure 2.7. (There were too few numerical points to evaluate the value for the 20-bead model at $\epsilon^* = 0.5$, shown above as N/A.)

Model	Energy	$A_H \times 10^{-19}$ J	
		Average Density	Inhomogeneous Density
10-bead, $\epsilon^* = 1$	0.47	1.21	1.87
20-bead, $\epsilon^* = 0.5$	N/A	0.60	0.89
20-bead, $\epsilon^* = 1$	0.81	6.14	1.81
20-bead, $\epsilon^* = 5$	0.91	10.1	10.6

larger than those obtained using MD-predicted energies directly and, for the 20-bead models, the prediction is significantly larger than the range of values expected based on experimental results. An alternative approach is to numerically solve the integral in Eq. 2.9 using density profile data such as that shown in Figure 2.7. The disjoining pressures calculated from the density data are shown in Figure 2.8. The values of disjoining pressure for $\epsilon^* = 0.5$ and 1 lie close to the curve (shown dotted) of the disjoining pressure expected from $\Pi = A_H/(6\pi h^3)$, using the traditional constant density expression for the Hamaker constant for this geometry, $A_H = 4\epsilon_{b-s}\sigma^6\pi^2\rho_b\rho_s$, where ρ_s is the density of the substrate. In particular, the rate of change of disjoining pressure with film thickness roughly follows $\sim 1/h^3$. The best fit estimate of A_H from this calculation is given in the rightmost column of Table 2.1, headed “Inhomogeneous Density”. Again, the model with the largest interaction strength ($\epsilon^* = 5$) predicts a Hamaker constant that is too large. However, both the 10- and 20-bead models with $\epsilon^* = 1$ predict reasonable values. Though the absolute values of the disjoining pressure may be poorly resolved by relying on the density rather than directly computing energies, the results from using Eq. 2.9 preserve the shape of the curve of disjoining pressure versus height. The shape of the curve is critical for film stability. For curves that are concave downwards ($d\Pi/dh > 0$), a straight line connecting two points along the curve will lie below the curve. This implies that the film can lower its free energy by breaking into portions at the two distinct heights at which the line contacts the curve [103]. This will be seen, for example, in the formation of holes in the film and in general by the film

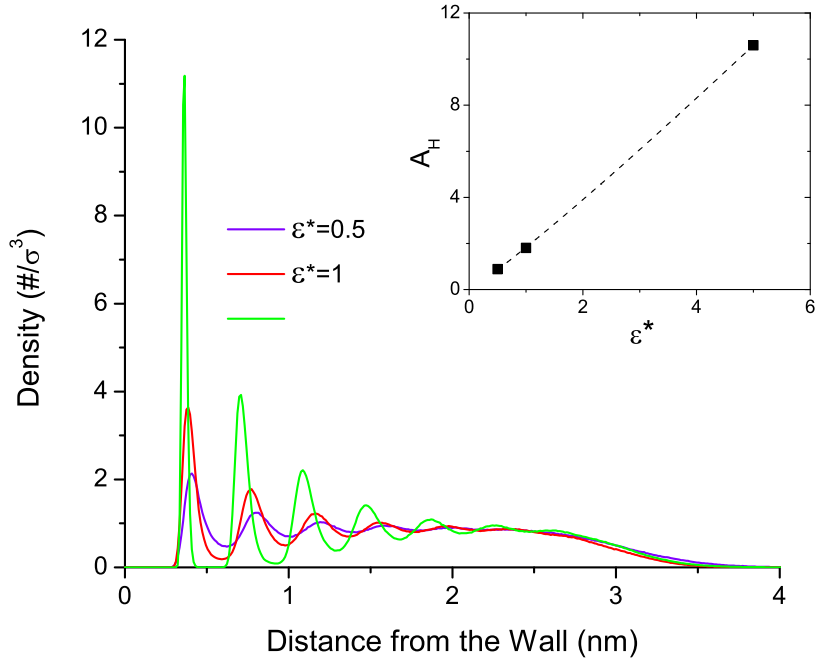


Figure 2.7: Density profile for 20-bead cases with similar film thickness but generated using models with different interaction strengths. The density is inhomogeneously distributed throughout the film thickness, with peaks in the density separated by the characteristic scale $\sigma_{20} = 0.43$ nm. Inset shows the Hamaker constant increasing with interaction strength; data from MD simulation and line represents a fit power law.

thickening and thinning inhomogeneously over the film area. For the data here, on the other hand, the energy method predicts a curve that is concave upwards, that is, $d\Pi/dh < 0$, and a uniform film thickness is stable. Eq. 2.9, preserves the negative value of this curvature and consequently, the prediction of film stability.

These results also highlight the role of interaction strength. According to $A_H = 4\epsilon_{b-s}\sigma^6\pi^2\rho_b\rho_s$, the Hamaker constant should be linearly related to interaction strength. To evaluate this in the context of our simulation data, we calculate the Hamaker constant for three different 20-bead models with different interaction strengths. The results, shown in the inset of Figure 2.7, are fit best with a power law where the magnitude of the exponent is 1.1. This indicates that increasing the interaction strength has both a direct effect on the Hamaker constant, but also an indirect effect through the density profiles. Specifically,

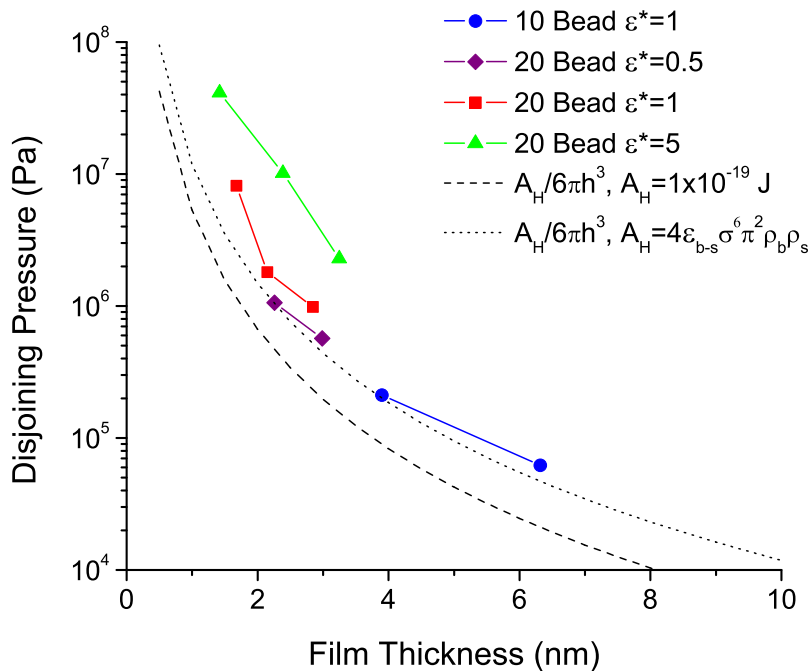


Figure 2.8: Disjoining pressure from the density measurements using Eq. 2.9. The black dashed line is the same as that in Figure 2.6 and the black dotted line is the estimate assuming a constant density of $1/\sigma^3$ across the entire film thickness and using $\epsilon^* = 1$.

increasing the interaction strength causes the density to become more inhomogeneous - a behavior that is clearly exhibited by the density profiles in Figure 2.7 - which results in a larger effective Hamaker constant.

2.4 Conclusions

Using PFPE fluids as lubricants requires that they completely cover the substrate surface, have low fluid surface roughness, and are stable. Ensuring that a film possesses all these features is particularly challenging given that it is only a few-nanometers thick. Here, we show that MD simulations with coarse-grained models can predict thin film PFPE structure and stability, quantified by the change in disjoining pressure with film thickness. A 20-bead model has been shown to well match experimentally-measured values of bulk density and surface roughness. Using this model, several methods were used to calculate disjoining pressure. The method based on the interaction between the film and substrate is

expected to give the most accurate results. However, computational resources may limit the number of data points and so lead to poor resolution. In contrast, methods based on the density distribution are much faster and simpler to use. Density-based methods capture the subtle effect of fluid-substrate interaction strength on density inhomogeneity which can become significant in very thin films. Density-based methods also correctly predict the variation in disjoining pressure with film thickness: these methods therefore can be expected to correctly predict thin film stability.

Chapter 3

SURFACE TRIBOCHEMISTRY

3.1 Introduction

Chemical reaction rates can be accelerated by supplying energy thermally, photochemically, by an external electrical potential, or mechanically, the mechanisms by which the latter operates being the least well-understood [104]. Despite this lack of understanding, over the past decades, a large number of mechanochemical syntheses have been discovered [105–109]. Most fundamental insights into how mechanical energy can accelerate a chemical reaction comes from single-molecule force spectroscopy experiments [110–112] that take advantage of the exquisite sensitivity of the atomic force microscopy. This approach enables the direction of the force to be controlled with respect to the surface-mediated molecular orientation. The results of such single-molecule pulling experiments have been analyzed theoretically using density functional theory (DFT), where, for example, it has been found that pulling alkyl thiolates from gold [113] or copper [114] causes gold atoms to be plucked out of the surface along with the alkyl thiolate group.

While such experiments and theoretical analyses provide an understanding of the effect of tensional forces, the majority of technologically important mechanochemical reactions are induced by interfacial shear, for example by ball milling or in a sliding contact, where a lubricant additive reacts with a surface to form a film that reduces friction and/or wear. Mechanochemical removal of adsorbed layers by shear has been observed in the atomic force microscope [115, 116] but the resulting small scan area precludes meaningful surface analyses of the rubbed region from being carried out. DFT analyses have also been used to examine the effect of lateral force on adsorbed layers. For example, it has been shown that shear forces on alkyl thiolates on gold cause lateral motion both of thiolate-gold entities and the surface gold layer [113] in accord with the restructuring of gold surfaces covered by sulfur-containing molecules during scanning [117].

Analyzing the chemical processes occurring at such sliding solid-solid interfaces, in particular measuring reaction rates, is the most challenging of surface chemistry problems since in situ spectroscopies, so that buried interfaces can be interrogated only using optical spectroscopies when one of the counterfaces is

transparent [118]. Although X-ray diffraction has recently been used to monitor mechanochemical reactions in situ [119], the technique is not surface sensitive. Adding to these experimental problems is the fact that frictional heating can lead to uncertainties in the reaction temperature [120] and may result in an interface in which the energy distribution is no longer described by a Boltzman probability [121].

3.2 Methods

Collaborators at University of Wisconsin-Milwaukee address these experimental challenges by using a model mechanochemical system consisting of a ball sliding on a methyl thiolate- ($\text{CH}_3\text{-S-}$) covered copper surface in ultrahigh vacuum (UHV) and by measuring mechanochemical reaction kinetics from the gas-phase products formed during sliding. A copper surface saturated with methyl thiolate species is created by exposing dimethyl disulfide ($\text{CH}_3\text{-S-S-CH}_3$, DMDS) onto an atomically clean copper foil in UHV at room temperature. The UHV chamber is equipped with a UHV-compatible tribometer in which a pin can be slid against a flat substrate. Measurements are carried out using speeds of 1 or 4×10^{-3} m/s at a preset load of 0.44 N while simultaneously monitoring the normal load (F_N), lateral force (F_L), and mass spectrometer signal. The normal load remained constant during the scan. Details on the experimental materials, setup, and procedure can be found in [3].

To supplement experimental findings, molecular dynamics (MD) simulations are performed on a system consisting of $\text{CH}_3\text{-S-}$ species adsorbed onto two copper, Cu(100), plates, Figure 3.1. The system is periodic in the plane of the $4 \times 4 \text{ nm}^2$ surfaces of the face-centered-cubic copper plates. The initial simulation structure is constructed using Accelrys Materials Studio[®], and subsequent simulations performed using Large Atomic/Molecular Massively Parallel Simulation (LAMMPS) software [100]. The Polymer Consistent Force Field (PCFF) with a global cutoff of 1.0 nm is used to describe bond, angle, torsion, and out-of-plane interactions between all atoms. A Nosé-Hoover thermostat [122] maintained the model’s temperature at 300 K and simulations are run with a time step of 0.005 fs.

An initialization process is used to create methyl thiolate-covered surfaces. First, the system is equilibrated with weak non-bonded interactions between the Cu and the S atoms from the methyl thiolate molecules. The simulation is equilibrated for 10 ps, the time required for the system to reach a stable potential energy, during which the CH_3S groups moved freely between the two Cu plates. Then, the strength of the non-bonded interactions between Cu and S is artificially increased such that the S atoms migrate towards the Cu plates. After the adsorbed system reaches a stable potential energy, the positions of the adsorbed S atoms on the plates are fixed and the Cu-S interactions reduced to their initial values.

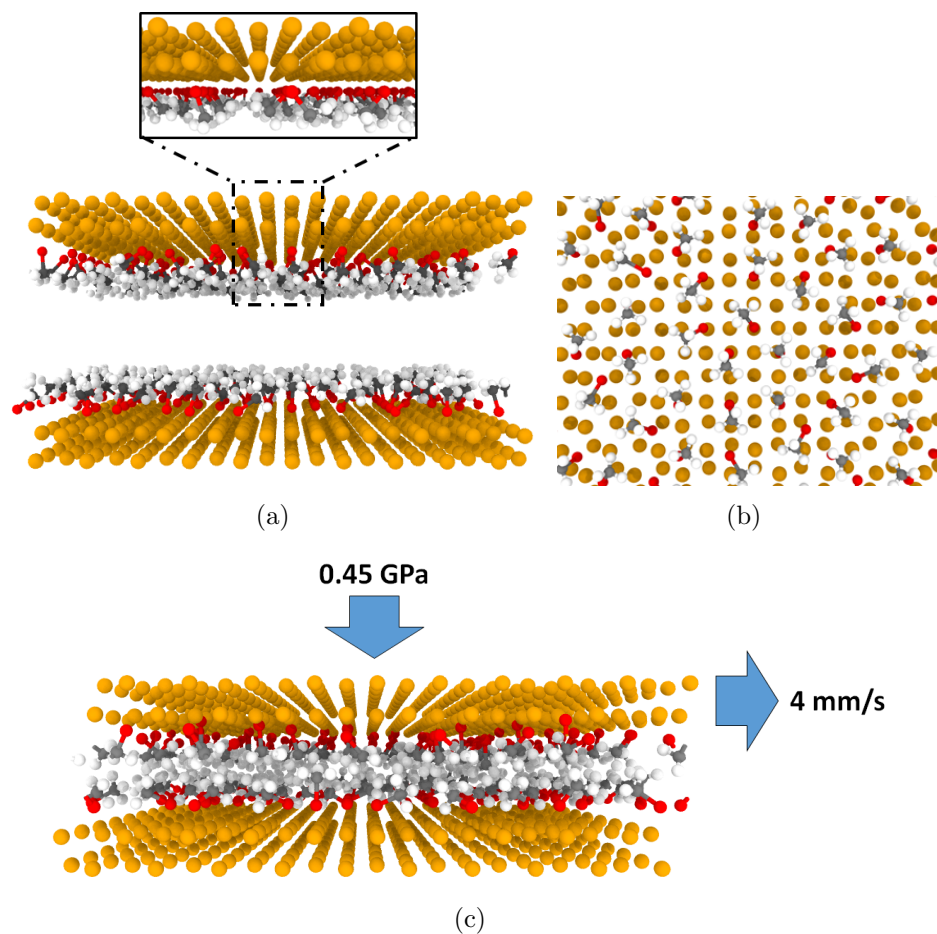


Figure 3.1: (a) Fully atomic structure of methyl thiolate covered Cu(100) plates, where the inset shows a close up of the adsorbed methyl thiolate species. (b) A top view snapshot of the adsorbed molecules. (c) A load of 0.45 GPa is imposed on the top plate and slid at a speed of 4 mm/s.

Production simulations consisted of applying load and then shear. First, a pressure of 0.45 GPa is applied to the top copper plate and the system is allowed to equilibrate for 0.35 ns, the time necessary for the force between S atoms and methyl (CH_3) groups to achieve a Gaussian distribution with zero mean force in the lateral directions. The top plate is then translated laterally with a sliding speed of 4 mm/s. The force in the sliding direction on each S-C bond is calculated at each time step. The top plate slid laterally a total of 2 nm, and the distributions of bond forces are averaged over the last 1 nm of sliding.

3.3 Results

It has been shown that DMDS initially reacts by rapidly cleaving the S-S bond to form adsorbed methyl thiolate ($\text{CH}_3\text{-S(ads)}$) species. This species decomposes thermally to evolve predominantly into methane (along with some ethylene and ethane), displaying a peak centered at ~ 425 K in temperature-programmed desorption (TPD) [123]. At room temperature, the temperature rise required to cause methyl thiolate decomposition (~ 125 K) is much larger than that caused by frictional heating, therefore any reaction products detected during sliding must be formed mechanically. By assuming a pre-exponential factor of $1 * 10^{13} \text{ s}^{-1}$ [124], a reaction activation energy for methane formation is estimated from the TPD peak temperature to be ~ 100 kJ/mol [123], giving a thermal reaction rate constant of $\sim 4 \pm 1 * 10^{-5} \text{ s}^{-1}$ at 290 K. Sliding experiments carried out in UHV at a sliding speed of $1 * 10^{-3} \text{ m/s}$ and a normal load of 0.44 N reveal the presence of methane, displayed in Figure 3.2, at room temperature during sliding, indicating that, for our system, the subsequent reaction steps after C-S bond cleavage are fast. The desorption yield, Y_n for the n th pass, for a first order reaction is given by:

$$Y_n = (1 - \exp(-k(F)t_c))(\exp(-k(F)t_c))^{(n-1)} \quad (3.1)$$

where $k(F)$ is the rate constant under the influence of a lateral force F , and t_c is the time required for the pin to traverse the contact. The data in Figure 3.2 are plotted as $\ln(Y_n)$ versus $(n - 1)$, producing a linear trend. This confirms the validity of Eq. 3.1 and yields a value of $k(F)t_c = 0.78 \pm 0.02 \text{ s}^{-1}$. Considering the various different contact modes (elastic/plastic) possible with the experimental setup, (Table 1 in [3]), the calculated mechanochemical activation energy is estimated to be 61.8-65.0 kJ/mol, smaller than the change caused by interfacial sliding (~ 100 kJ/mol). Experimental findings demonstrate that the rate of the methyl thiolate decomposition is significantly accelerated at the sliding interface. The external work carried out during sliding directly lowers the energy barrier.

MD simulations were run to analyze and characterize the force distribution on the thiolate molecules during sliding. The multiplicity of molecular contacts at the sliding interface can result in a distribution of lateral forces as found previously

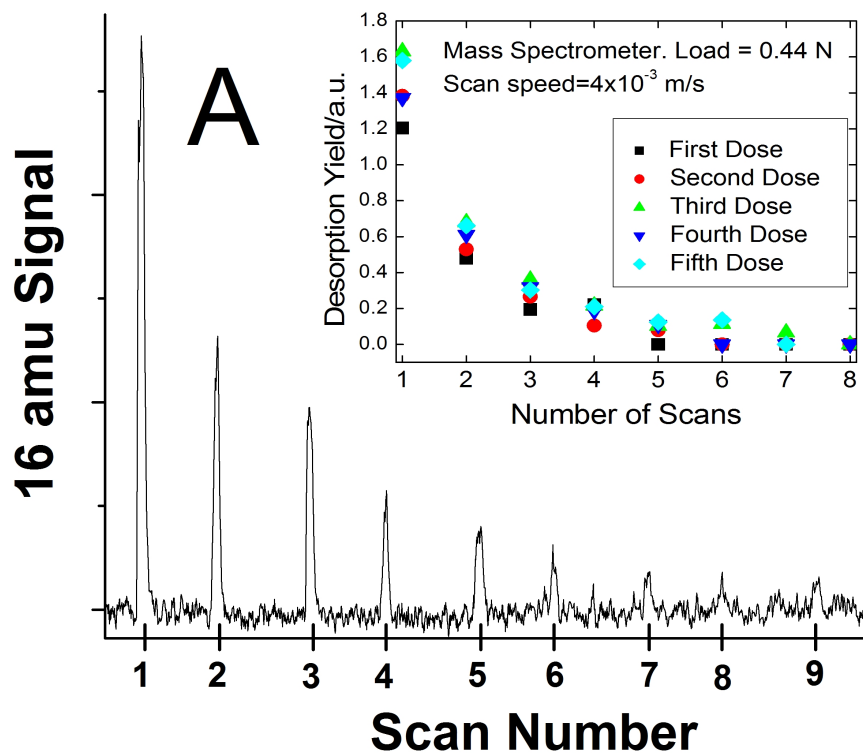


Figure 3.2: The 16 amu (methane) signal measured by sliding a tungsten carbide pin on a run-in (50 scans) clean copper foil as a function of the number of scans at a sliding speed of 1×10^{-3} m/s with a normal load of 0.44 N showing the decay in methane desorption yield as a function of the number of scans. Shown as an inset is the desorption yield measured from the area under each methane pulse as a function of the number of scans. After collecting data for the first DMDS dose, until no more methane was detected, the sample was re-saturated with DMDS and the 16 amu signal again monitored while sliding. This experiment was repeated for the third, fourth and fifth DMDS doses, where the evolution of methane yield as a function of the number of scans is identical. Experiments were performed by Dr. W.T. Tysoe's research group.

for MD simulations of organic molecules on surfaces [76,125]. The shear force per molecule is estimated as the x -directional force on the bond between the S-C atoms. This value is estimated based on the following equation:

$$f_{x-bond} = f_{total-bond} \left| \frac{x_2 - x_1}{d} \right| \quad (3.2)$$

where distance, d , is estimated from $d = \sqrt{(x_1 - x_2)^2 + (y_1 - y_2)^2 + (z_1 - z_2)^2}$, x , y , z are coordinates of atom 1 (sulfur) and 2 (carbon), f_{x-bond} is the x -directional bond force, and $f_{total-bond}$ is the total bond force. As expected, the results reveal a broad Gaussian distribution in forces acting on the S-C bonds, as shown in Figure 3.3.

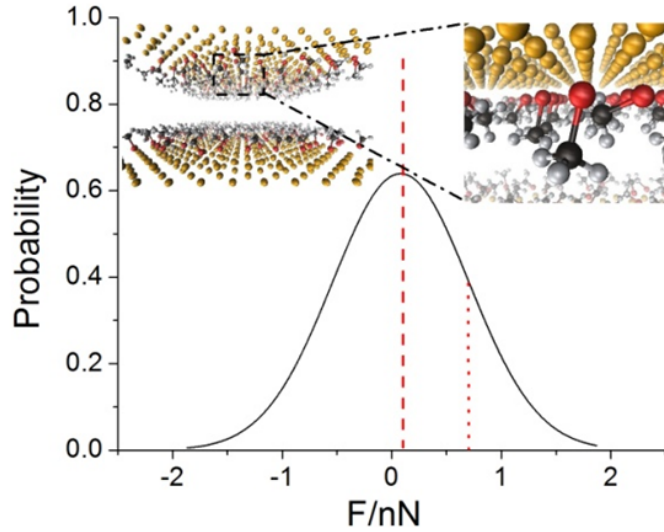


Figure 3.3: The calculated force distribution from MD simulations of methyl thiolate species on Cu(100) at a sliding speed of 4 mm/s with a contact pressure of 0.45 GPa; snapshots of the simulation are shown in the insets. The calculated average force F_0 is ~ 0.08 nN (dashed line in figure). However, the distribution of forces is Gaussian with a significant proportion of molecules experiencing much larger forces than the average value. The calculations show that $D = \sigma/F_0$, where σ is the standard deviation of the force distribution (dotted line in figure) is ~ 6.9 .

The average shear force per molecule is estimated as the mean of the x -directional bond force distribution. Based on Figure 3.3, the average calculated shear force per molecule, F_0 is ~ 0.08 nN. Defining a parameter $D = \sigma/F_0$, where σ is the standard deviation of the Gaussian force distribution and F_0 is the average

force, predicts a value of $D \sim 7$ from the MD simulations. Since MD was carried out for a relatively small contact area, such a force distribution is likely to occur not only in the micro-scale contacts present in the sliding of a pin on a copper substrate studied here but also in the nanocontact of an AFM tip. Similar calculations were also carried at higher pressures and the results are summarized in Table 3.1. The results in Table 3.1 show that contact pressure does not appear to strongly influence the value of D .

Table 3.1: Values of D obtained from MD at different normal pressures at a sliding speed of 40 m/s.

Pressure (GPa)	D
0.45	7.1
1	7.3
2	7.2
4	7.5

3.4 Discussion

The presence of a force distribution implies that there are much larger forces acting on the methyl thiolate over layer on copper than indicated by the average force. These forces are sufficiently high to enable the methyl thiols to decompose at room temperature. To explore whether the range of values of D obtained using MD simulations are sufficient to reproduce the experimentally observed activation energies, the effective rate constants $k(F)$ and the corresponding activation energies, $E_a(F)$, were calculated for a Gaussian distribution of forces.

A Gaussian force distribution $p(F)$ is found from MD simulations:

$$p(F) = \frac{1}{\sqrt{2\pi}\sigma} \exp\left(-\frac{(F - F_0)^2}{2\sigma^2}\right) \quad (3.3)$$

where F_0 is the average force and σ is the width of the distribution. Rewriting this using $D = \sigma/F_0$ gives

$$p(F) = \frac{1}{\sqrt{2\pi}DF_0} \exp\left(-\frac{(F - F_0)^2}{2D^2F_0^2}\right) \quad (3.4)$$

The activation energy varies with force as $\Delta E_a(F)$ so that the number of molecules δn that have activation barriers between $E_a(F)$ and $E_a(F) + \delta E_a(F)$ is given by $\delta n = Np(E_a(F))dE_a(F)$ where N is the total number of molecules. For a first order reaction, the reaction rate

$\delta r = Ae^{-((\Delta E_a(F))/(k_B T))} \delta n = Ae^{-((\Delta E_a(F))/(k_B T))} N p(E_a(F)) dE_a(F)$. The total rate of reaction R is obtained by integrating over all rates: $R = AN \int_0^\infty e^{-((\Delta E_a(F))/(k_B T))} p(E_a(F)) dE_a(F)$, yielding an effective, shear-induced rate constant $k(F)$ given by

$$k(F) = A \int_0^\infty e^{-((\Delta E_a(F))/(k_B T))} p(E_a(F)) dE_a(F) \quad (3.5)$$

This barrier is related to the effective activation energy (measured experimentally) through $k(F) = Ae^{-((\Delta E_a(F))/(k_B T))}$, so that

$$\exp\left(-\frac{E_a(F)}{k_B T}\right) = A \int_0^\infty e^{-((\Delta E_a(F))/(k_B T))} p(E_a(F)) dE_a(F) \quad (3.6)$$

This integral is evaluated numerically for both elastic and plastic contacts, as shown in Figure 3.4. The energy distribution $\Delta E_a(F)$ is evaluated using the Bell model and the Tomlinson/Prandtl model, where details of the evaluation available in reference [3]. For the elastic contact, Figure 3.4 (a), a comparison with the experimental value of activation energy under shear (Table 1 in reference [3]) predicts that a rather large D value of ~ 18 is required to reproduce the experimental results. For a plastic deforming contact, Figure 3.4 (b), D is estimated to be ~ 5 , much closer to MD predictions. These results indicate that the large forces present in the tail of the broad force distribution exerted on a methyl thiolate over layer at a sliding interface is responsible for the experimentally observed rate of methyl thiolate decomposition.

The larger value of D for the elastic contact can be traced to the lower value of F_0 and the behavior shown in Figure 3.4 is dominated by the width of the Gaussian force distribution. For both the plastic and elastic distribution, agreement with the experimentally measured activation energy occurs for $\sigma \sim 0.14$ nN/molecule. MD simulations predict that D should be ~ 7 (Table 3.1), which is consistent with a plastically deforming contact (Figure 3.4). Note that the value of F_0 predicted by MD simulations under conditions similar to the ones used in the experiment (0.08 nN) is very close to the value measured assuming a plastically deforming contact (0.07 ± 0.01 nN). An AFM image of the wear track (Figure S2 in reference [3]) reveals marks along the sliding direction with a root-mean square roughness of ~ 5 nm so that the sliding interface is by no means atomically smooth. Experiments to correlate the nature of the contact with various metals to their plasticity indices [126,127] indicate that copper does deform plastically in the contact [128].

3.5 Conclusion

This chapter demonstrates the mechano- and tribochemical processes occurring at sliding interfaces can be analyzed by considering the distribution of forces present at

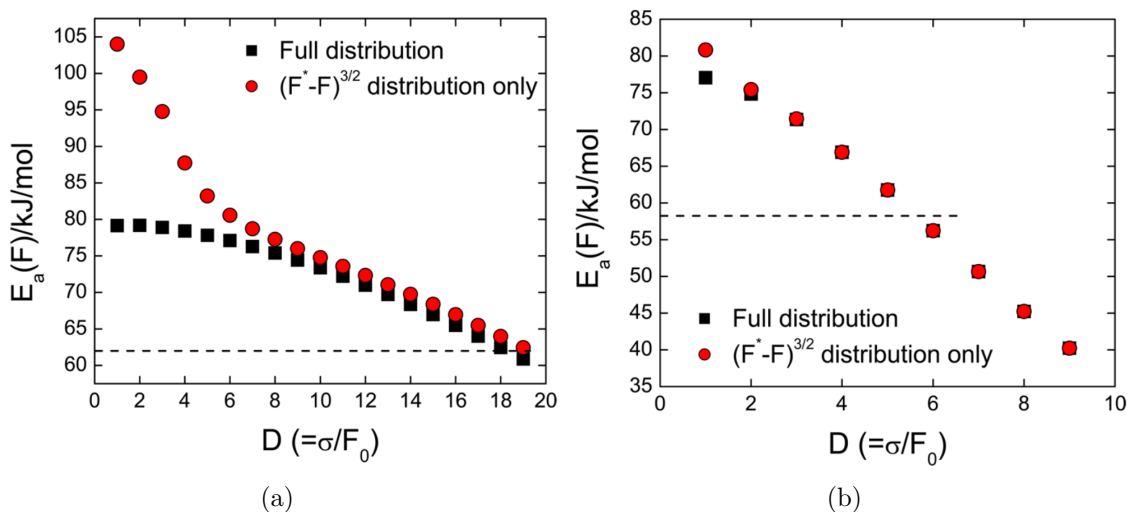


Figure 3.4: (a) A plot of the effective activation energy, $E_a(F)$, vs. D for an elastically deforming contact. Energy is estimated for a Gaussian force distribution with an average force of $F_0 \sim 0.018$ nN/molecule. The horizontal line shows the measured value of the shear-induced methyl thiolate decomposition activation energy for an elastically deforming contact. (b) A plot of the effective activation energy, $E_a(F)$, vs. D for a plastically deforming contact. Energy is estimated for a Gaussian force distribution with an average force of $F_0 \sim 0.07$ nN/molecule. The horizontal line shows the measured value of the shear-induced methyl thiolate decomposition activation energy, assuming plastic deformation at the contact. In both figures, the black squares represent energy distributions estimated using the Bell modal while the red circles represent energy distributions estimated using the Tomlinson/Prandtl model. Details on these calculations are available in reference [3]. This analysis was performed by Dr. W.T. Tysoe's research group.

the sliding interface. Only the highest forces in the tail of the distribution are capable of reducing the activation energy sufficiently to lead to measurable reaction rates at room temperature. The broad distribution results in lateral forces that are both along and opposite to the direction of motion, the average of all of these forces being the measured frictional force. This arises because of the wide range of interactions between the methyl thiolate species at the contacting interface, which will depend in detail on their relative positions as they come into contact under the influence of the normal load. The results indicate that significant mechanochemical rates can be obtained under mild sliding conditions. These results may help rationalize the intriguing discovery of graphitic tribological layers on the surface of metal-on-metal hip replacements [129, 130], which are unlikely to attain the temperatures required to thermally form such films. A combination of in situ kinetic methods and MD simulation techniques provides a platform to understand the complete picture of shear-induced mechanochemistry.

Part II

Bulk Properties of Lubricants

Chapter 4

PRESSURE-VISCOSITY BEHAVIOR OF LUBRICANTS

4.1 Introduction

Viscosity, a fluid property that describes resistance to shear, is an important characteristic in lubrication. Viscous fluids present between two contacting surfaces, in nature and machines, reduce friction and increase durability [131]. In hydrodynamic lubrication, viscosity drives the formation of a protective layer of sufficient thickness that separates the roughness of two contacting surfaces [16]. The formation and effectiveness of this layer is highly dependent on the effects of pressure, temperature, and shear rate within the interface on viscosity [24–26]. The increase of viscosity with pressure can significantly affect interface performance, particularly at the high pressures of elastohydrodynamically lubricated interfaces, and even in plain bearings [132]. The rate at which a lubricant’s viscosity increases with pressure is usually characterized by a pressure-viscosity coefficient, a material-specific constant derived from experimental viscosity data.

The pressure-viscosity response (PVR) of a fluid is a function of its chemical structure and composition [26], so obtaining pressure-viscosity coefficients for real lubricants usually requires highly accurate experiments to be performed for each fluid composition. To address this issue, it is desirable to be able to predict PVR efficiently using models. Such models can be divided into two categories, atomistic and empirical. Atomistic models, such as MD simulation, provide explicit representation of molecular structure as well as chemistry and can be used to predict PVR for nanoscale volumes of fluid. Empirical models, on the other hand, are mathematical equations developed from experimental observations that relate PVR to other material-specific properties. As discussed next, there are advantages and disadvantages to each of these approaches and neither approach has been thoroughly validated.

MD simulations explicitly describe the molecular structures of fluids and predict the evolution of those structures over time. The high level of detail available from these simulations provides a means of leveraging the relationship between molecular structure and material properties. Viscosity (and so PVR) can be calculated directly from such simulations using either equilibrium (EMD) or non-equilibrium (NEMD) methods, however, there are limitations with both

approaches. Viscosity predictions through EMD are estimated at zero shear rate from either the Einstein relation or the Green-Kubo equation, both of which require the computation of time correlation functions. The accuracy of these functions depends on the size of the system used as well as the length of the relaxation time [69, 133, 134]. Since size and relaxation time are influenced by structure, computing viscosity using EMD can be prohibitively time intensive, particularly for complex lubricants [69]. NEMD viscosity predictions are based on stress-strain relationships and are computed for systems subject to non-zero shear rates. However, due to the timescale limitations of MD in general, such simulations must be run at unrealistically large shear rates for reasonable simulation durations [135]. There are then issues with extrapolating these results to lower shear rates since shear thinning can occur at the large shear rates (larger than the inverse rotational-diffusion time) accessible to MD simulations that is not reflected in typical low shear rate experimental measurements [136].

The alternative to MD-based approaches for predicting PVR is the use of empirical correlations [137–140]. These correlations are usually derived from experimental observations and enable PVR to be estimated from other material properties such as temperature-viscosity relationships, pressure-density relationships, and temperature-density relationships [137, 139]. While these equations are a simpler option, they do not explicitly capture the dependence of PVR on molecular structure. Predictions from some of these models also have large errors, particularly if the fluid for which PVR is being predicted is very different from the fluids to which the models were fit [139]. More importantly, these equations rely on experimental material property data, which limits their application for new lubricant mixtures unless prior experimental information is available.

Based on our evaluation of currently available methods, it is clear that there are pros and cons to estimating PVR using either MD simulations or empirical equations. MD simulations have structural precision that capture specific features of fluid molecules, but direct viscosity predictions demand large simulation sizes and long computational time, especially for complex fluids. Empirical models, on the other hand, are usually simple and straight forward mathematical equations, but they rely on experimental data and do not provide any insight on the dependence of molecular structure to pressure-viscosity behavior. To capitalize on the advantages of both methods, it would be beneficial to predict PVR from empirical models using MD predicted material properties, eliminating the need for experimental data.

This is the approach explored here. Specifically, we use a recently-proposed empirical viscosity correlation to predict piezoviscous behavior from ambient viscosity and pressure-volume data [141]. A key feature of this approach is that the pressure-volume data can be relatively easily obtained from MD simulations, therefore obviating the need for any high pressure experimental data to predict

viscosity. The new method is evaluated in two stages. First we evaluate the accuracy of the proposed viscosity correlation in terms of its ability to predict piezoviscosity from experimentally-measured pressure-volume data. Second, pressure-volume data from MD simulation is used as input into the viscosity correlation to predict pressure-viscosity behavior. The ability of the model to make accurate predictions is found to vary from fluid to fluid. The limitations of the model are analyzed in terms of potential sources of error and potential means of minimizing the error are discussed.

4.2 Methods

4.2.1 Empirical Model

Recently a new empirical correlation was proposed that provides a bridge between two very different regimes of pressure-temperature-viscosity behavior for non-associating liquids [141]. These are the low viscosity regime where the temperature dependence is Arrhenius and the pressure dependence is roughly linear and the high viscosity regime where the temperature dependence is super-Arrhenius and the pressure-dependence is roughly exponential. This correlation is given by [141]

$$\eta = A \exp(B\beta_V^q + C\beta_V^Q), 0 < q < 1, 1 < Q \quad (4.1)$$

where η is viscosity, A , B , C , are various constants, q , Q are power-law exponents, and β_V is the normalized Ashurst-Hoover scaling parameter

$$\beta_V = \left(\frac{1}{T}\right) \left(\frac{V_{molec}}{V}\right)^\gamma \quad (4.2)$$

where T is temperature, V_{molec} is the specific volume of a single molecule, V is volume, and γ is the thermodynamic interaction parameter. A , B , C , q , Q , and γ are material specific constants [141] Eq. 4.1 represents a complete range of compressed fluid response and creates a master Stickel plot in which the points represent the location of the data rather than a fitted model. In addition, it also has an added advantage of not having singularities, a long standing problem for free-volume formulations in numerical simulations of elastohydrodynamic lubrication regimes [141]. Viscosity predictions made using Eq. 4.1 have been shown to be very accurate for several different liquids, from a refrigerant to a viscous diester [141]. However, the applicability of this method requires prior knowledge of material specific parameters, thus limiting this approach to fluids with accessible or readily available B , C , q , and Q values.

In this work, we extend the potential utility of the method by assuming that B , C , q , and Q are universal constants for lubricant-like species. We identify values of B , C , q , and Q by fitting Eq. 4.1 and 4.2 to experimentally-measured data for

squalane and diisodecyl phthalate, two commonly used reference fluids [141]. The parameters derived from fitting are $B = 44.52$, $C = 2.36E7$, $q = 0.094$, $Q = 2.18$ such that Eq. 4.1 becomes

$$\eta = A \exp(44.5\beta_V^{0.094} + 2.36e7\beta_V^{2.18}) \quad (4.3)$$

For a given fluid, we can fit values of the remaining constants, A and γ , using easily-measured ambient viscosity and volume. Then, Eq. 4.3 can be used to predict the piezoviscous response of that fluid from its pressure-volume behavior.

Several different variables have been proposed to capture the PVR of a fluid, including the conventional pressure-viscosity coefficient, α_0 , the secant pressure-viscosity coefficient, α_B , Blok’s reciprocal asymptotic isoviscous pressure coefficient, α^* , and the modified Blok’s coefficient, α_{film} [132, 140]. Here, we use Blok’s reciprocal asymptotic isoviscous pressure coefficient, α^* given by [140]

$$\alpha^* = \left[\int_0^\infty \frac{\eta(P=0)dP}{\eta(P)} \right]^{-1} = \left[\frac{\eta_0}{\alpha_N \eta_N} + \sum_{i=1}^N \frac{\eta_0}{\alpha_i} \frac{\eta_i - \eta_{i-1}}{\eta_i \eta_{i-1}} \right]^{-1} \quad (4.4)$$

where η_i is viscosity at pressure P_i and $\alpha_i = \frac{\ln(\eta_i/\eta_{i-1})}{P_i - P_{i-1}}$. α_N and η_N are the pressure-viscosity coefficient and viscosity at the N -th pressure, respectively.

4.2.2 MD Simulation

Pressure dependent volume data can be obtained from MD compressibility simulations. Compared to EMD and NEMD simulations for predicting viscosity, compressibility simulations can be performed with relatively small model systems and do not depend on relaxation time, enabling them to be performed within relatively short durations. Recently we developed a simulation method that successfully predicted the compressibility of several model lubricants [142, 143]. We will employ a similar approach here to estimate changes in density with pressure for 9-N-octylheptadecane (TOM) and 1-cyclopentyl-4(3-cyclopentylpropyl)dodecane (CPD).

The molecular structure of TOM and CPD, given in Fig. 5.1(a), and simulation system, Fig. 5.1(b), are constructed with Accelrys Materials Studio[®]. Subsequent simulations are implemented using Large Atomic/Molecular Massively Parallel Simulation (LAMMPS) software [100]. The system has periodic boundary conditions with initial dimensions of 4.0 nm \times 4.0 nm \times 4.0 nm. The All Atom Optimized Potentials for Liquid Simulations (OPLS-AA) force field [68] with a global cutoff of 1.2 nm is used to describe bond, angle, torsion, and non-bonded interactions between all atoms. A Noé-Hoover thermostat and barostat are used to control temperature and pressure [122]. All simulations are run with a time step of 0.25 fs and a 1-4 intramolecular van der Waals scaling factor of 0.0 [144].

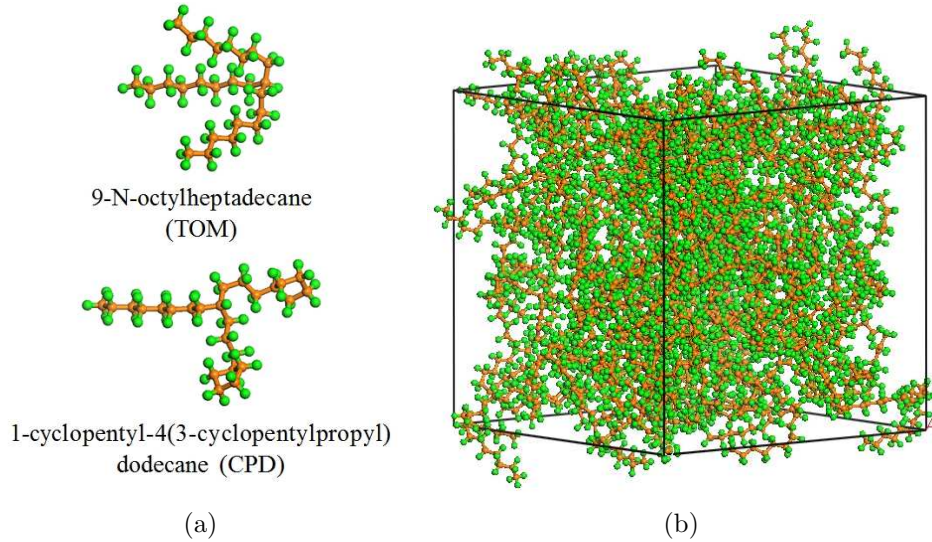


Figure 4.1: (a) Fully atomistic structure of TOM and CPD (b) Cross sectional view of the initial configuration of the model where the black line indicates the periodic boundary. Colored spheres represent individual atoms: Orange-carbon and green-hydrogen

The simulation cell is equilibrated under NVT (constant number of atoms, volume, and temperature) conditions, where temperature is set at 1000 K, for approximately 125 ps, followed by NPT (constant number of atoms, pressure, and temperature) conditions, where pressure is set to 1 atm and temperature is kept constant at 300 K, for 5 ns. The initial density of the system is averaged over the last 0.5 ns of the NPT equilibrate stage. Compression is then induced on the system, where the dimension of the simulation box is reduced at a constant engineering strain rate of 0.0001 ns^{-1} in all three dimensions, to a maximum pressure of 400 MPa. At this strain rate, the x -, y -, and z - dimensions of the box are reduced to a maximum of 4.5% of their initial length. During this compression process, 6 different simulation sizes are selected for further analysis. Each compressed system is re-equilibrated under NVT conditions at a temperature of 300 K for an additional 0.5 ns and average pressure estimations are taken over the last 0.25 ns.

V_{molec} , the specific volume of a single molecule, can also be estimated from the simulations. Here, V_{molec} is estimated using the Connolly Volume Computation method [145] available in the Atom Volumes and Surfaces tool in Materials Studio[®]. The Connolly Volume Computation method is a geometric computation method that estimates volume-based information using analytical partition calculations [145]. A

probe-like sphere scans the molecule to provide volume estimations. Variations in the probe radius provides different volume information, such as van der Waals volume, solvent-excluded volume, and interstitial volume [145]. In this work, the probe radius is set to zero and V_{molec} is estimated as the van der Waals volume of a single molecule.

4.3 Results

4.3.1 Accuracy of the General Correlation

The capability of the general viscosity correlation to make accurate predictions is evaluated for five fluids: di-(2ethylhexyl)-sebacate (DOS), 1-cyclohexyl-3(2-cyclohexylethyl) hendecane (CHH), 9-N-octylheptadecane (TOM), 1-cyclopentyl-4(3-cyclopentylpropyl) dodecane (CPD), and 80W-90. For these molecules, A and γ are estimated from fitting to temperature-viscosity and temperature-volume data (0 - 120 °C) at atmospheric pressure ($P = 0$ MPa); data for DOS, CHH, TOM, and CPD is available in the 1953 ASME Pressure-Viscosity Report [4] and for 80W-90 in previous technical reports [6, 7] as well as in the Appendix of this chapter. V_{molec} is estimated from fitting pressure-temperature-volume and pressure-temperature-viscosity data [4, 6, 7] to the Doolittle Equation [140]. Table 4.1 lists the parameters in Eq. 4.2 and 4.3, and Table 4.2 reports the predicted PVR at various temperatures. The predictions for CHH have the largest error, $\sim 20\%$ at 0°C, while predictions for 80W-90 have the smallest error, $\sim 0.4\%$ at 50°C. These results show that, although the model predictions are reasonable, the accuracy of the method varies from fluid to fluid and none of the predictions are perfect. The observed error may be due to inaccuracies in the form of Eq. 4.3, the fit universal constants in that equation, or the value of V_{molec} . These will be discussed further in the next section.

Table 4.1: V_{molec} , A , and γ values required to predict PVR for DOS, CHH, TOM, CPD, and 80W-90

Molecule	V_{molec} (cc/g)	A	γ
DOS	0.6602	$8.257e-12$	3.568
CHH	0.8756	$1.257e-11$	6.072
TOM	0.7673	$8.257e-12$	3.88
CPD	0.7646	$7.471e-12$	4.136
80W-90	0.699	$1.190e-9$	4.402

Table 4.2: Predicted α^* for DOS, CHH, TOM, CPD, and 80W-90 are compared to reported literature values [4, 6] (literature values in brackets)

Temperature °C	DOS (GPa ⁻¹)	CHH (GPa ⁻¹)	TOM (GPa ⁻¹)	CPD (GPa ⁻¹)	80W-90 (GPa ⁻¹)
0	13.94 (17.15)	33.77 (27.97)	15.25 (13.93)	18.88 (19.29)	-
20	-	27.57 (23.80)	12.69 (13.11)	15.93 (16.96)	-
25	11.50 (14.21)	-	-	-	-
30	-	-	-	-	23.82 (23.61)
38	11.26 (12.68)	24.79 (21.21)	11.78 (11.93)	14.48 (15.13)	-
50	-	-	-	-	20.80 (20.88)
80	-	-	-	-	17.48 (17.27)
99	8.48 (8.96)	14.02 (14.48)	9.29 (8.66)	10.33 (10.56)	-
120	-	-	-	-	14.58 (13.98)

4.3.2 Accuracy of the General Correlation with MD Data

Next, the general viscosity correlation, Eq. 4.3, is tested using pressure-volume data obtained from MD compressibility simulations of TOM and CPD at 20°C. When a system is compressed, its volume decreases with increasing pressures. Fig. 4.2 shows these expected trends for TOM and CPD predicted by both MD simulations and the experimentally-fit [4] Tait equation. V_{molec} is calculated as described in the Methods section using the Connolly Volume Computation. Then, using the simulation-predicted V_{molec} and ambient viscosity/volume data from experiment, we re-fit A and γ . Finally, we can predict PVR using Eq. 4.3 with the simulation predictions shown in Fig. 4.2. The results are summarized in Table 4.3.

The model predictions with the simulation data are less accurate than those predicted by the viscosity correlation with experimental volume data. To understand

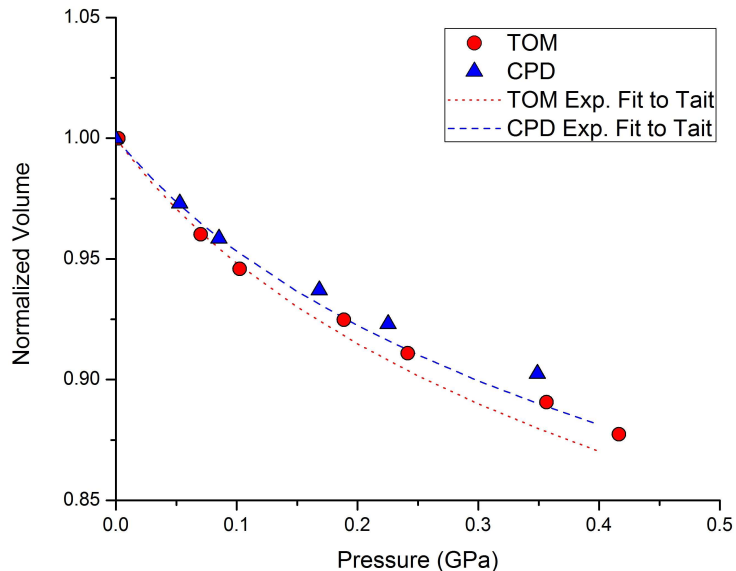


Figure 4.2: Normalized volume (normalized by ambient volume) versus pressure plots for TOM and CPD. Symbols represent MD data and the dashed lines represent the Tait equation fit to experimental data [4]

the observed error, we consider its possible sources, the empirical equation and MD simulations. The contribution of these to the overall error can be isolated by calculating PVR with various combinations of input data. The results are shown in Table 4.4.

The best predictions are made, as expected, using the experimental data. As mentioned previously, the error that is observed in these cases is attributable to Eq. 4.3 itself, the universal constants, or the value of V_{molec} obtained by fitting experimental data to the Doolittle equation. The form of the equation, which combines two exponential power law terms, creates a viscosity master curve and is able to capture the Stickel curve up to high compressions. Additionally, this equation also includes molecular volume characteristics, V_{molec} , which makes it robust and transferrable to specific molecules [141]. Therefore, this is not expected to be a major source of error. The accuracy of the constants may be improved slightly by fitting them to data from more fluids. However, we have found that the best fit values of B , C , q , and Q are relatively constant for the different fluids we considered here. Lastly, the molecular volume obtained from a fit to the Doolittle equation. The Doolittle equation is known to be limited in its ability to reproduce experimental accuracy [146]. Therefore, we expect this to be the primary source of error associated with correlating experimental pressure-volume data to PVR.

Table 4.3: V_{molec} , A , γ , and α^* values predicted by MD for TOM and CPD. α^* predictions are compared to reported literature values [4]

Molecule	V_{molec} (cc/g)	A	γ	α_{MD}^* (GPa^{-1})	$\alpha_{Lit.}^*$ (GPa^{-1})
TOM	0.7520	$7.471e-12$	3.690	11.44	13.11
CPD	0.7203	$5.425e-12$	3.530	12.71	16.96

Table 4.4: Predicted α^* and the resulting error in those predictions for TOM and CPD using $P - V$ and V_{molec} from either experiment or MD simulation

Molecule	V_{molec}	$P - V$	α^* (GPa^{-1})	$\alpha_{Lit.}^*$ (GPa^{-1})	Error %
TOM	Exp	Exp	12.69		3.2
	MD	Exp	12.2	13.11	6.9
	Exp	MD	11.92		9.1
	MD	MD	11.44		12.7
CPD	Exp	Exp	15.93		6.1
	Exp	MD	14.63	16.96	13.7
	MD	Exp	13.75		19
	MD	MD	12.71		25.1

Introducing MD simulation into the method increases the error in the predicted PVR. This error is attributable to two factors, the molecular volume and and pressure-volume data. Comparing the pressure-viscosity coefficient predictions with V_{molec} from MD and $P - V$ from experiment to those with V_{molec} from experiment and $P - V$ from MD in Table 4.4 reveals that the error in the pressure-volume data is greater for TOM, while the error in the molecular volume is greater for CPD. In both cases, the error associated with the V_{molec} is reasonable in the sense the this value is well-known to significantly depend on the details of its calculation, and there is no standard method. In fact, it was shown that molecular volume predictions from several different commonly-used software packages (Materials Studio, PcModel, and TSAR) are inconsistent, primarily because of different atomic radii used in the volume computation method [147]. In general, there may be issues with the limited ability of V_{molec} to capture the role of molecular size in resisting intermolecular motion; e.g. the molecular volume of a ringed structure may exclude the volume in the center of the ring, but that volume is not available for neighboring molecules to occupy. The error associated with the pressure-volume predictions may be due to limitations of the empirical potential

that describes the atomic interactions and behavior of bonds. The empirical model used here, OPLS, is parameterized (fit to experimental data or first principles calculations) under ambient conditions [68]. This can limit its ability to accurately predict the conformation of molecules under high pressures. Going forward, this may be addressed by identifying alternative empirical models tuned for pressurized systems or fitting such a model specifically for this purpose.

4.4 Conclusions

This chapter presents a method to predict PVR from empirical models using MD predicted material properties. Specifically, we use a recently-proposed empirical viscosity correlation to predict pressure-viscosity behavior from ambient viscosity and pressure-volume data. The method takes advantage of the molecular-scale features of MD simulation and the ability of empirical models to relate PVR to properties easily accessible using MD. The accuracy of the proposed method is evaluated with experimentally-measured data and MD derived data. The errors observed as well as the limitations of the method are then discussed in detail. Regardless of the errors observed, the method presented in this study, which combines MD simulation with empirical model, holds significant promise. Once optimized, this approach can be further developed to make accurate PVR and pressure-viscosity coefficient predictions for molecules with varying chemical structures. The proposed method provides a means of fundamentally understanding the relationship between a fluid’s molecular structure and its pressure-viscosity behavior.

4.5 Appendix

Table 4.5: Viscosity for 80W-90 [6]

Pressure (MPa)	Temperature (°C)			
	30	50	80	120
0	232	73.7	20.08	6.98
50	797	224	52.6	15.51
100	2372	594	117.2	30.2
150	6838	1417	240	55.2
250	48661	7520	928	158.1
500		375318	22072	1839
750		solid	407406	14792
1000			8283860	123772
1200				678516

Table 4.6: Calculated relative volume for 80W-90 [7]

Pressure (MPa)	Temperature (°C)			
	30	50	80	120
0	0.9856	1	1.0216	1.0503
50	0.9600	0.9718	0.9890	1.0110
100	0.9404	0.9506	0.9652	0.9836
150	0.9245	0.9336	0.9466	0.9627
250	0.8996	0.9073	0.9182	0.9315
500	0.8578	0.8637	0.8720	0.8819
750	0.8300	0.8350	0.8419	0.8501
1000	0.8091	0.8135	0.8196	0.8267
1200	0.7954	0.7995	0.8051	0.8115

Chapter 5

EFFECT OF MOLECULAR-SCALE FEATURES ON THE POLYMER COIL SIZE OF MODEL VISCOSITY INDEX IMPROVERS

5.1 Introduction

Viscosity index improvers (VII) are an important class of additives that decrease the change of fluid viscosity with temperature [45, 148], enabling optimum lubricant performance over a wider range of operating temperatures. These additives are typically high molecular weight polymers [1, 8, 149], such as olefin copolymer, polyalkylmethacrylates, polyisobutylenes, styrene block copolymer, and ethylene alpha olefin copolymers [1, 20, 45]. Over the years, advancements in VII technology have been focused on either modifying chemistries [150–152] or manipulating the structure and architecture [153–155] of traditional VII polymers. These variations not only improve viscosity index performance, but in some cases also boost shear, thermal, and oxidative stability of the lubricating oil [150, 154–156].

The mechanism behind the functionality of VII additives is still poorly understood. The most commonly accepted theory is the coil expansion mechanism, which was first introduced in 1958 by Selby [48]. Based on this theory, it is proposed that at lower temperatures, the polymer is poorly soluble in the lubricating oil and tends to stay in a coiled conformation. In this state, the polymer does not contribute much to fluid viscosity. At elevated temperatures, the solubility of the polymer in the lubricating oil improves. The polymer expands and induces a thickening effect on the solution, therefore reducing the decline of fluid viscosity with temperature. While this idea is widely accepted in the literature [1, 8, 45, 149, 153, 157, 158], there is little direct evidence to support it.

Several studies have been performed to evaluate the proposed coil expansion theory [24, 159–161]. In these studies, changes in the size of a polymer coil in solution can be determined using direct or indirect measurement methods. In the direct approach, experimental techniques, such as small angle neutron scattering, static laser light scattering, dynamic laser light scattering, or size exclusion chromatography, are used to measure coil size [24, 160]. The indirect methods infer polymer coil size from measured viscosity data, sometimes using

empirical correlations, such as Einstein’s equation or the Flory-Fox equation [24, 159, 161]. These studies have shown that not all VII polymers exhibit coil expansion with increased temperatures [24, 159–161]. In fact, the coil size of some VII polymers, such as olefin copolymers, hydrogenated diene copolymers, and styrene butadiene copolymers, remain constant or decrease with increasing temperature. So far, only VII additives derived from polyalkylmethacrylate chemistry appear to comply with the classical theory, where the coil size of the polymer increases with increasing temperature [24, 159–161].

In this work we explore trends in polymer coil size using molecular dynamics (MD) simulation. We use MD simulations to observe and characterize temperature-induced changes in the radius of gyration for several model VII polymers. MD predicted trends are compared to experimental data available in literature to partially validate the proposed method. Additionally, the simulations are also used to explore the effects of polymer chemistry on temperature-induced coil size behaviors. Our findings indicate that polymer size at a given temperature depends on specific atomic-scale features and suggests avenues for further exploration of these dependencies.

5.2 Methods

Two model VII additives, random ethylene-propylene copolymer (OCP) and polydodecylmethacrylate (PMA), illustrated in Fig. 5.1(a) and (b), are used in this work. Both structures are 50 repeat units long where OCP has a molecular mass of 1755.39 g/mol and PMA has a molecular mass of 12722.7 g/mol. The OCP model is constructed with 50/50 mole ratio of ethylene to propylene monomers. Each model VII polymer is placed in a dodecane solvent, as illustrated in Fig. 5.1(c). The initial configurations of all models are constructed with Accelrys Materials Studio[®]; a representative image of PMA in dodecane is shown in Fig. 5.1(d). Subsequent simulations are implemented using Large Atomic/Molecular Massively Parallel Simulation (LAMMPS) software [100]. The simulation systems have periodic boundary conditions with initial dimensions of 6.0 nm \times 6.0 nm \times 6.0 nm. The All Atom Optimized Potentials for Liquid Simulations (OPLS-AA) force field [68] with a global cutoff of 1.2 nm is used to describe bond, angle, torsion, and non-bonded interactions between all atoms. A Noé-Hoover thermostat and barostat are used to control temperature and pressure. All simulations are run with a time step of 1.0 fs and a 1-4 intramolecular van der Waals scaling factor of 0.0. This scaling factor has been shown to increase the accuracy of density predictions for molecules with more than 12 carbon atoms [144].

The simulations have three stages, relaxation, equilibration and production, as shown in Table 5.1. First, the simulation is run under NVT conditions (constant number of atoms, volume, and temperature) at a high temperature to rapidly relax

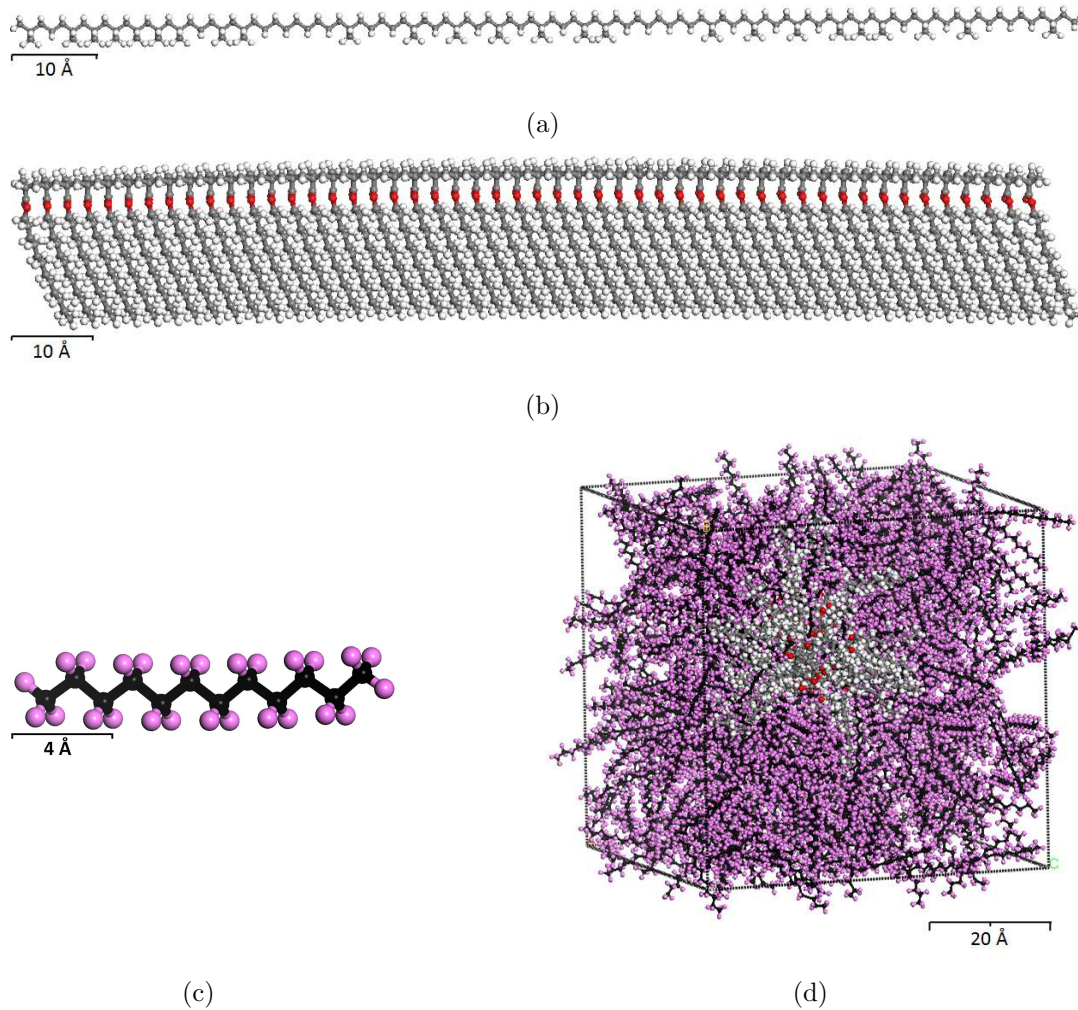


Figure 5.1: Atomic structures of the model (a) random ethylene-propylene copolymer, (b) polydodecylmethacrylate polymer, and (c) dodecane. (d) Initial configuration of the polydodecylmethacrylate molecule in dodecane solvent, where the dotted black lines indicate the periodic boundary. For all figures, colored spheres represent individual atoms: grey/black-carbon, white/pink-hydrogen, and red-oxygen

the system. Next the simulations are equilibrated under NPT conditions (constant number of atoms, pressure, and temperature) at 40°C and 100°C, but no data is collected. Lastly, during the production stage, the simulation continues to run under NPT conditions, but data is collected for further analysis.

Table 5.1: Outline of the various stages of the simulations

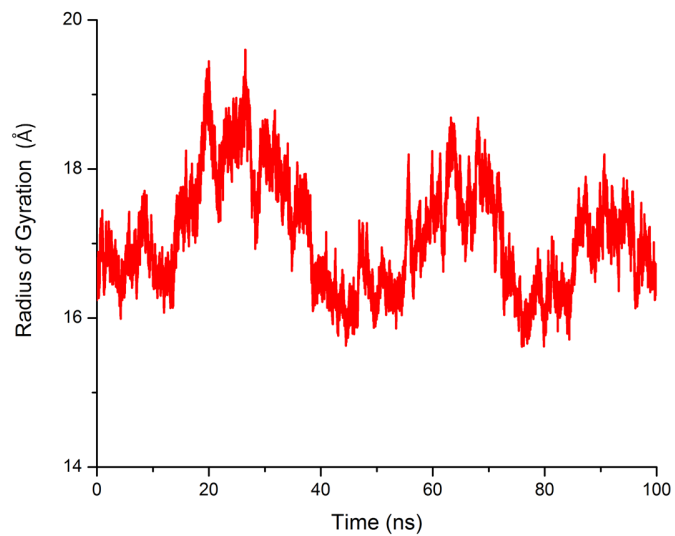
Process	Ensemble	Pressure (atm)	Temperature (°C)	Time (ns)
Relaxation	NVT	-	727	0.5
Equilibration	NPT	1.0	40 or 100	3.0
Production	NPT	1.0	40 or 100	100.0

The polymer size is quantified by its radius of gyration, R_g , which is calculated throughout the production simulation. The R_g varies over time as the polymer moves and changes its conformation, as presented in Fig. 5.2(a). Therefore, the raw data is used to plot frequency histograms, Fig. 5.2(b), that capture the recurrence of specific conformations. A Gaussian function is then fit to the histograms to quantify the mean, μ , and standard deviation of the distributions. While the Gaussian function may not be the best fit for all histograms, it provides a reasonable means to quantitatively compare the differences between different models and temperatures. Lastly, the percent change in the polymer coil size with temperature is estimated from the mean of the distribution using $(\mu_{100^\circ C} - \mu_{40^\circ C}) / \mu_{40^\circ C} \times 100$.

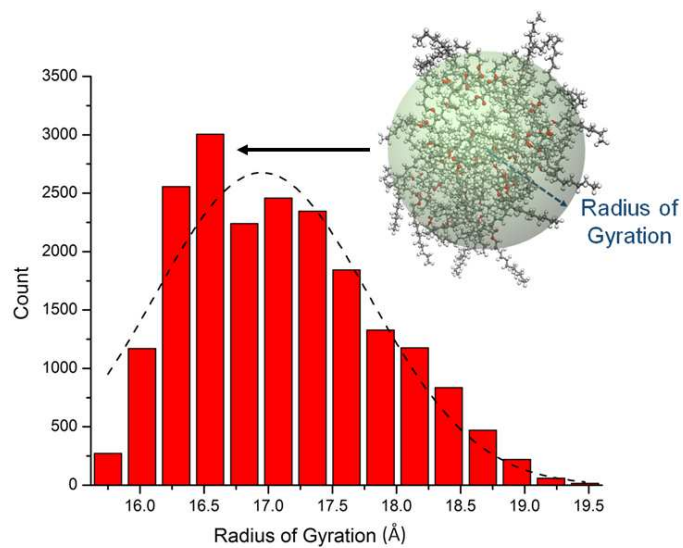
5.3 Results and Discussion

Fig. 5.3 shows the frequency histograms for PMA and OCP at 40°C and 100°C. The mean and standard deviation of the Gaussian fit to the distributions are reported in Table 5.2. The mean R_g of PMA clearly increases when temperature is increased, which means that this polymer is experiencing an increase in coil size with temperature. The standard deviation of PMA is also larger at 100°C compared to 40°C (3.0 vs. 0.7), implying that PMA is able to assume more conformations at the higher temperature. The mean R_g of OCP, on the other hand, has a similar value at both low and high temperatures, indicating that the coil size of OCP does not change significantly with temperature. The standard deviation of the OCP R_g is also similar at both temperatures (3.6 vs. 3.7), indicating that this polymer has similar number of available conformations at high and low temperatures.

Table 5.2 also reports the percent change in polymer coil size with temperature. PMA has a positive percent change while OCP has a negative

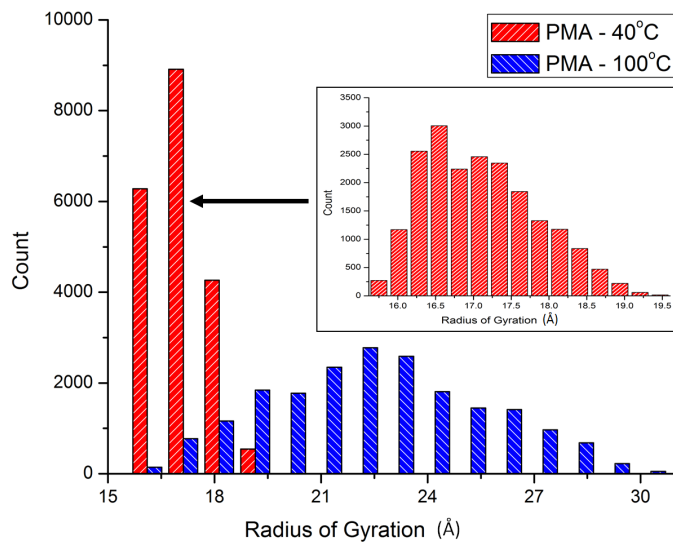


(a)

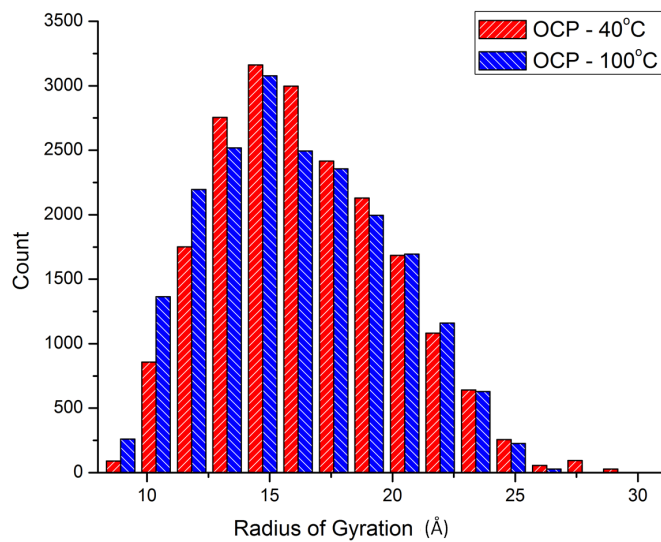


(b)

Figure 5.2: (a) Changes in R_g over time as the polymers moves and changes conformations (b) Frequency histogram plotted from raw R_g data. The dotted line represents a Gaussian fit to the histogram data.



(a)



(b)

Figure 5.3: Frequency histograms of (a) PMA and (b) OCP at 40°C and 100°C. Gaussian functions are fit to these histograms to obtain information on the mean and standard deviation of the distribution

Table 5.2: Mean and standard deviation of the R_g distribution for PMA and OCP at 40°C and 100°C as well as the percent change in polymer coil size with increased temperature

Temperature (°C)	PMA (Å)	OCP (Å)
40	17.1 ± 0.7	16.5 ± 3.6
100	22.5 ± 3.0	16.1 ± 3.7
Change (%)	31.5	-2.2

percent change when temperature is increased from 40°C to 100°C. This trend reflects coil size expansion for PMA and slight coil size contraction for OCP.

Changes in the coil size of PMA and OCP in a dodecane solvent have been recently studied using small angle neutron scattering [160]. The study reported that the size of PMA increased with temperature (by 6.2 or 11.6%, depending on the type of alkylmethacrylate monomer used), while the size of OCP decreased with temperature (-10.5%). These trends are comparable to our MD predicted results, in which PMA showed a positive percent change and OCP showed a negative percent change. The difference in the magnitude of the change between simulation and experiment may be due to variations in the size and structure of the VII polymers used in our work and in reference [160]. Similar trends were also observed in other studies for multiple variations of PMA and OCP chemistries [24, 159–161].

The two most significant differences between PMA and OCP are the presence of long side chains and oxygen atoms on PMA. To study the effects of these structural and chemical properties, several model test polymers were constructed. These models may not represent feasible VII polymers, however they provide insight into the contribution of specific molecular features and chemistries on the functionality of VII polymers. For uniformity, all molecules are 50 repeat units long, placed in a dodecane solvent, and treated according to the process described in the Methods section of this Chapter.

One of the major differences between PMA and OCP is the presence of long side chains in PMA. For acrylate chemistry, long side chains improve the solubility of the polymer in the lubricating oil [1]. However, there is a possibility that these side chains also influence the overall change in polymer coil size with temperature. To understand the impact of side chain length on polymer coil size, we create a model polymethylmethacrylate (PMMA) which, as shown in Fig. 5.4(a) (molecular mass 5007.87 g/mol), has much shorter side chains than PMA. The mean and standard deviation of the radius of gyration distribution of PMMA along with the percent change in the polymer coil size are reported in Table 5.3. We observe that the mean R_g of PMMA is smaller than PMA at both temperatures, but the changes in size

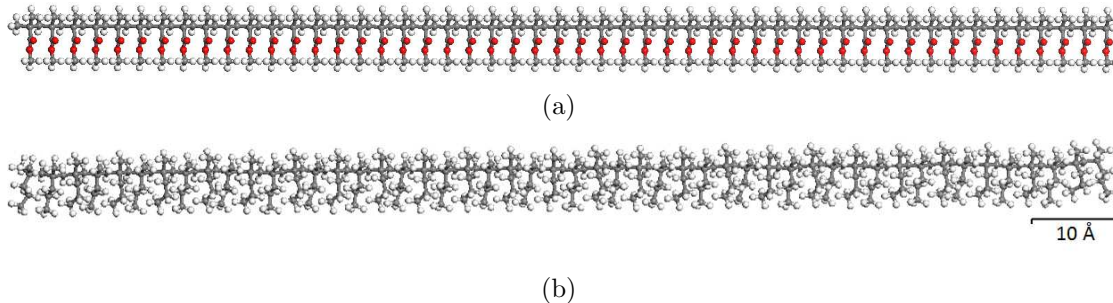


Figure 5.4: Molecular structures of (a) polymethylmethacrylate (PMMA) and (b) a test polymer that is structurally similar to PMMA but without oxygen atoms (OFP). For all figures, colored spheres represent individual atoms: grey-carbon, red-oxygen, and white-hydrogen. The scale bar applies to all figures

with temperature are comparable (31.5% for PMA and 33.4% for PMMA). This suggests that the length of the side chains affects the size, but does not affect the change in size with temperature for acrylate-based VII polymers.

Table 5.3: Mean and standard deviation of PMMA and OFP at 40°C and 100°C, along with percent change with temperature

Temperature (°C)	PMMA (Å)	OFP (Å)
40	11.2 ± 0.5	18.5 ± 1.9
100	15.0 ± 3.7	16.9 ± 2.6
Change (%)	33.4	-8.7

Another critical difference between PMA and OCP is the presence of oxygen atoms in the chemistry of the molecule, i.e. acrylate-based VII polymers contain oxygen atoms while olefin copolymers do not. We studied the influence of oxygen atoms on polymer coil size by comparing PMMA, a molecule with oxygen atoms, to a model polymer that is structurally similar to PMMA, but without oxygen atoms. The oxygen atoms in the carbonyl and ester groups in PMMA are replaced by $-\text{CH}_2-$ groups to create an oxygen free polymer (OFP), Fig. 5.4(b) (molecular mass 4210.12 g/mol). Again, the mean and standard deviation of the distribution along with the percent change in the polymer coil size are reported in Table 5.3. The mean R_g of the distribution of OFP is larger than PMMA at both temperatures. However, OFP has a negative percent change in size when temperature is increased, implying that this polymer contracts with temperature, a behavior which was observed for OCP.

This suggests that, for linear chains of similar size and structure, the presence of oxygen atoms in the molecule will significantly influence the response of the polymer coil to temperature.

The role of oxygen in altering the conformations of long-chain polymers has been an object of inquiry since at least 1974 [162], . Here, our results point to oxygen as providing a dominant factor in determining whether the polymer expands or contracts on increase in temperature. PMMA is a polymer that contains oxygen. In contrast, in OFP, the oxygens are removed and replaced by carbon atoms. The changes in length of the oxygen-free polymer, OFP, are qualitatively different from those of the oxygen-containing polymers: on heating, OFP decreases in length, while PMMA increases in length. This indicates that, for the polymers studied here, oxygen may affect a polymer's behavior through its influence on the interaction strength, described in the simulations by Lennard-Jones potential parameters, and flexibility, described in the simulations by bond angle and torsion potentials, which leads to polymer expansion on heating.

5.4 Conclusions

This chapter presents a method to estimate changes in polymer coil size of VII polymers using MD simulations. The simulations predict that PMA will increase in size with temperature while OCP will not, observations that are consistent with trends reported in the literature, which were obtained using both direct and indirect measurement methods. The hydrocarbons olefin copolymers, hydrogenated diene copolymers, and styrene butadiene copolymers do not increase in coil size on temperature rise while the polyalkylmethacrylates do. These observations are consistent with the conclusions presented here. To understand this difference, we analyzed the structural and chemical differences between OCP and PMA, and developed simulations of test polymers to isolate the effect of the differences. These simulations reveal that the presence of oxygen in PMA is critical to the observed temperature-induced increase in coil size. Overall, the molecular dynamics simulation method presented in this study holds significant promise in understanding a polymer's response to temperature change, an area that is particularly relevant for VII additives. The ability to anticipate the effect of molecular structure and chemistry on coil size may enable molecular-scale design and optimization of novel VII polymers.

Chapter 6

TRENDS IN THERMORESPONSIVE BEHAVIOR OF LIPOPHILIC POLYMERS

6.1 Introduction

Viscosity modifiers (VM) or viscosity index improvers (VII) are mainly polymers of various chemical compositions and architectures. Among the several polymeric VM previously explored, [153, 154, 163–166] two widespread examples include the following: 1) olefin copolymers (OCP) which are fully saturated, lipophilic, nonpolar, carbon based polymers that thicken oils and 2) poly(alkyl methacrylate)s (PAMA) which include fatty pendants and polar esters within the polymer chain, with lipophilic side chains but somewhat polar backbone [153, 167]. The differing chemical compositions and architectures of these VM translate into unique viscosity performance properties which have been exploited for certain lubricant applications. In particular, PAMAs tend to be better VII in part due to a lower lubricant thickening effect at lower temperatures and potentially a greater solvation difference at hot versus cold temperatures.

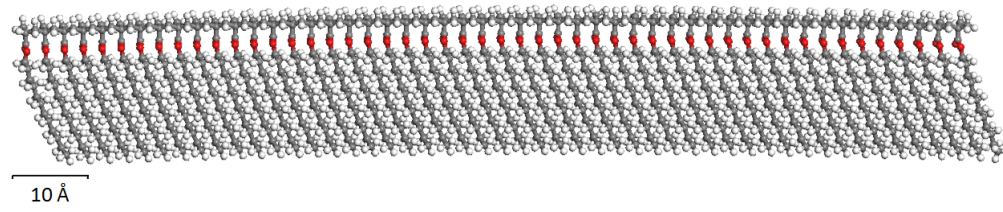
The widely accepted mechanism of VII's thermoresponsive nature revolves around the notion of polymer coil expansion at high temperatures and promotion of a globular conformation at low temperature; [24, 160] however, the mechanism of the VII's size change with temperature has only been empirically understood and directly investigated once before [160]. The intrinsic viscosity of a polymer, which relates to its radius of gyration (R_g), is temperature dependent [168–170]. Techniques to elucidate the functional mechanisms for the change in polymer size of thermoresponsive polymers have traditionally included dynamic light scattering (DLS) [171, 172] and small angle neutron scattering (SANS) [160, 173, 174]. DLS and SANS are perhaps two of the most complementary methods to measure temperature induced structural changes of polymers in solution. While DLS provides the hydrodynamic size (R_h) of the polymers in a solution, SANS gives information on the specific polymer coil transitions and is considered to be a direct measure of polymer dimensions, i.e. radius of gyration (R_g). Covitch and Trickett recently showed, using SANS measurements, that PAMA based VII undergo a transition from Gaussian coil to a coil experiencing excluded volume interactions with increasing temperatures in d-dodecane [160].

This chapter herein probes the theorized connection between VI values and molecular expansion with temperature for various polymer architectures, including linear, comb, star, and hyperbranched. We attempted to identify qualitatively, a predictive tool for VII performance of oil soluble polymers with unique architectures and chemical compositions. To this end, we explored physical techniques, SANS and DLS, and a predictive model, molecular dynamics (MD) simulation, to identify trends between dimensional changes and VII performance. Viscosity measurements for VI determination typically require multigram quantities of a given polymer which can be quite expensive to synthesize. The present methodologies only require milligram quantities (5 mg) for screening and therefore would provide a much faster result. So, in addition to challenging the conventional wisdom, finding a trend would offer a great benefit to researchers in the field of polymeric lubricant additives.

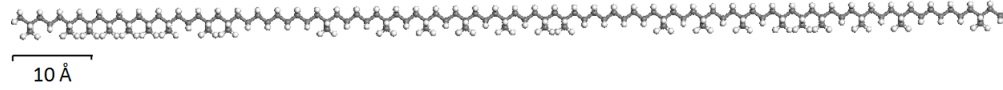
6.2 Methods

Collaborators at Pacific Northwest National Laboratory (PNNL) and NIST Center for Neutron Research (NCNR) explore the connection between VI values and temperature-induced expansion for four VII with varying architectures and chemical compositions. The four VII used are olefin copolymers (OCP), poly(alkyl methacrylate)s (PAMA), highly branched poly(ethylene) (HBPE), and star poly-(dodecyl methacrylate) (Star). HBPE [175] and Star [176] are prepared as previously described in literature, whereas OCP and PAMA are proprietary materials obtained from industrial collaborators. These polymers were separately dissolved into Yubase4 (4Y) base oil. The dynamic viscosities of these solutions were measured by a Brookfield spindle viscometer at 40 and 100 °C and divided by their densities to estimate their kinematic viscosities. VI of these solutions are then calculated using the ASTM D2270 method and reported in Table 1 of reference [177]. DLS measurements were performed in a Brookhaven ZetaPALS 90 Plus particle size analyzer at (PNNL) in Richland, Washington. SANS measurements were performed on the NG7 30 m SANS instrument at NCNR in Gaithersburg, Maryland. Detailed information on the experimental equipment, sample preparation, testing, and analysis methods can be found in reference [177].

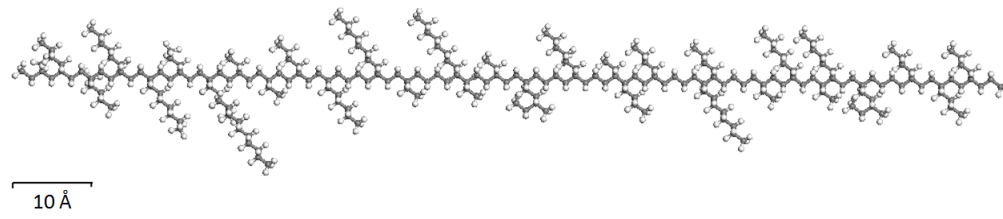
To supplement experimental findings, MD simulations of a model polymer in dodecane was used to characterize a polymer's change in size with temperature. The molecular structures of PAMA, OCP, HBPE, and Star are represented in Figure 6.1. For each polymer, a maximum of 50 repeat units was chosen as the polymer length as a compromise between computational efficiency and realism. With this length basis, the model PAMA has a molecular mass of 12722.7 g/mol, OCP has a mass of 1755.39 g/mol, and HBPE has a mass of 3831.39 g/mol. The model Star polymer has 16 repeat units in each arm (a total of 48 repeat units in all three arms) and a mass of 12584.4 g/mol.



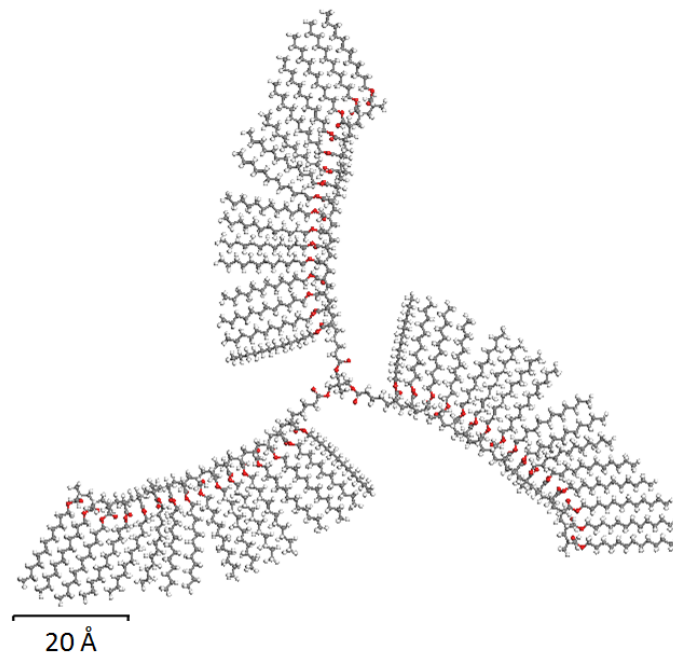
(a)



(b)



(c)



(d)

Figure 6.1: Molecular structures of (a) PAMA, (b) OCP, (c) HBPE, and (d) Star. For all structures, colored spheres represent individual atom types: grey - carbon, white - hydrogen, red - oxygen.

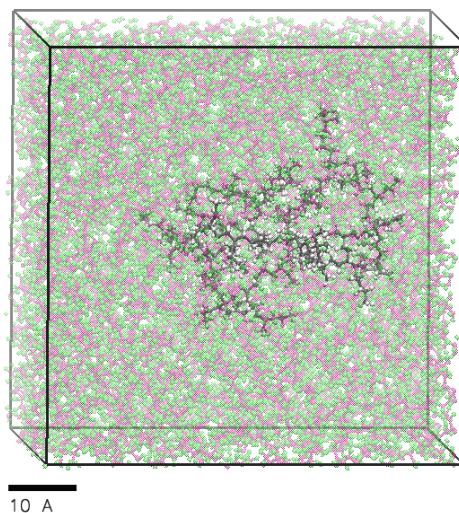
The simulation systems created had periodic boundaries in all three directions, and the size of the simulation box was either 6x6x6 nm³ (PAMA, OCP, and HBPE) or 7x7x7 nm³ (Star). As illustrated in Figure 6.2 (a) for HBPE, each respective polymer was placed in the virtual dodecane solvent. Initial simulation structures were constructed with Accelrys Materials Studio[®] and subsequent simulations performed using Large Atomic/Molecular Massively Parallel Simulation (LAMMPS) software [100]. The All Atom Optimized Potential for Liquid Simulations (OPLS-AA) force field [68] with a global cutoff of 1.2 nm was used to describe bond, angle, torsion, and nonbonded interactions between all atoms. A Noé-Hoover thermostat and barostat maintained the temperature and pressure of the system. All simulations were run with a time step of 1 fs and a 1-4 intramolecular scaling factor of 0.0. Setting the scaling factor to zero turns off the van der Waals and Coulombic interactions between 1 and 4 atom pairs, which are those separated by three bonds, and has been shown to increase the prediction accuracy of liquid-state properties for molecules with 12 carbons or more [144].

The simulations were divided into three phases: relaxation, equilibration, and production. During the relaxation stage, simulations were run at high temperatures under NVT conditions (constant number of atoms, volume, and temperature) to rapidly relax the system. The system was then equilibrated under NPT conditions (constant number of atoms, pressure, and temperature) at 40 and 100 °C, respectively, without data collection. Finally, during the production phase, the system continued to run under NPT conditions, while information on the polymers coil size was collected for analysis. Details on the simulation stages can be found in reference [178].

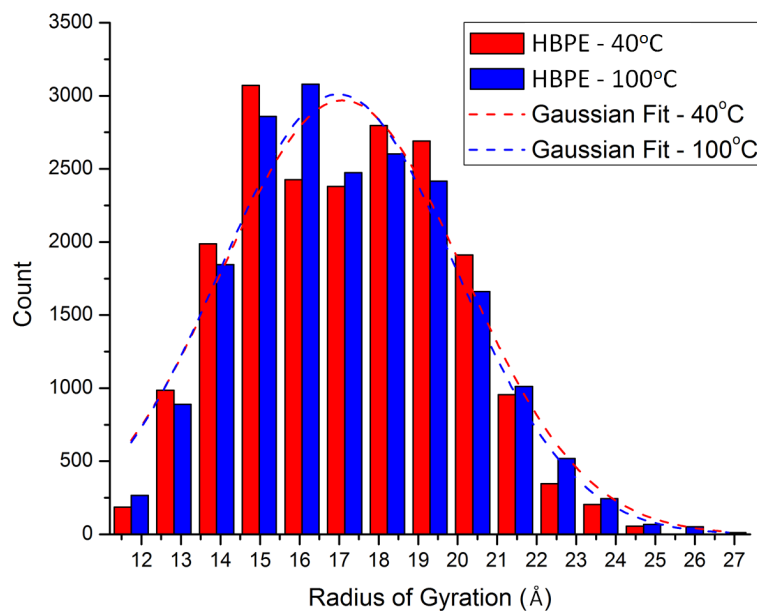
Radius of gyration, R_g , is frequently used to quantify a polymers coil size. In MD simulations, R_g is defined as the mass weighted average distance from the center of mass of the molecule to each atom in the molecule. Here, R_g was calculated at every 5 ps interval during the production stage, and the data then was used to plot frequency histograms. The frequency histograms essentially map the recurrence of specific conformations throughout the simulation time. A Gaussian function was fit to the frequency histogram to quantify the mean, μ , of the distribution. This is illustrated for HBPE in Figure 6.2 (b). Lastly, the percent change in coil size with temperature was calculated from the mean of the coil size distribution at 40 and 100 °C using $(\mu_{100^\circ C} - \mu_{40^\circ C})/\mu_{40^\circ C} * 100$.

6.3 Results

Figure 6.3 represents the variations in architecture and chemical composition portrayed by the four VII used in this work. OCPs are hydrocarbon based linear polymers that are soluble in Group III oils and nonpolar solvents. They generally have short alkyl side-chains extending from the polymer backbone. HBPEs have a similar chemical composition to OCPs but differ in architecture. HBPEs have a



(a)



(b)

Figure 6.2: (a) Initial configuration of HBPE in dodecane. The lines represent the periodic boundary. The carbon and hydrogen atoms in dodecane are represented by magenta and green spheres, respectively. The grey and white spheres represent the HBPE polymer. (b) Representative histogram of the radius of gyration of HBPE at the two temperatures, which were fit to Gaussian functions to obtain the mean of the distribution.

random branch-on-branch configuration that limits conformational mobility [175]. PAMAs are generally comb-like polymers with a relatively polar backbone (i.e., ester) and lipophilic side chains, which vary in polarity, length, and branching. Viscosity performance and therefore coil expansion with PAMAs are typically accredited to the oil immiscible repeating units which, presumably, repel hydrocarbons at low temperatures but allow diffusion at elevated temperatures. Star, like PAMAs, contains a lipophilic pendant group (i.e., C12) extending from a polar backbone but has three arms connected to a center moiety that inherently limits conformational freedom. It is important to note that all four analogs have different molecular weights and therefore unique hydrodynamic volumes. For this reason, the percent change in the dimensions was used as a measure to identify the relationship between VI performance and architecture.

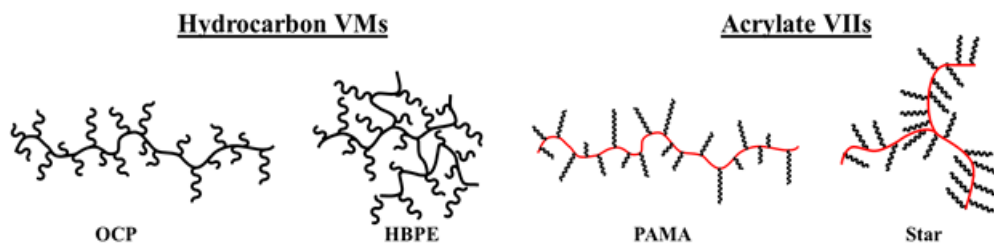


Figure 6.3: Schematic representation of the four polymers investigated, where the red line represents the polar backbone.

The hydrodynamic radii (R_h) of the polymers in hexadecane (0.5 wt % polymers in solution) were measured stepwise between 25 and 95 °C using DLS by collaborators at PNNL. Hexadecane was chosen as the solvent due to a desirable boiling point (286.8 °C) and heat capacity (499.72 JK⁻¹ mol⁻¹) as well as chemical similarity to petroleum base oils (i.e., saturated alkane). The results are shown in Figure 6.4 (a)-(d) and summarized in Table 6.1. The R_h values were mean sizes obtained by cumulant analysis. All polymers, except for OCP, had an average R_h between 10 and 35 nm at 25 °C. It is possible a few large aggregates remained in the OCP solution despite extensive filtering, resulting in one outlier point of $R_h \sim 60$ nm at 25 °C.

OCP showed a continuous decrease in R_h with temperature, with a plateau between 65 and 85 °C and an increase in R_h at 95 °C. PAMA showed a moderate decrease in size until about 75 °C and a slight increase at the highest temperature (95 °C). Like OCP, both HBPE and Star polymers show an increase in size from 65 to 95 °C. These trends can be seen clearly from the percent change in size of the polymers between 45 and 95 °C (Table 6.1). A negative percent change

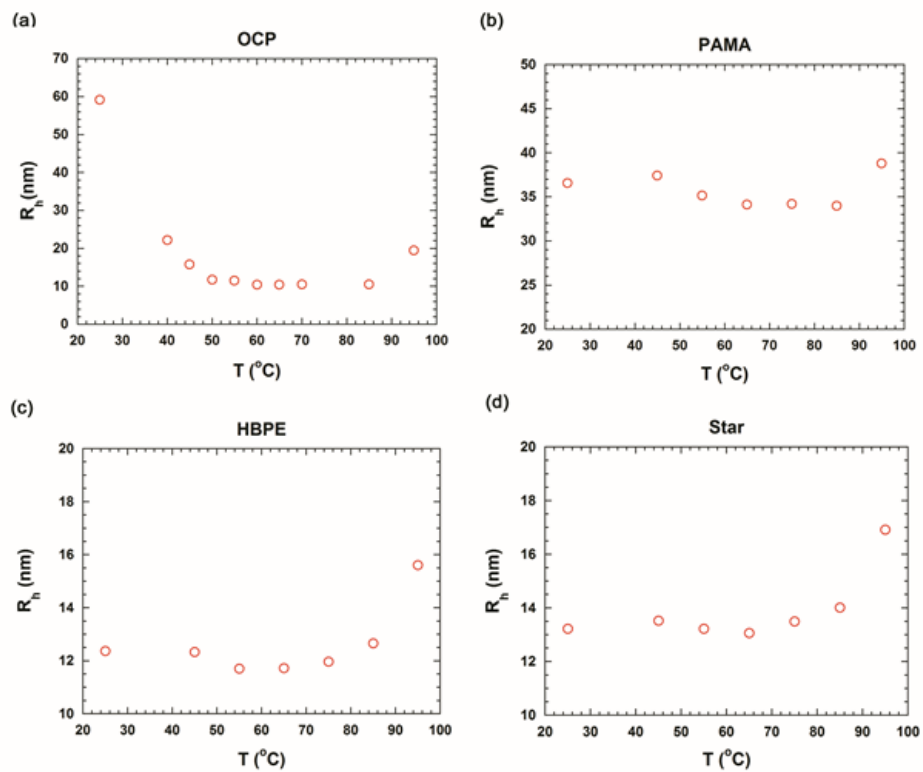


Figure 6.4: DLS plots as a function of temperature for (a) OCP, (b) PAMA, (c) HBPE, and (d) Star polymers. The scales of the y-axes have been adjusted to better visualize the changes in R_h . Error bars (standard error of the mean over 3 to 5 sample runs) are smaller than the data points and are not shown for clarity. DLS experiments and analysis were performed by P. Bhattacharya and B.J. Tarasevich from PNNL.

Table 6.1: Summary of DLS measurements for all polymers at 45 and 95 °C. Errors (standard error of the mean over 3 - 5 sample runs) in R_h are within ± 0.04 nm.

Parameters	OCP	HBPE	Star	PAMA
R_h @ 45 °C (nm)	15.82	12.33	13.53	37.44
R_h @ 95 °C (nm)	19.50	15.61	16.92	38.79
$\Delta R_h = [R_{h95} - R_{h45}]/R_{h45}(\%)$	+23.26	+26.62	+25.05	+3.61

indicates a decrease in polymer size, whereas a positive percent supports an increase in polymer size with rising temperatures. The percent increase in size of the HBPE and Star polymers are similar, although they behave somewhat differently as VII within the temperature window of study. It is notable that the chemical composition and molecular weights of PAMAs may significantly vary, depending on the source; therefore, the magnitude of the trend in polymer size may differ as well. The polymer dimensions in solution will depend on the interactions between the like and unlike components of the solvent and the polymer segments, which in turn determine whether the polymer intrasegmental interactions are more preferred over interactions with solvent molecules. Hence, a better solvent (i.e., good solvents), promotes greater swelling in the polymer. In good solvents, as temperature increases, the polymer-solvent interaction increases while the polymer-polymer (intra- and intermolecular) interaction decreases thereby resulting in coil expansion [168]. When the concentration of the polymer solution is infinitely dilute, intermolecular polymer-polymer interactions are negligible. Therefore, any change in the intrinsic viscosity of the solution at such low concentrations may be attributed to the polymer-solvent interaction. An independence of the polymer size on temperature may indicate that either the solvent behaves as a good solvent throughout the temperature range in this study or that the polymer coil does not expand while increasing temperature. A decrease in polymer size, however, indicates polymer coil contraction and suggests the polymer-solvent interaction is less favorable at elevated temperatures. The temperature range of these experiments may not be all inclusive toward studying polymer coil expansion or the more elusive globule-to-coil polymer transition state but does provide a qualitative understanding of the relationship between changes in polymer size and VI behavior. Overall, there appears to be no correlation between ΔR_h and VI values based on DLS measurements.

While DLS provides information on the global topology of the polymers and their solvent interactions, SANS provides a direct measure of polymer dimensions and internal structure. SANS experiments were conducted by collaborators at NCRC, where polymer samples were dissolved in d-hexadecane at 0.5 wt % at 25,

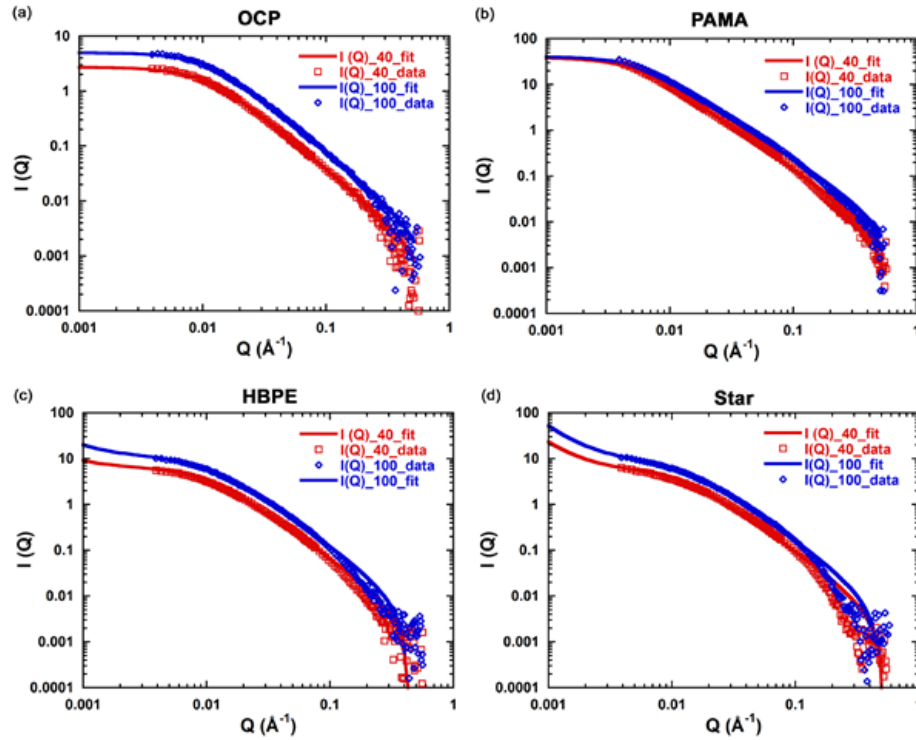


Figure 6.5: SANS profiles of (a) OCP, (b) PAMA, (c) HBPE, and (d) Star polymers in d-hexadecane. Solid red and blue lines show model fits to the SANS data. The data for OCP and PAMA polymers have been fitted to the polymer excluded volume model, whereas data for HBPE and Star polymers have been fitted to the correlation length model. The $I(Q)$ values at 100 °C data and their corresponding fits in each plot have been multiplied by 2 for clarity. Error bars (standard error of the mean for the number of detector pixels used in the data averaging) at low Q are smaller than the data points, and error bars at high Q are not shown for clarity. SANS experiments and analysis were performed by S. Krueger from NCNR.

40, 70, and 100 °C. Figure 6.5 shows the SANS profiles for the four polymer solutions measured at 40 and 100 °C. Details on the SANS data analysis technique can be found in reference [177]. From SANS measurements, OCP and PAMA polymers fit well to the polymer excluded volume interactions model with Porod exponents (n) close to 5/3. This indicates the polymer coils are swollen and in good solvent conditions. However, both HBPE and Star polymers have Porod exponents closer to 2, validating their compact conformation by design and indicating Gaussian chain structures. Furthermore, they did not fit well with the polymer excluded volume interactions model nor the Gaussian coil or Debye models. Hence, an empirical model with Porod and Lorentzian-like terms was used, to get the correlation lengths (L_c) and Porod exponents to fit the scattering curves for these polymers. The comparisons between the polymer excluded volume interactions model and the correlation length model fits are shown in the Supporting Information (Figure S3) of reference [177] for HBPE and the Star polymers. Using the correlation length model, no reduction in n or change in R_g with increasing temperature was observed for the Star and HBPE polymers, implying that their internal flexibility is low. Even though HBPE and Star polymers fit poorly to the polymer excluded volume model, the Porod values computed were similar to those from the correlation length model, and R_g showed the same trends as the correlation length (Table S1 in reference [177]). On the other hand, a very minor reduction in n from 1.87 (40 °C) to 1.78 (100 °C) was observed for PAMA suggesting a coil experiencing excluded volume interactions with increasing temperature. This change is also accompanied by a slight decrease in R_g . The results of the fits are shown in Table 6.2.

The R_g and L_c values determined by SANS are smaller than the R_h values determined by DLS. The DLS method probes the diffusion behavior of the polymer, while the SANS method detects inhomogeneities in the neutron density of a sample. The hydrodynamic radius determined by DLS will include associated solvent that is not visible to SANS. The SANS method, therefore, will tend to measure the polymer size and will show a significant change in polymer dimensions only if there is a structural change in the polymer with changing temperature, while DLS measures the size of the polymer plus associated solvent [179].

The third method used to characterize polymer change in size with temperature was MD simulations of each model polymer in dodecane. The evolution of the polymers coil size, determined by the radius of gyration, R_g , was observed throughout the simulation duration. Table 6.3 summarizes mean R_g values calculated from MD simulations at 40 and 100 °C and the percent change in coil size with temperature for all four molecules described above. A positive percent change indicates coil size expansion, while a negative percent change implies coil size contraction with temperature. From Table 6.3 we observe that PAMA is the only molecule that is predicted to expand significantly with

Table 6.2: Summary of SANS results for all polymers at 40 and 100 °C. Errors in R_g , L_c , and the Porod exponent are the statistical errors determined from the fits to the data.

Sample	Model Fit	T (°C)	Porod Exponent, n	R_g (nm)	ΔR_g [$R_{g100} - R_{g40}$]/ R_{g40} (%)
OCP	polymer excluded volume	40	1.85 ± 0.01	13.6 ± 0.1	-4.4 ± 1.0
		100	1.85 ± 0.01	13.0 ± 0.1	
PAMA	polymer excluded volume	40	1.87 ± 0.01	27.8 ± 0.1	-12.6 ± 1.8
		100	1.78 ± 0.01	24.3 ± 0.1	

Sample	Model Fit	T (°C)	Porod Exponent, n	L_c (nm)	ΔL_c [$L_{c100} - L_{c40}$]/ L_{c40} (%)
HBPE	correlation length	40	1.90 ± 0.01	10.4 ± 0.1	$+0.95 \pm 1.4$
		100	1.90 ± 0.01	10.5 ± 0.1	
Star	correlation length	40	2.10 ± 0.01	8.2 ± 0.1	-2.43 ± 3.2
		100	2.10 ± 0.01	8.0 ± 0.1	

temperature. OCP, HBPE, and Star, on the other hand, exhibit similar mean R_g values at both temperatures, suggesting that these polymers undergo negligible changes in coil size with temperature.

6.4 Discussion

A summary of the results from DLS, SANS, and MD is shown in Figure 6.6. By comparing the simulation calculations to the SANS experimental measurements, an opposite trend is observed, with the exception of PAMA, where a decrease in size was observed in SANS measurements. However, through DLS measurements, a significant increase in size with temperature is observed for OCP, HBPE, and Star polymers while a modest increase in size is observed for PAMA. Simulations entirely disagree with DLS, where a significant decrease in size with temperature is observed for all analogs, except for PAMA. However, considering that PAMA has the highest VI, followed by the Star, HBPE, and OCP, simulations do realistically predict PAMAs behavior.

DLS data shows that OCP, HBPE, and Star clearly expand with temperature, while SANS shows the opposite effect. Since DLS can detect the solvent shell associated with the polymer, while SANS cannot, changes in R_h measured by DLS, therefore, may correspond to changes in solvent interactions, while changes in R_g measured by SANS may correspond to change in the polymer

Table 6.3: Mean values of the R_g distribution for all polymers at 40 and 100°C along with the percent change in coil size with temperature ^a

Temperature (°C)	OCP [178] (nm)	HBPE (nm)	Star (nm)	PAMA [178] (nm)
40	1.65	1.72	2.15	1.71
100	1.61	1.73	2.10	2.25
Change (%)	-2.4	0.18	-2.3	31.5

^a Data for PAMA and OCP are from reference [178]

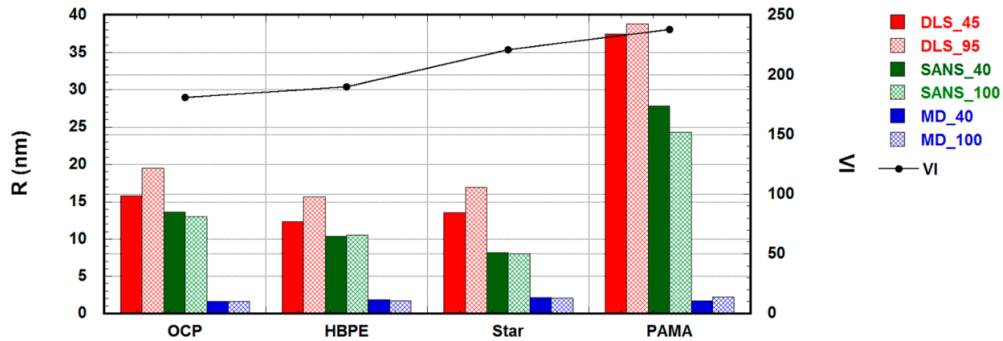


Figure 6.6: Comparison between DLS, SANS, and MD simulations results of polymers, along with the VI values. Here R represents R_h values from DLS, R_g values from MD simulations, R_g values for OCP and PAMA, and L_c values for HBPE and Star polymers from SANS measurements. DLS experiments and analysis were performed by P. Bhattacharya and B.J. Tarasevich (PNNL) while SANS experiments were performed by S. Krueger (NCNR).

structure itself. The increase in R_h with temperature, therefore, may correspond to an increase in solvent-polymer chain interactions. An increase in solvation is also suggested by a leveling off of the scattering intensity with temperature in the DLS measurements (Figure S4 in [177]). Scattering intensity typically increases with R_h unless there is a change in the refractive index of the polymer. The leveling off of scattering intensity corresponding to an increase in R_h , shown in Figure S4 of reference [177], suggests a decrease in the refractive index of the polymer due to solvent swelling [180]. However, PAMA and Star have similar polarities and backbones, and the dissimilar behavior is surprising. One would expect that polymers with higher polarity than the solvent (baseoil, in this case hexadecane) will respond in an equivalent manner to heat and have similar VIs. The VI values of the PAMA and Star are in the ballpark, but the observed DLS and SANS

behaviors are not.

It is important to note that a Porod exponent of 3 was not observed, characteristic of a collapsed polymer coil, for any polymer at all temperature conditions studied. The temperature dependent viscosity measurements suggest that there is a significant improvement in the VI of 4Y oil, from 127, on adding all the above polymers as VII (Table 1 in reference [177]). Interestingly, the PAMA polymer shows the greatest improvement in VI (238) despite showing a modest increase in R_h with temperature through DLS measurements and a decrease in R_g with temperature through SANS measurements. On the other hand, the HBPE and OCP polymers underwent a similar increase in R_h with increasing temperature and demonstrated comparable VI performance (OCP 181, HBPE 190), even though a decrease in size with increasing temperature in SANS measurements was observed for OCP. Moreover, the Star polymer which showed a large increase in size through DLS but negligible change in size in SANS measurements had a VI of 221 slightly lower than that of the PAMA polymer, 238. These conflicting dimensional-performance behaviors can be observed clearly in Figure 6.6. Overall, the physical data obtained from DLS and SANS when qualitatively compared to empirically calculated VI values suggests that the current polymer globule-to-coil transition or coil expansion VI structure-performance relationship explanation is not all-telling, at least between 40 and 100 °C.

If polymer size changes do not correlate with VIs, other factors must be important in controlling the VIs of polymeric additives. Molecular weight correlates well with thickening efficiency and generally with VIs, but this discussion is outside the scope of this study. HBPE and Star were prepared and analyzed by collaborators at PNNL; however, OCP and PAMA were acquired through industrial partnerships, and their respective molecular weights are proprietary information. As described earlier, the VII investigated in this study have unique chemical compositions and architectures compared to one another. In particular, OCP and HBPE have different topologies but are roughly the same chemically, which translates to comparable KVs and subsequent VIs. The Star and PAMA additives have the highest VIs even though their architectures are very different from one another. Both of these additives have similar chemical compositions involving a polar ester backbone with lipophilic alkyl side chains. The polar backbone appears to have a role in increasing the VI by affecting polymer stiffness or solvent interactions.

6.5 Conclusion

A comparison of results from two experimental techniques and MD simulations shows that, while these techniques are excellent probes for polymer-solvent interactions, polymer size, and structure, they might not be able to predict the behavior of the polymers as VII in oil. The interactions of VII with oil include a complex mix of inter- and intramolecular interactions such as polar/nonpolar

interactions that are long range and not accounted for by the above techniques. The molecular weight, architecture, and chemical composition of the polymers have a huge influence on the solution viscosity and thermoresponsiveness [181,182]. Moreover, the topology and architecture of the VII have non-uniformities in them. In this chapter we observed that polymers which significantly improve the VI (PAMA) do not show considerable change in size in the observation window between 40 and 100 °C. In conclusion, changes in polymer size do not significantly affect VI values as described by the traditional model suggesting that other factors are important in controlling and optimizing VI.

Chapter 7

SUMMARY AND FUTURE WORK

7.1 Summary

In summary, molecular dynamics simulation was used to study the surface and bulk properties of liquid lubricants. Part I of this thesis was dedicated to understanding properties and features of lubricated surfaces. We explored topics such as surface coverage and stability of thin functionalized polymer films as well as mechano- and tribo-chemical processes occurring at boundary lubricated sliding interfaces. In Part II of this thesis, we studied bulk fluid properties of lubricants, specifically the pressure-viscosity and temperature-viscosity response of lubricants. A novel method for predicting the pressure-viscosity response of a fluid was developed using an empirical equation and MD predicted material properties. Polymers used to improve the temperature-viscosity response of lubricants were also investigated in order to understand the mechanisms behind their functionality. Specifically, we were interested in their coil expansion mechanism, which we studied using several analytical techniques. In general, this work provides an in-depth analysis of several key features and properties that govern the functionality of surface and bulk lubricants. A clear understanding of functionality can lead to better lubricating capabilities through the design of more energy-efficient lubricants.

7.2 Future Work

7.2.1 Exploring Lubricant-Surface Interactions Under Shear

In Chapter 2, we studied the effectiveness of a non-covalently adsorbed polymer layer by characterizing conformation and stability of thin PFPE films. This analysis was conducted using coarse-grained PFPE molecules and performed under zero shear. In high shear applications with boundary lubricated films, such as hard disk drives, the stress can cause the lubricant coating to shear off of the substrate [29]. To avoid spin off, functionalized polymers typically have dynamic bonding and self-healing capabilities that are especially important in high shear boundary lubricated applications [78].

The work in Chapter 2 can be expanded to study the effects of shear forces using a more detailed fully atomistic model. In this model, a shear force would be induced on the bottom substrate and the density, distribution, and stability of the remaining adsorbed film could be characterized. This approach would make the research both novel, comparable to real systems, and provide a platform to study behaviors of commonly-used functionalized polymers under realistic operating conditions. In general, this follow-up would provide insight into lubricant-substrate interactions under shear.

7.2.2 Exploring Mechanochemical Reactions Using Reactive Force Fields

Chapter 3 of this thesis studied the shear-induced mechanochemistry experienced by a methyl thiolate covered copper surfaces. Sliding experiments conducted under UHV, performed by collaborators at University of Wisconsin-Milwaukee, showed that methyl thiolate molecules decomposes thermally to evolve predominantly into methane. Experimental results were supplemented with MD simulations to analyze and characterize the force distribution on the methyl thiolate molecules during sliding. Some methyl thiolate molecules experienced larger sliding forces, present at the tail of the distribution, that were significant enough to initiate mechanochemical reactions that resulted in the formation of methane molecules.

The MD study discussed in Chapter 3 was conducted using the Polymer Consistent Force Field (PCFF), a non-reactive force field that does not capture bond breakage or formation. This study can be followed up by conducting simulations using a reactive force field, such as Reax-FF, which is a bond order based force field capable of modeling chemical reactions [183]. Simulations performed using Reax-FF would provide a more realistic model of surface tribochemistry. This method would allow us to physically observe and quantify mechanochemical reactions occurring at the sliding interface to further support experimental observations of methane formation. Additionally, this approach would enable an in-depth analysis to be conducted on the chemical reactions experienced by the methyl thiolate molecules that lead to the formation of methane.

7.2.3 Correlating Molecular Features to Coil Expansion and Viscosity

Chapter 5 explored the temperature-induced expansion of polyalkylmethacrylates and olefin copolymers, two commonly used viscosity index improver and viscosity modifier. We presented a methodology that estimates changes in coil size of VII polymers using MD simulations. MD results showed that polyalkylmethacrylates expanded with temperature while olefin copolymers did not, consistent with trends reported in literature [24, 159–161]. Additional analysis on polyalkylmethacrylate and olefin copolymer chemistry using model polymers showed that the presence of oxygen atoms in the polymer structure is a key factor that determines whether the polymer expands or contracts with temperature [178].

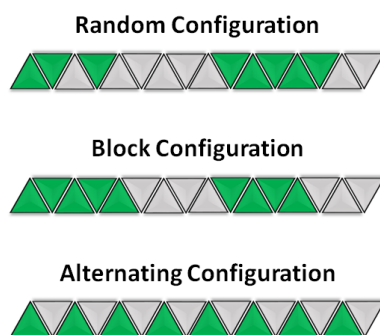


Figure 7.1: Schematic representation of potential copolymer configurations. The green and grey triangles represent different monomer species.

Our research showed that simulations are able to accurately capture the role of chemical structure on changes in molecular size with temperature. This research can be followed up with viscosity simulations, where we can work towards correlating structural features to coil size expansion and viscosity. Over the years, advancements in VII technology have been focused on either modifying chemistries [150–152] or manipulating the structure and architecture [153–155] of traditional VII polymers. These experimental works can be supplemented and accelerated by using MD simulations to correlate structural features, such as chemistry and architecture, to VII functionality. For example, configurations of styrene-butadiene polymer, another type of VII polymer, can be examined to correlate variations in block, random, or alternating configurations to coil expansion and viscous properties. A schematic of potential styrene-butadiene configurations is illustrated in Figure 7.1. The proposed method is unique because it enables a systematic analysis to be conducted on real or fictitious molecules to understand how key molecular features drive product functionality. A fundamental

grasp of the structure-property-function relationships will aid in the design of application-specific VII polymers with enhanced performance and functionality.

7.2.4 Exploring Alternative Mechanisms That Influence VII Functionality

In 1958, Selby first introduced the concept of coil expansion to explain the mechanism behind the functionality of VII additives [48]. This theory proposes that, as temperature is increased, the solubility of the polymer in the lubricating oil improves and the polymer expands, thus inducing a thickening effect which modifies the overall solution rheology. Recent studies using MD simulations, as discussed in Chapters 5 and 6, experiments, and empirical models revealed that this mechanism is not observed by all viscosity modifying polymers [24, 159–161, 178]. Specifically, hydrocarbon chemistries, such as olefin copolymer and hyperbranched polyethylene, show minimum changes in coil size with temperature, but are still able to induce a thickening effect in the solution. This suggests that there is more than one mechanism involved in how VII polymers affect rheology.

The coil size analysis conducted on hydrocarbon chemistries can be followed up by studying alternative factors that modify solution rheology, such as solubility, aggregation or association of the polymer, entanglement, polymer-solvent interactions, and solvent structure. Some of these concepts have been studied extensively using MD simulation, for example, solubility can be studied using Hildebrand or Hansen solubility parameters [184] and entanglement can be studied using the Rouse or tube model [98, 134, 185–187]. Other properties, such as association and polymer-solvent interactions, may be investigated using analytical tools that estimate the number of contact atoms between two associating molecules. This study can provide a detailed investigation of all the mechanisms and factors that contribute to rheology improvements observed in polymer-enhanced solutions. A clear understanding on the factors that influence the functionality of VII polymers will be beneficial in designing better lubricant packages.

7.2.5 Exploring Competition Between Boundary Lubricated Additives

In boundary lubrication, antiwear additives and friction modifiers are added to reduce friction and wear of the sliding contacts. Commonly used antiwear additives are zinc dithiophosphates, tricresyl phosphates, and their derivatives that are modified for different temperatures and stability [20, 60–62]. Friction modifiers, on the other hand, are chemicals consisting of polar heads and long non-polar chains that stack vertically to separate the contacting metal surfaces [20, 58]. Both antiwear and friction modifiers function by either adsorbing on or reacting with the metal surface to form a protective film. Since both these additives function by

interacting with the substrate to form a protective layer, these additives will compete amongst one another to adsorb onto the contact surface [56]. For maximum functionality, a good balance has to be maintained between the composition of antiwear additives and friction modifiers.

Future studies on boundary lubricated films can be focused on characterizing several different types of antiwear additives and friction modifiers to understand how these additives function under different conditions. A fully atomistic model using reactive force fields can be used to simulate and study the adsorption and desorption process of the respective additives. The stability of the resulting boundary film can be characterized under varying temperatures, pressures, and sliding speeds. Models with mixtures of antiwear additives and friction modifiers of varying concentrations, as illustrated in Figure 7.2, can also be studied at the molecular level to understand the dynamics of how these two additives compete for adsorption surfaces. This study would facilitate a complete understanding of the individual properties of antiwear additives and friction modifiers under different operating conditions as well as the nature of the competition between two additives. A clear understanding of the competition between these two commonly used surface active additives will ultimately enable the formulation of additive packages with optimum functionality and efficiency.

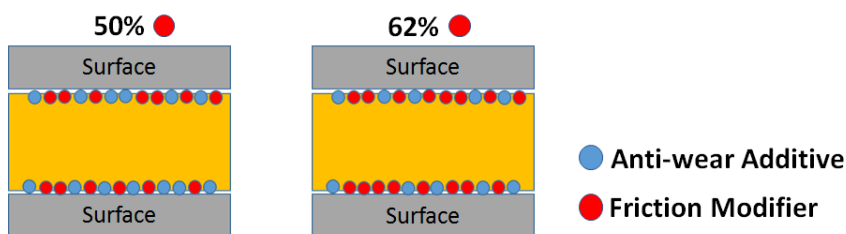


Figure 7.2: Schematic representation of a mixture of friction modifiers and antiwear additives at two different concentrations. The red spheres represent friction modifiers and the blue spheres represent antiwear additives.

7.3 Concluding Remarks

Molecular dynamics simulations was used to study the surface and bulk properties of liquid lubricants. A variety of bulk fluid and boundary lubricated systems were modeled to understand features, properties, and mechanisms that are specific to those systems. This thesis covers topics such as surface coverage and stability of thin films, tribochemical processes occurring at boundary lubricated sliding interfaces, a novel method for predicting the pressure-viscosity response of a fluid, and the coil expansion mechanism of viscosity improving additives. The work completed here can be followed-up with additional studies that complement or improve the content of this thesis. Future work can be conducted to explore lubricant-substrate interactions under shear, mechanochemical reactions using reactive force fields, alternative mechanisms that influence VII functionality, competition between boundary lubricated additives, and the correlation between molecular features, coil expansion, and viscosity. Advancements in all of these areas can lead to the design of lubricants and lubricated systems with enhanced performance, which in return will increase energy efficiency and reduce energy consumption.

BIBLIOGRAPHY

- [1] S.Q.A. Rizvi. *A Comprehensive Review of Lubricant Chemistry, Technology, Selection, and Design*. ASTM International, Conshohocken, 2009.
- [2] C.M. Mate. Taking a fresh look at disjoining pressure of lubricants at slider-disk interfaces. *IEEE Trans. Magn.*, 47(1):124–130, 2011.
- [3] H.L. Adams, M.T. Garvey, U.S. Ramasamy, Z. Ye, A. Martini, and W.T. Tysoe. Shear induced mechanochemistry: Pushing molecules around. *J. Phys. Chem. C*, 119(13):7115–7123, 2015.
- [4] ASME. Pressure-viscosity report. Technical report, American Society of Mechanical Engineers, New York, 1953.
- [5] R.M. Mortier, S.T. Orszulik, and M.F. Fox. *Chemistry and Technology of Lubricants, Third Edition*. Springer, London, 2010.
- [6] S. Bair. A characterization of the pressure-viscosity behavior of two gear oils and one tractor oil to 1.2 gpa. Georgia Institute of Technology. Report to John Deere Product Engineering Center, 2013.
- [7] S. Bair. A characterization of the compressibility of two gear oils. Georgia Institute of Technology. Report to John Deere Product Engineering Center, 2013.
- [8] G.W. Stachowiak and A.W. Batchelor. *Engineering Tribology, Third Edition*. Butterworth-Heinemann, Burlington, 2006.
- [9] P. Jost. Lubrication (Tribology) - A report on the present position and industrys needs. Technical report, Department of Education and Science, UK, 1966.
- [10] International energy outlook 2011. Technical report, US Energy Information Administration, 2011.
- [11] Lawrence Livermore National Laboratory. Energy flowchart, 2012.
- [12] K. Holmberg, P. Andersson, and A. Erdemir. Global energy consumption due to friction in passenger cars. *Tribol. Inter.*, 47:221–234, 2012.

- [13] H.P. Jost. Tribology micro macro economics: A road to economic savings. *Tribol. Lubr. Technol.*, 61:18–22, 2005.
- [14] M.R. Hilton and P.D. Fleischauer. Applications of solid lubricant films in spacecraft. *Surf. Coat. Technol.*, 54:453–441, 1992.
- [15] S.Q.A. Rizvi. *Additives: Chemistry and Testing, Tribology Data Handbook An Excellent Friction, Lubrication, and Wear Resource*. CRC Press, Boca Raton, 1997.
- [16] S. Bair. *High Pressure Rheology for Quantitative Elastohydrodynamics*. Elsevier, Oxford, 2007.
- [17] V. Ganesan. *Internal Combustion Engines*. McGraw Hill Education (India) Pvt Ltd, India, 2012.
- [18] C.A. Bouman. *Properties of Lubricating Oils and Engine Deposits*. McMillan and Co., London, 1950.
- [19] T. Regueira, L. Lugo, O. Fandiño, E.R. López, and J. Fernández. Compressibilities and viscosities of reference and vegetable oils for their use as hydraulic fluids and lubricants. *Green Chemistry*, 13(5):1293–1302, 2011.
- [20] B. Bushan, editor. *Modern Tribology Handbook, Volume One*. CRC Press, Boca Raton, 2001.
- [21] L.D. Wedeven. What is ehd? *Journal of the American Society of Lubrication Engineers*, 31:291–296, 1975.
- [22] D. Dawson and G.R. Higginson, editors. *Elasto-hydrodynamic Lubrication: The Fundamentals of Roller and Gear Lubrication*. Pergamon Press, England, 1966.
- [23] G.E. Totten, S.R. Westbrook, and R.J. Shah. *Fuels and lubricants handbook: technology, properties, performance, and testing*. American Society for Testing & Materials, 2003.
- [24] C. Mary, D. Phillipon, L. Lafarge, D. Laurent, F. Rondelez, S. Bair, and P. Vergne. New insight into the relationship between molecular effects and the rheological behavior of polymer-thickened lubricants under high pressure. *Tribol. Lett.*, 52(3):357–369, 2013.
- [25] R. Larsson, E. Kassfeldt, Å. Byheden, and T. Norrby. Base fluid parameters for elastohydrodynamic lubrication and friction calculations and their influence on lubrication capability. *J. Synth. Lubr.*, 18(3):183–198, 2001.

- [26] A.S. Pensado, M.J.P. Comunas, and J. Fernandez. The pressure-viscosity coefficients of several ionic liquids. *Tribol. Lett.*, 31(2):107–118, 2008.
- [27] J. Zakarian. The limitations of the viscosity index and proposals for other methods to rate viscosity-temperature behavior of lubricating oils. *SAE Int. J. Fuels Lubr.*, 5(2012-01-1671):1123–1131, 2012.
- [28] E.C. Fitch. *Proactive Maintenance for Mechanical Systems*. Elsevier Science, England, 1992.
- [29] B. Marchon. *Developments in Data Storage: Materials Perspective, First Edition*. John Wiley and Sons, Inc., 2012.
- [30] X.C. Guo, B. Marchon, R.H. Wang, C.M. Mate, Q. Dai, R.J. Waltman, H. Deng, D. Pocker, Q.F. Xiao, Y. Saito, and T. Ohtani. A multidentate lubricant for use in hard disk drives at sub-nanometer thickness. *J. Appl. Phys.*, 111(2):024503, 2012.
- [31] R. Waltman. The adsorbed film structure of end-functionalized poly (perfluoro-*n*-propylene oxide). *Tribology Online*, 9(3):113–120, 2014.
- [32] H. Chen, Q. Guo, and M.S. Jhon. Effects of molecular structure on the conformation and dynamics of perfluoropolyether nanofilms. *IEEE Trans. Magn.*, 43(6):2247–2249, 2007.
- [33] P.S. Chung, M.S. Jhon, and H.J. Choi. Molecularly thin fluoro-polymeric nanolubricant films: tribology, rheology, morphology, and applications. *Soft Matter*, 12(11):2816–2825, 2016.
- [34] T.R. Lynch. *Process Chemistry of Lubricant Base Stocks*. CRC Press, Boca Raton, 2007.
- [35] F.M. Seger, H.G. Doherty, and A.N. Sachanen. Noncatalytic polymerization of olefins to lubricating oils. *Ind. Eng. Chem.*, 42(12):2446–2452, 1950.
- [36] G.M. van der Want, K.I. Beynon, T.G. Evans, C.B. Milne, and D. Southern. Polymerisation of dec-1-ene. I. Effect of change of reaction conditions. *J. Appl. Chem.*, 12(1):33–45, 1962.
- [37] K.I. Beynon, C.B. Milne, and D. Southern. Polymerisation of dec-1-ene. II. Effect of reaction temperature. *J. Appl. Chem.*, 17(8):213–217, 1967.
- [38] D.H. Antonsen, P.S. Hoffman, and R.S. Stearns. Preparation and properties of oligomers from 1-octene. *Ind. Eng. Chem. Prod. Res. Dev.*, 2(3):224–228, 1963.

- [39] A.G. Evans, D. Holden, P.H. Plesch, M. Polanyi, and W.A. Weinberger. Friedel-crafts catalysts and polymerization. *Nature*, 157:102, 1946.
- [40] A.G. Evans and M. Polanyi. Polymerization of isobutene by friedel-crafts catalysts. *J. Chem. Soc.*, pages 252–306, 1947.
- [41] T. Higashimura, Y. Miyoshi, and H. Hasegawa. Cationic oligomerization of 1-hexene catalyzed by EtAlCl₂chloroacetic acid complexes. *J. Appl. Pol. Sci.*, 27(7):2593–2603, 1982.
- [42] A. Pettersson. High-performance base fluids for environmentally adapted lubricants. *Tribol. Int.*, 40(4):638–645, 2007.
- [43] S. Boyde. Hydrolytic stability of synthetic ester lubricants. *Lubr. Sci.*, 16(4):297–312, 2000.
- [44] V. Eychenne and Z. Mouloungui. Relationships between structure and lubricating properties of neopentylpolyol esters. *Ind. Eng. Chem. Res.*, 37(12):4835–4843, 1998.
- [45] Neil Canter. Viscosity index improvers. *Tribol. Lubr. Technol.*, 67(9):10–22, 2011.
- [46] R.J.A. Eckert and D.F. Covey. Developments in the field of hydrogenated diene copolymers as viscosity index improvers. *Lubr. Sci.*, 1(1):65–80, 1988.
- [47] A.M. Nassar, N.S. Ahmed, R.S. Kamal, A.A.A. Abdel Azim, and E.I. El-Nagdy. Preparation and evaluation of acrylate polymers as viscosity index improvers for lube oil. *Pet. Sci. Technol.*, 23(5–6):537–546, 2005.
- [48] T.W. Selby. The non-newtonian characteristics of lubricating oils. *ASLE Trans.*, 1(1):68–81, 1958.
- [49] A.A.A. Abdel Azim, A.M. Nasser, N.S. Ahmed, A.F. El Kafrawy, and R.S. Kamal. Multifunctional additives viscosity index improvers, pour point depressants and dispersants for lube oil. *Pet. Sci. Technol.*, 27(1):20–32, 2009.
- [50] X. Maleville, D. Faure, A. Legros, and J.C. Hipeaux. Oxidation of mineral base oils of petroleum origin: The relationship between chemical composition, thickening, and composition of degradation products. *Lubr. Sci.*, 9(1):1–60, 1996.
- [51] Neil Canter. Antioxidants: Key additives enable lubricants to operate under more severe conditions. *Tribol. Lubr. Technol.*, 72(9):10–21, 2016.

- [52] S. George, S. Balla, V. Gautam, and M. Gautam. Effect of diesel soot on lubricant oil viscosity. *Tribol. Inter.*, 40(5):809–818, 2007.
- [53] T. Mang and W.S Dresel, editors. *Lubricants and Lubrication, Second, Completely Revised and Extended Edition*. John Wiley & Sons, 2007.
- [54] A. Dorinson and K.C. Ludema. *Mechanics and Chemistry in Lubrication. Tribology Series, Vol. 9*. Elsevier, Amsterdam, 1985.
- [55] Z. Pawlak. *Tribochemistry of Lubricating Oils. Tribology and Interface Engineering Series, Vol. 45*. Elsevier, Amsterdam, 2003.
- [56] R. Sarin, D.K. Tuli, A.S. Verma, M.M. Rai, and A.K. Bhatnagar. Additive-additive interactions: search for synergistic FM-EP-AW composition. *Wear*, 174(1–2):93–102, 1994.
- [57] H. Spikes. Friction modifier additives. *Tribol. Lett.*, 60(5):1–26, 2015.
- [58] Z. Tang and S. Li. A review of recent developments of friction modifiers for liquid lubricants (2007-present). *Current Opinion in Solid State and Materials Science*, 18(3):119–139, 2014.
- [59] N.J. Mosey, M.H. Müser, and T.K. Woo. Molecular mechanisms for the functionality of lubricant additives. *Science*, 307(5715):1612–1615, 2005.
- [60] F. Rounds. Contribution of phosphorus to the antiwear performance of zinc dialkyldithiophosphates. *ASLE Trans.*, 28(4):475–485, 1985.
- [61] E.S. Forbes. Antiwear and extreme pressure additives for lubricants. *Tribology*, 3(3):145–152, 1970.
- [62] A.G. Papay. Antiwear and extreme pressure additives in lubricants. *Lubr. Sci.*, 10(3):209–224, 1998.
- [63] V.S. Saji. A review on recent patents in corrosion inhibitors. *Recent Patents on Corrosion Science*, 2(6):6–12, 2010.
- [64] R. Larson. The performance of zinc dithiophosphates as lubricating oil additives. *Ind. Lubr. Tribol.*, 10(8):12–19, 1958.
- [65] P.C. Hamblin, U. Kristen, and D. Chasan. Ashless antioxidants, copper deactivators and corrosion inhibitors: their use in lubricating oils. *Lubr. Sci.*, 2(4):287–318, 1990.

- [66] W.F. van Gunsteren and H.J.C. Berendsen. Computer simulation of molecular dynamics: Methodology, applications, and perspectives in chemistry. *Angew. Chem. Int. Ed. Engl.*, 29(9):992–1023, 1990.
- [67] *InsightII User Guide*. Molecular Simulations Inc., 1996.
- [68] W.L. Jorgensen, D.S. Maxwell, and J. Tirado-Rives. Development and testing of the opls all-atom force field on conformational energetics and properties of organic liquids. *J. Am. Chem. Soc.*, 118(45):11225–11236, 1996.
- [69] D.J. Evans and G.P. Morriss. *Statistical Mechanics of Nonequilibrium Liquids*. Academic Press, London, 1990.
- [70] M.P. Allen and D.J. Tildesley. *Computer Simulation of Liquids*. Clarendon Press, Oxford, 1991.
- [71] B. Bhushan and A.V. Goldade. Kelvin probe microscopy measurements of surface potential change under wear at low loads. *Wear*, 244(1):104–117, 2000.
- [72] H. Liu and B. Bhushan. Nanotribological characterization of molecularly thick lubricant films for applications to MEMS/NEMS by AFM. *Ultramicroscopy*, 97(1):321–340, 2003.
- [73] J.G. Guo, L.J. Zhou, and Y.P. Zhao. Instability analysis of torsional MEMS/NEMS actuators under capillary force. *J. Colloid Interface Sci.*, 331(2):458–462, 2009.
- [74] Y. Liu and S.K. Sinha. Wear performances of uhmwpe composites with nacre and cnts, and pfpe coatings for bio-medical applications. *Wear*, 300:44–54, 2013.
- [75] M. Chandross, G.S. Grest, and M.J. Stevens. Friction between alkylsilane monolayers: Molecular simulation of ordered monolayers. *Langmuir*, 18(22):8392–8399, 2002.
- [76] P.T. Mikulski, L.A. Herman, and J.A. Harrison. Odd and even model self-assembled monolayers: Links between friction and structure. *Langmuir*, 21(26):12197–12206, 2005.
- [77] L. Ramin and A. Jabbarzadeh. Effect of load on structural and frictional properties of alkanethiol self-assembled monolayers on gold: Some oddeven effects. *Langmuir*, 28(9):4102–4112, 2012.
- [78] R.J. Waltman, G.W. Tyndall, and J. Pacansky. Computer-modeling study of the interactions of zdol with amorphous carbon surfaces. *Langmuir*, 15(19):6470–6483, 1999.

- [79] A. Koike. Molecular dynamics study of tribological behavior of confined branched and linear perfluoropolyethers. *J. Phys. Chem. B*, 103(22):4578 – 4589, 1999.
- [80] H.C. Li, C. McCabe, S.T. Cui, P.T. Cummings, and H.D. Cochran. On the development of a general force field for the molecular simulation of perfluoroethers. *Mol. Phys.*, 101(14):2157 – 2169, 2003.
- [81] P.S. Chung, H. Park, and M.S. Jhon. The static and dynamic responses of binary mixture perfluoropolyether lubricant films molecular structural effects. *IEEE Trans. Magn.*, 45(10):3644 – 3647, 2009.
- [82] R.L. Smith, Y.I. Jhon, L.T. Biegler, and M.S. Jhon. An atomistic study of perfluoropolyether lubricant thermal stability in heat assisted magnetic recording. *IEEE Trans. Magn.*, 49(7):3748 – 3751, 2013.
- [83] B. Jiang, D.J. Keffer, and B.J. Edwards. Estimation and analysis of the rheological properties of a perfluoropolyether through molecular dynamics simulation. *J. Fluorine Chem.*, 127(6):787 – 795, 2006.
- [84] S. Ogata, H. Zhang, K. Fukuzawa, and Y. Mitsuya. Quantification of the surface morphology of lubricant films with polar end groups using molecular dynamics simulations: Periodic changes in morphology depending on film thickness. *J. Tribol.*, 130(2):022301, 2008.
- [85] Y. Li, C.H. Wong, B. Li, S. Yu, W. Hua, and W. Zhou. Lubricant evolution and depletion under laser heating: A molecular dynamics study. *Soft Matter*, 8(20):5649–5657, 2012.
- [86] M. Fukuda, H. Zhang, T. Ishiguro, K. Fukuzawa, and S. Itoh. Adhesion properties of nanometer-thick perfluoropolyether films confined between solid surfaces: A coarse-grained molecular dynamics study. *Tribol. Lett.*, 51(3):479 – 487, 2013.
- [87] B. Derjaguin. Range of action of surface forces. *Nature*, 138:330 – 331, 1936.
- [88] Q. Wu and H. Wong. A slope-dependent disjoining pressure for non-zero contact angles. *J. Fluid Mech.*, 506(29):157–185, 2004.
- [89] S. Izumisawa and M.S. Jhon. Calculation of disjoining pressure for lubricant films via molecular simulation. *IEEE Trans. Magn.*, 42(10):2543–2545, 2006.
- [90] A.P. Bowles, Y.T. Hsia, P.M. Jones, L.R. White, and J.W. Schneider. Quasi-equilibrium AFM measurement of disjoining pressure in lubricant nanofilms II: Effect of substrate materials. *Langmuir*, 25(4):2101–2106, 2009.

- [91] T. Yi and H. Wong. Theory of slope-dependent disjoining pressure with application to Lennard-Jones liquid films. *J. Colloid Interface Sci.*, 313(13):579–591, 2007.
- [92] Y.T. Hsia, P. Jones, and L.R. White. Can contact-angle measurements determine the disjoining pressure in liquid nanofilms on rigid substrates? *Langmuir*, 20(23):10073–10079, 2004.
- [93] H.J. Butt, K. Graf, and M. Kappl. *Physics and Chemistry of Interfaces*. Wiley-VCH, 2006.
- [94] J.N. Israelachvili. *Intermolecular and Surface Forces, Revised Third Edition*. Academic press, 2011.
- [95] T.P. Straatsma and J.A. McCammon. Computational alchemy. *Annu. Rev. Phys. Chem.*, 43(1):407–435, 1992.
- [96] W.P. Reinhardt, M.A. Miller, and L.M. Amon. Why is it so difficult to simulate entropies, free energies, and their differences. *Acc. Chem. Res.*, 34(7):607–614, 2001.
- [97] D.A. McQuarrie. *Statistical Mechanics*. University Science Books, 2000.
- [98] K. Kremer and G.S. Grest. Dynamics of entangled linear polymer melts: A molecular-dynamics simulation. *J. Chem. Phys.*, 92(8):5057–5086, 1990.
- [99] Q. Guo, S. Izumisawa, D.M. Philips, and M.S. Jhon. Surface morphology and molecular conformation for ultrathin lubricant films with functional end groups. *J. Appl. Phys.*, 93(10):8707–8709, 2003.
- [100] S. Plimpton. Fast parallel algorithms for short-range molecular dynamics. *J. Comp. Phys.*, 117(1):1–19, 1995.
- [101] W. Humphrey, A. Dalke, and K. Schulten. VMD - visual molecular dynamics. *J. Mol. Graphics*, 14(1):33–38, 1996.
- [102] C.M. Mate, M.F. Toney, and K.A. Leach. Roughness of thin perfluoropolyether lubricant films: Influence on disk drive technology. *IEEE Trans. Magn.*, 37(4):1821–1823, 2001.
- [103] A. Oron, S.H. Davis, and S.G. Bankoff. Long-scale evolution of thin liquid films. *Rev. Mod. Phys.*, 69(3):931–980, 1997.
- [104] M.K. Beyer and H. Clausen-Schaumann. Mechanochemistry: The mechanical activation of covalent bonds. *Chem. Rev.*, 105(8):2921–2948, 2005.

- [105] G.A. Bowmaker. Solvent-assisted mechanochemistry. *Chem. Commun*, 49(4):334–348, 2013.
- [106] Z. Huang and R. Boulatov. Chemomechanics: Chemical kinetics for multiscale phenomena. *Chem. Soc. Rev.*, 40(5):2359–2384, 2011.
- [107] R. Boulatov. Mechanochemistry: Demonstrated leverage. *Nat. Chem.*, 5(2):84–86, 2013.
- [108] S.L. James, C.J. Adams, C. Bolm, D. Braga, P. Collier, T. Frišćić, F. Grepioni, K.M.D. Harris, G. Hyett, W. Jones, A. Kerbs, J. Mack, L. Maini, A.G. Orpen, I.P. Parkin, W.C. Shearouse, J.W. Steed, and D.C. Waddell. Mechanochemistry: Opportunities for new and clearer synthesis. *Chem. Soc. Rev.*, 41(1):413–447, 2012.
- [109] M. D. Eddleston, M. Arhangelskis, T. Frišćić, and W. Jones. Solid state grinding as a tool to aid enantiomeric resolution by cocrystallisation. *Chem. Commun.*, 48(92):11340–11342, 2012.
- [110] M. Rief, F. Oesterhelt, B. Heymann, and H.E. Gaub. Single molecule force spectroscopy on polysaccharides by atomic force microscopy. *Science*, 275(5304):1295–1297, 1997.
- [111] J. Zlatanova, S.M. Lindsey, and S.H. Leuba. Single molecule force spectroscopy in biology using the atomic force microscopy. *Prog. Biophys. Mol. Bio.*, 74(1):37–61, 2000.
- [112] G. Hummer and A. Szabo. Free energy surfaces from single-molecule force spectroscopy. *Accounts Chem. Res.*, 38(7):504–513, 2005.
- [113] P. Seema, J. Behler, and D. Marx. Force-induced mechanical response of molecule-metal interfaces: Molecular nanomechanics of propanethiolate self-assembled monolayers on au(111). *Phys. Chem. Chem. Phys.*, 15(38):16001–16011, 2013.
- [114] M. Konôpka, R. Turanský, M. Dubecký, D. Marx, and I. Štich. Molecular mechanochemistry understood at the nanoscale: Thiolate interfaces and junctions with copper surfaces and clusters. *J. Phys. Chem. C*, 113(20):8878–8887, 2009.
- [115] X.D. Xiao, G. Liu, D.H. Charych, and M. Salmeron. Preparation, structure, and mechanical stability of alkylsilane monolayers on mica. *Langmuir*, 11(5):1600–1604, 1995.

- [116] A. Lio, C. Morant, D.F. Ogletree, and M. Salmeron. Atomic force microscopy study of the pressure-dependent structural and friction properties of n-alkanethiols on gold. *J. Phys. Chem. B*, 101(24):4767–4773, 1997.
- [117] J.A. Boscoboinik, R.R. Kohlmeier, J. Chen, and W.T. Tysoe. Efficient transport of gold atoms with a scanning tunneling microscopy tip and linker molecule. *Langmuir*, 27(15):9337–9344, 2011.
- [118] R. Fraenkel, G.E. Butterworth, and C.D. Bain. In situ vibrational spectroscopy of an organic monolayer at the sapphire-quartz interface. *J. Am. Chem. Soc.*, 120(1):203–204, 1998.
- [119] T. Friščić, I. Halasz, P.J. Beldon, A.M. Belenguer, F. Adams, S.A.J. Kimber, V. Honkimáki, and R.E. Dinnebier. Real-time and in situ monitoring of mechanochemical milling reactions. *Nat. Chem.*, 5(1):66–73, 2013.
- [120] M. Kalin and J. Vižintin. Comparison of different theoretical models for flash temperature calculations under fretting conditions. *Tribol. Int.*, 34(12):831–839, 2001.
- [121] O.A. Mazzyar, H. Xie, and W.L. Hase. Nonequilibrium energy dissipation at the interface of sliding model hydroxylated alpha-alumina surfaces. *J. Chem. Phys.*, 122(9):094713, 2005.
- [122] S. Nošé. A unified formulation of the constant temperature molecular-dynamics method. *J. Comp. Phys.*, 81(1):511–519, 1984.
- [123] O.J. Furlong, B.P. Miller, Z. Li, J. Walker, L. Burkholder, and W.T. Tysoe. The surface chemistry of dimethyl disulfide on copper. *Langmuir*, 26(12):16375–16380, 2010.
- [124] P.A. Redhead. Thermal desorption of gasses. *Vacuum*, 12(4):203–211, 1962.
- [125] J.A. Harrison, J.D. Schall, M.T. Knippenberg, G. Guangtu, and T.M. Paul. Elucidating atomic-scale friction using molecular dynamics and specialized analysis technique. *J. Phys. Condens. Matter*, 20(35):354009, 2008.
- [126] K.L. Johnson. *Contact Mechanics*. Cambridge University Press, Cambridge, U.K., 1985.
- [127] J.A. Greenwood and J.B.P. Williamson. Contact of nominally flat surfaces. *Proc. R. Soc. London Ser. A*, 295(1442):300–319, 1966.
- [128] F. Gao, O. Furlong, P.V. Kotvis, and W.T. Tysoe. Pressure dependence of shear strengths of thin films on metal surfaces measured in ultrahigh vacuum. *Tribol. Lett.*, 31(2):99–106, 2008.

- [129] Y. Liao, E. Hoffman, M. Wimmer, A. Fischer, J. Jacobs, and L. Marks. Cocromo metal-on-metal hip replacements. *Phys. Chem. Chem. Phys.*, 15(3):746–756, 2013.
- [130] Y. Liao, R. Pourzal, M.A. Wimmer, J.J. Jacobs, A. Fischer, and L.D. Marks. Graphitic tribological layers in metal-on-metal hip replacements. *Science*, 334(6063):1687–1690, 2011.
- [131] B.J. Hamrock, S.R. Schmid, and B.O. Jacobson. *Fundamentals of Fluid Film Lubrication*. McGraw-Hill, New York, 1994.
- [132] Y. Liu, Q.J. Wang, W. Wang, Y. Hu, D. Zhu, I. Krupka, and M. Hartl. EHL simulations using free-volume viscosity model. *Tribol. Lett.*, 23(1):27–37, 2006.
- [133] S.H. Lee and P.T. Cummings. Shear viscosity of model mixtures by nonequilibrium molecular dynamics. *J. Chem. Phys.*, 99(5):3919–3925, 1993.
- [134] A.E. Likhtman, S.K. Sukumaran, and J. Ramirez. Linear viscoelasticity from molecular dynamics simulation of entangled polymer. *Macromolecules*, 40(18):6748–6757, 2007.
- [135] W.G. Hoover and W.T. Ashurst. Nonequilibrium molecular dynamics. *Theor. Chem.: Adv. Perspect*, 1:1–51, 1975.
- [136] M. Mondello and G.S. Grest. Viscosity calculations of n-alkanes by equilibrium molecular dynamics. *J. Chem. Phys.*, 106(22):9327–9336, 1997.
- [137] B.Y.C. So and E.E. Klaus. Viscosity-pressure correlation of liquids. *ASLE Transactions*, 23(4):409–421, 1980.
- [138] W.G. Johnston. A method to calculate pressure-viscosity coefficients from bulk properties of lubricants. *ASLE Transactions*, 24(2):232–238, 1981.
- [139] C.S. Wu, E.E. Klaus, and J.L. Duda. Development of a method for the prediction of pressure-viscosity coefficients of lubricating oils based on free-volume theory. *ASME J. Tribol.*, 111(1):121–128, 1989.
- [140] S. Bair and F. Qureshi. Accurate measurements of the pressure-viscosity behavior in lubricants. *Tribol. Trans.*, 45(3):390–396, 2002.
- [141] S. Bair and A. Laesecke. Normalized ashurts-hoover scaling and a comprehensive viscosity correlation for compressed liquids. *J. Tribol.*, 134(2):021801, 2012.
- [142] A. Martini and A. Vadakepatt. Compressibility of thin film lubricants characterized using atomistic simulation. *Tribol. Lett.*, 38(1):33–38, 2010.

- [143] A. Vadakepatt and A. Martini. Confined fluid compressibility predicted using molecular dynamics simulation. *Tribol. Int.*, 44(3):330–335, 2011.
- [144] X. Ye, S. Cui, V.F. de Almeida, and B. Khomami. Effect of varying the 1-4 intramolecular scaling factor in atomistic simulations of long-chain n-alkanes with the opl-s-aa model. *J. Mol. Model*, 19(3):1251–1258, 2013.
- [145] M.L. Connolly. Computation of molecular volume. *J. Am. Chem. Soc.*, 107(5):1118–1124, 1985.
- [146] R.N. Haward. Occupied volume of liquids and polymers. *J. Macromol. Sci., Part C: Polymer Reviews*, 4(2):191–242, 1970.
- [147] Y.H. Zhao, M.H. Abraham, and A.M. Zissimos. Fast calculation of van der waals volume as a sum of atomic and bond contributions and its application to drug compounds. *J. Org. Chem.*, 68(19):7368–7373, 2003.
- [148] G. Cai, L. Zhang, L. Ma, and W. Eli. Synthesis and characterization of polybutylacrylate viscosity index improver with anti-wear function. *Lubr. Sci.*, 27(4):209–216, 2015.
- [149] N.S. Ahmed and A.M. Nassar. *Lubricating Oil Additives*. InTech, Open Access Publisher, 2011.
- [150] A. Jukic, E. Vidovic, and Z. Janovic. Alkyl methacrylate and styrene terpolymers as lubricating oil viscosity index improvers. *Chem. Tech. Fuels Oils*, 43(5):386–394, 2007.
- [151] S.A. Mohamad, N.S. Ahmed, S.M. Hassanein, and A.M. Rashad. Investigation of polyacrylates copolymers as lube oil viscosity index improvers. *J. Petrol. Sci. Eng.*, 100:173–177, 2012.
- [152] I.Š. Jerbić, J.P. Vuković, and A. Jukić. Production and application properties of dispersive viscosity index improvers. *Ind. Eng. Chem. Res.*, 51(37):11914–11923, 2012.
- [153] T. Stöhr, B. Eisenberg, and M. Müller. A new generation of high performance viscosity modifiers based on comb polymers. *SAE Int. J. Fuels Lubr.*, 1(2008-01-2462):1511–1516, 2008.
- [154] J. Wang, Z. Ye, and S. Zhu. Topology-engineered hyperbranched high-molecular-weight polyethylenes as lubricant viscosity-index improvers of high shear stability. *Ind. Eng. Chem. Res.*, 46(4):1174–1178, 2007.

- [155] S. Morgan, Z. Ye, R. Subramanian, and S. Zhu. Higher-molecular-weight hyperbranched polyethylenes containing crosslinking structures as lubricant viscosity-index improvers. *Polym. Eng. Sci.*, 50(5):911–918, 2010.
- [156] P. Ghosh and M. Das. Synthesis, characterization, and performance evaluation of some multifunctional lube oil additives. *J. Chem. Eng. Data*, 58(3):510–516, 2013.
- [157] A.M. Nassar. Synthesis and evaluation of viscosity index improvers and pour point depressant for lube oil. *Pet. Sci. Technol.*, 26(5):523–531, 2008.
- [158] P. Ghosh and M. Das. Study of the influence of some polymeric additives as viscosity index improvers and pour point depressants synthesis and characterization. *J. Petrol. Sci. Eng.*, 119:79–84, 2014.
- [159] H.G. Müller. Mechanism of action of viscosity index improvers. *Tribol. Int.*, 11(3):189–192, 1978.
- [160] M.J. Covitch and K.J. Trickett. How polymers behave as viscosity index improvers in lubricating oils. *Adv. Chem. Engineer. Sci.*, 5(02):134–151, 2015.
- [161] D. LaRiviere, A.F.A. Asfour, A. Hage, and J.Z. Gao. Viscometric properties of viscosity index improvers in lubricant base oil over a wide temperature range. part i: Group ii base oil. *Lubr. Sci.*, 12(02):133–143, 2000.
- [162] J. Dale. The conformational consequences of replacing methylene groups by ether oxygen. *Tetrahedron*, 30(12):1683–1694, 1974.
- [163] W.L. Van Horne. Polymethacrylates as viscosity index improvers and pour point depressants. *Ind. Eng. Chem*, 41(5):952–959, 1949.
- [164] M.R. Sutton, W.R.S. Barton, and D. Price. Lubricating composition comprising poly (isobutylene)/poly (vinyl aromatic) block copolymer, 2012. Int. Pat. CA 2,012,162,207.
- [165] J.R. Johnson and B.J. Schober. Loose core star polymers and lubricating composition thereof, 2014. Int. Pat. CA 2,014,031,154.
- [166] A. Duggal. Lubricant additives, 2012. U.S. Pat. CA 2,012,010,1017 A1.
- [167] H.A. Bruson. Composition of matter and processes, 1937. U.S. Pat. CA 2,019,627 A.
- [168] P.J. Flory. *Principles of Polymer Chemistry*. Cornell University Press, Ithaca New York, 1952.

- [169] C.C. Han. Molecular weight and temperature dependence of intrinsic viscosity of polymer solutions. *Polymer*, 20(9):1083–1086, 1979.
- [170] H.R. Colby. Scaling analysis of the temperature dependence of intrinsic viscosity. *J. Polym. Sci.; Part B: Polym. Phys.*, 35(12):1989–1991, 1997.
- [171] V.J. Novotny. Temperature dependence of hydrodynamic dimensions of polystyrenes in cyclohexane by quasielastic light scattering. *J. Chem. Phys.*, 78(1):183–189, 1983.
- [172] J. Mazur and D. McIntyre. The determination of chain statistical parameters by light scattering measurements. *Macromolecules*, 8(4):464–476, 1975.
- [173] Y.B. Melnichenko, E. Kiran, K. Heath, S. Salaniwal, H.D. Cochran, M. Stamm, W.A.V. Hook, and G.D. Wignall. *Scattering From Polymers*, volume 739. ACS Symposium Series, Washington, 1999.
- [174] Y.B. Melnichenko and G.D. Wignall. Comparison of inter- and intramolecular correlations of polystyrene in poor and theta solvents via small-angle neutron scattering. *Macromolecules*, 31(23):8346–8438, 1998.
- [175] Z.M. Dong and Z.B. Ye. Hyperbranched polyethylenes by chain walking polymerization: Synthesis, properties, functionalization, and applications. *Polym. Chem.*, 3(2):286–301, 2012.
- [176] J.W. Robinson, Y. Zhou, J. Qu, R. Erck, and L. Cosimbescu. Effects of star-shaped poly(alkyl methacrylate) arm uniformity on lubricant properties. *J. Appl. Polym. Sci.*, 133(26):43611–43621, 2016.
- [177] P. Bhattacharya, U.S. Ramasamy, S. Krueger, J.W. Robinson, B.J. Tarasevich, A. Martini, and L. Cosimbescu. Trends in thermoresponsive behavior of lipophilic polymers. *Ind. Eng. Chem. Res.*, 55(51):12983–12990, 2016.
- [178] U.S. Ramasamy, S. Lichter, and A. Martini. Effect of molecular-scale features on the polymer coil size of model viscosity index improvers. *Tribol. Lett.*, 62(23):1–7, 2016.
- [179] B. Aichmayer, H.C. Margolis, R. Sigel, Y. Yamakoshi, J.P. Simmer, and P. Fratzl. The onset of amelogenin nanosphere aggregation studied by small-angle x-ray scattering and dynamic light scattering. *J. Struct. Biol.*, 151(3):239–249, 2005.

- [180] F. Han, A.H. Soeriyadi, S.R.C. Vivekchand, and J.J. Gooding. Simple method for tuning the optical properties of thermoresponsive plasmonic nanogels. *ACS Macro Lett.*, 5(5):626–630, 2016.
- [181] H. Cheng, S. Xie, Y. Zhou, W. Huang, D. Yan, J. Yang, and B. Ji. Effect of degree of branching on the thermoresponsive phase transition behaviors of hyperbranched multiarmed copolymers: Comparison of systems with LCST transition based on coil-to-globule transition or hydrophilic-hydrophobic balance. *J. Phys. Chem. B*, 114(19):6291–6299, 2010.
- [182] W. Tian, X.Y. Wei, Y.Y. Liu, and X.D. Fan. A branching point thermo and pH dual-responsive hyperbranched polymer based on poly(N-vinylcaprolactam) and poly(N,N-diethyl aminoethyl methacrylate). *Polym. Chem.*, 4(9):2850–2863, 2013.
- [183] K. Chenoweth, A.C.T. van Duin, and W.A. Goddard. Reaxff reactive force field for molecular dynamics simulations of hydrocarbon oxidation. *J. Phys. Chem. A*, 112(5):1040–1053, 2008.
- [184] B.A. Miller-Chou and J.L. Koenig. A review of polymer dissolution. *Prog. Polym. Sci.*, 28(8):1223–1270, 2003.
- [185] P.E. Rouse Jr. A theory of the linear viscoelastic properties of dilute solutions of coiling polymers. *J. Chem. Phys.*, 21(7):1272–1280, 1953.
- [186] B.H. Zimm. Dynamics of polymer molecules in dilute solution: Viscoelasticity, flow birefringence and dielectric loss. *J. Chem. Phys.*, 24(2):269–278, 1956.
- [187] P.G. de Gennes. Reptation of a polymer chain in the presence of fixed obstacles. *J. Chem. Phys.*, 55(2):572–579, 1971.